Concepts for Leptoquark Search
at Hera

Peter Schleper

PHYSIKALISCHE INSTITUTE

RWTH AACHEN

Sommerfeldstr.

51 AACHEN, FR GERMANY

Concepts for Leptoquark Search
at Hera

Von der Mathematisch– Naturwissenschaftlichen Fakultät
der Rheinisch– Westfälischen Technischen Hochschule Aachen
genehmigte Dissertation zur Erlangung des akademischen Grades
eines Doktors der Naturwissenschaften

von

Diplom– Physiker

Peter Schleper

aus Oberhausen

für Sylvia

Contents

1 Introduction

In the last decades particle accelerators have played a key role for our present under-standing of the nature of matter. Fixed target experiments together with e^+e^- and $p\bar{p}$ colliders have led to the 'standard model' of high energy physics, which successfully describes all experimental results down to distances of 10^{-16} cm.

In 1992, the new accelerator *HERA* will become operational at DESY, the 'Deutsche Elektronen Synchrotron' in Hamburg. Beeing the first electron proton collider, *HERA* is complementary to other accelerators. The lay out chosen for the beams is asymmetric, 30 GeV for the electrons and 820 GeV for the protons. The resulting center of mass energy of 314 GeV is a real novelty for a lepton quark system and will allow to study the structure of the proton at momentum transfers two orders of magnitude higher than present experiments.

Furthermore, this offers the exciting opportunity to test a new sector of particle physics, namely vertices with a lepton, a quark and a new type of particle, called leptoquark. Such interactions do not exist in the standard model, but can easily be added in a gauge invariant way. Moreover, leptoquarks appear naturally in most theories beyond the standard model as a consequence of symmetries between quarks and leptons. The experimental constraints on this new coupling are rather weak and do not exclude an observation at *HERA*. In contrast, a copious production is possible for leptoquark masses up to 300 GeV.

Experimentally, the high luminosity at *HERA* will cause more than 10^7 events per year. This is a challenge for the hardware and software of the two experiments, *H1* and ZEUS.

This thesis project is devoted to concepts which enable a search for leptoquarks. In view of the large background for these particles, two main aspects are considered:

- The detailed simulation of so many events is very time consuming. Therefore, a new and very fast monte carlo program for the *H1* detector was developed.

- The analysis of presumably rare processes requires a very efficient rejection of background events. For this, a constrained kinematic fit is suggested, which leads to an optimum reconstruction of the leptoquark mass and allows additional cross checks on event interpretations. The results presented here have been published in ref. [1].

2 Predictions for Leptoquarks and Leptogluons

2.1 The Standard Model

The standard model of elementary particle physics [2] is based on the gauge group $SU(3)_c \times SU(2)_L \times U(1)_Y$. The strong interaction is mediated by gluons, which couple to the colours c of quarks. The weak interaction involves only the left handed isospin doublets L of fermions, and the hypercharge Y is related to the electric charge Q of a particle via $Q = T_3 + Y/2$. T_3 is the third component of the weak isospin. Together with the Higgs mechanism of spontaneous symmetry breaking, this model has shown a remarkable success in describing all present experimental data. Many of its predictions, like the weak gauge bosons Z^o, $W^\pm$, have been discovered later on, while others are still to be confirmed or at least not yet excluded (top quark, higgs).

Nevertheless, the standard model is not looked upon as the ultimate theory due to several shortcomings and unexplained features. Among others are:

- The number of free parameters in the model is very large (18 if all neutrinos are assumed to be massless).

- The electromagnetic, weak and strong interactions are not unified, i.e., there are still three independent gauge couplings.

- Gravitation is not included in the model. The Planck scale and the Fermi scale are extremely different ($\approx 10^{19}$ GeV compared to ≈ 100 GeV) .

- The Higgs particle as a fundamental scalar imposes difficulties with diverging mass terms, which require an enormous fine tuning if the Higgs mass should not become extremely large (hierarchy problem).

- There are three known generations of leptons and quarks. The reason for this multiplication of fermions with very different masses for each generation, and generally the distinction of the generations, is not understood.

- No explanation is given for the symmetry between the lepton and the quark sector with respect to their electroweak interactions.

The last item is closely related to the problem of anomalies in triangle diagrams. For the chiral couplings of the weak interaction, such diagrams lead to non-- renormalizable divergencies for each fermion. However, these anomalies cancel if the sum of electric charges Q of all fermions in one generation equals zero. Assuming three colours, this interrelates the charges of the quarks (u, d) to those of the leptons (ν, e) in the form

$$Q_e + Q_\nu + 3\left(Q_u + Q_d\right) = 0.$$

This equation, given here for the first generation, is exactly fulfilled for each of the three generations of the standard model, at least if the top quark exists with its anticipated quantum numbers.

Many models have been developed as extensions or alternatives to the standard model. In order to explain experimental data, they are constructed such that they include the standard model as their 'low energy' limit. The lepton– quark relationship is explained by introducing some new symmetry principle and interaction. Most often, this leads to the possibility of a direct Yukawa interaction term in the lagrangian $\mathcal{L}$ between a lepton ℓ, a quark q and a new particle, called leptoquark LQ. Schematically, this can be written

$$\mathcal{L} = \lambda \, \bar{q} \, \ell \; LQ$$

Here as well as in most of the following equations, spinor, weak isospin, colour and flavour indices are suppressed. λ is a dimensionless coupling constant[1]. Such couplings do not exist in the standard model and their experimental effects can be used to search for new physics. Leptoquarks may be scalar or vector particles. They carry lepton and baryon quantum numbers (if these are still conserved in the new theory) and transform as a colour triplet under $SU(3)_c$.

Specifically in composite models, a natural extension of this is to allow also for leptogluons, particles that carry lepton number and belong to a colour octet.

In the following chapters some models with leptoquarks or leptogluons will be introduced together with present experimental constraints on their existence.

2.2 Grand Unifying Theories

In Grand Unifying Theories (GUT), the electroweak and strong interactions are incorporated in a common framework by introducing a new, larger gauge group which can be spontaneously broken down to the standard model group. Typical examples for this are the groups SU(5), SO(10) or SU(15). Leptons and quarks may then be closely related by putting them into the same representations. Besides of often introducing new fermions like right handed neutrinos, a large variety of new gauge bosons appear. Some of them mediate transitions between the leptons and quarks. These bosons are leptoquarks since they carry lepton and baryon quantum numbers. Two main experimental facts put constraints on the parameters of these models.

- Since the aim is to unify electromagnetic, weak and strong interactions, the running coupling constants $\alpha_i(Q^2)$, $(i = 1, 2, 3;$ Q^2 is the square of the 4 momentum transfer) of these 3 theories have to appoach a common value at high Q^2, called the unification scale Λ. This scale typically corresponds to the masses M_X of the additional gauge bosons. Together with the measured, 'low energy' starting points, the slope of the functions $\alpha_i^{-1}(Q^2)$ enter the calculation of Λ. These slopes depend on the particle content of the underlying theory and, if existing, on intermediate symmetry breaking scales.

---

[1]In the literature, λ is sometimes given in relation to the electromagnetic coupling by introducing $F = \frac{\lambda^2}{4\pi} \frac{1}{\alpha_{elm}}$, where $\alpha_{elm} = \frac{1}{137}$ is the electromagnetic fine structure constant. So $\lambda \approx 0.3$ means that $F \approx 1$ and that the Yukawa coupling is of electromagnetic strength. The units used throughout this text are defined by setting $\hbar = c = 1$. Masses, energies and momenta are thus given in GeV.

- The lifetime of nucleons is very high. The Frèjus, IMB and Kamiokande nucleon decay experiments [3] have set a lower limit on the proton lifetime τ_p of

$$\tau_p \times BR_{(p \to e^+ \pi^0)} > 5 \times 10^{32} \text{ years} \qquad (1)$$

at 90% confidence level[2]. The proton lifetime is related to the mass M_X of the gauge boson and to the proton mass m_p like

$$\tau_p \approx \frac{C}{\alpha^{-2}} \frac{M_X^4}{m_p^5}.$$

Assuming that the coupling constant α of the unified theory, evaluated at $Q^2 = M_X^2$, is $\approx 1/40$ and $C \approx 1$ for the hadronic matrix element, the limit given above corresponds to $M_X > 10^{16}$ GeV. This example shows that all leptoquarks with baryon number violating gauge couplings to up and down quarks should be very heavy and out of reach for any collider experiment.

For the simplest GUT, the minimal SU(5), none of these two constraints are fulfilled. Especially the latest measurements of the strong coupling constant and of electroweak parameters at LEP have excluded, at the level of 7 standard deviations, that all three running coupling constants coincide in one point [4].

Recently however, an extension of the minimal $SU(5)$ theory [5] has caused interest. In this model, a new pair of light leptoquarks with masses of ≈ 100 GeV are introduced. These leptoquarks are allowed to couple to fermions only as

$$\mathcal{L} = \lambda \, \bar{d}_R \ell_L \, LQ.$$

Here the indices L, R denote left and right handed states of fermions. ℓ_L is the left handed $SU(2)_L$ doublet of leptons and d_R is the right handed, $SU(2)_L$ singlet d- quark. Since there are no couplings to quark pairs, these light leptoquarks do not induce fast proton decays. It has also been shown that with this new particle content, the slope of the running coupling constants changes enough to allow them to obtain the same value at a common scale[3]. The prediction for the strong coupling constant α_s agrees well with measurements and also the proton lifetime obtained $\tau_p \times BR_{(p \to e^+ \pi^0)} = 7 \times 10^{29}$ – 7×10^{32} years is marginally compatible with experimental data. No argument is given to explain the large unnatural mass difference between these light leptoquarks (called *SU(5)- saver*) and the other, very heavy leptoquarks of this model. In any case, this is clearly a model to be supported or rejected by the *HERA* experiments.

Based on the gauge group SU(15), a model with explicit baryon and lepton number conservation has been suggested [6]. The fermions are arranged in different multiplets such that flavour changing neutral currents are suppressed. In this model several new intermediate symmetry breaking scales are introduced. Accessible to experiments is the lightest scale, between 250 GeV and 2 TeV, where diquarks, dileptons and all types of scalar and vector leptoquarks are predicted.

---

[2]In the minimal $SU(5)$ model, the branching ratio $BR_{(p \to e^+ \pi^0)}$ is predicted to be close to one.

[3]It is noted however that the values taken for the coupling constants are not exactly the ones from ref. [4].

2.3 Supersymmetry

In the minimal supersymmetric model (MSSM) [7], an additional new boson (fermion) is introduced for each fermion (boson) of the standard model. These supersymmetric partners carry precisely the same quantum numbers of $SU(3)_c \times SU(2)_L \times U(1)_Y$. In the simpliest form the superpotential conserves baryon number B and lepton number L and a new quantum number, called R- parity, which is defined as

$$R = (-1)^{3B+L+2S}$$

where S is the spin. Therefore, supersymmetric particles can only be produced in pairs, which implies that the lightest of them must be stable and escapes detection. This model does not contain leptoquarks.

Without disturbing gauge invariance, it is however possible to add R– parity violating terms to the lagrangian, which then, necessarily, does not conserve either baryon number or lepton number. In this case the lightest supersymmetric particle is not stable but might decay inside a detector. Limits for the MSSM which depend on the signature of missing transverse momentum (CDF limits) are therefore not applicable for these specific models. The lepton number violating part of the lagrangian contains Yukawa couplings of quarks and leptons to their supersymmetric partners, the squarks $(\tilde{u}, \tilde{d})$ and sleptons $(\tilde{e}, \tilde{\nu})$.

$$\mathcal{L} = \lambda^{ijk} \left[-\tilde{u}_L^j \bar{d}_R^k e_L^i - (\tilde{d}_R^k)^*(\bar{e}_L^i)^c u_L^j + \tilde{d}_L^j \bar{d}_R^k \nu_L^i + (\tilde{d}_R^k)^*(\bar{\nu}_L^i)^c d_L^j - \tilde{e}_L^i \bar{d}_R^k u_L^j + \tilde{\nu}_L^i \bar{d}_R^k d_L^j \right]$$

The notation is adopted from ref [8]. c stands for charge conjugation and $i, j, k = 1, 2, 3$ are generation indices. Formally, the first four expressions resemble the leptoquark interactions with fermions, with squarks taking the part of the leptoquarks. In ep-collisions, squarks are produced via the first two terms in the lagrangian given above and only quarks of the first generation have to be considered. For squarks decaying via Yukawa couplings the signature will be identical to the one of leptoquarks, at least if only one of the λ^{ijk} does not vanish [8]. Thus the analysis of leptoquark signatures can be reinterpreted directly to determine these R- violating couplings.

On the other hand, squarks may also decay via their gauge couplings, preferentially into a quark and a gluino or photino (the gluino $\tilde{g}$ is the fermionic superpartner of the gluon, the photino the one of the photon). These branches are characterized by at least three jets and a lepton, which originates from secondary decays of the lightest super-symmetric particle. The leptoquark– like decay dominates only if one of the following items is fulfilled:

- the strength of the Yukawa coupling is comparable to the gauge couplings
- the squark is lighter than the gluino or photino
- the squark is lighter than the corresponding quark.

Concerning the first possibility their exist a variety of low energy experiments [9] setting stringent limits for the lepton number violating couplings λ^{ijk}. From the requirement of charged current universality in μ and β decays and the determination of Kobayashi-Maskawa matrix elements one finds $\|\lambda^{11k}\| < 3 \times 10^{-4}\,m_{\tilde{q}}$ GeV^{-1}, where $m_{\tilde{q}}$ is the mass of the squark. Measurements of parity violating couplings in atoms yield $\|\lambda^{1j1}\| < 2.6 \times 10^{-3}\,m_{\tilde{q}}$ GeV^{-1}. The second number is comparable to the electromagnetic coupling ($\lambda^2/4\pi \approx \alpha_{elm}$) for masses around 100 GeV. This indicates that squarks of heavy generations might be accessible. It is also not excluded by collider experiments that the top quark is heavier than the stop thereby suppressing decays $\tilde{t} \rightarrow t\tilde{g}$. Thus a leptoquark search at *HERA* will automatically examine the possibility of a 'light' squark (stop) with $R-$ parity violating couplings to fermions of the first generation. The present experimental bound on this coupling is $\lambda < 0.26$ [10].

2.4   E$_6$ Superstring Models

Superstring models [11] extend the usual concept of point like particles by introducing strings moving in 10 dimensions as the new fundamental objects. The gauge group E_6 is studied most frequently as the 'low energy' 4 dimensional limit of this theory. Each of the (27) representations of this group contains all known fermions of one generation together with additional, new fermions. Two of them have scalar superpartners $\tilde{D}_o, \tilde{D}_o^c$ with Yukawa couplings to the known quarks and leptons [12][13][14][15]. They are $SU(2)_L$ singlets with electric charges of 1/3 and -1/3 respectively. Their masses are expected to be relatively small, between 50 GeV and 1000 GeV [15]. In order to avoid fast decays of protons and to obey constraints from neutrino masses, the couplings of these two leptoquarks have to be arranged such, that vertices with two quarks and two leptons vanish. The remaining terms are then fixed and give [13]

$$\mathcal{L} = \lambda_L \tilde{D}_o^c\, \bar{q}_L^c\, i\tau_2\, \ell_L + \lambda_R \tilde{D}_o^c\, \bar{u}_R^c\, e_R$$

where τ_2 is a Pauli spin matrix. q_L and ℓ_L are as usual the $SU(2)_L$ doublets of quarks and leptons. The two coupling constants λ_L and λ_R are generally independent. Experimentally they can be distinguished by using polarized electron beams.

In addition, E_6 superstring models include a right handed massive partner ν_L^c of the neutrino, giving the additional term

$$\lambda_\nu \tilde{D}_o\, \bar{d}_R\, \nu_L^c \ ,$$

where λ_ν is independent of λ_L, λ_R. In *ep* scattering, such a heavy neutrino could be produced in the decay of a $\tilde{D}_o$. In a right handed electron beam needed to produce the $\tilde{D}_o$, such a process has no direct background from the standard model, since a neutrino from a charged current event can not occur.

2.5 Compositeness and Technicolour

Another suggestion to overcome the deficiencies of the standard model is to introduce a new, more fundamental layer of matter, out of which the known particle spectrum is composed.

In extended technicolour theories [16] the Higgs particle as the only scalar in the standard model is assumed to consist out of two new technifermions which couple to each other via a new, confining interaction. Together with the known fermions they are placed in one representation of the associated gauge group. Symmetry breaking then induces a spectrum of massive pseudo– Goldstone bosons, some of them carrying lepton and baryon quantum numbers. Their masses are expected to be in the order of 100 GeV. In contrast to other models, the couplings of these technicolour leptoquarks are expected to be proportional to the mass of the participating fermions because the Goldstone boson masses and the fermion masses have a common origin. Their production with light quarks in ep scattering is thus very much suppressed. On the other hand, the production of eb, et type leptoquarks requires the creation of heavy quark flavours by splitting a gluon. The high limits for top quark masses from CDF and the reduced cross section disfavour such an observation at *HERA*. This process has been studied extensively in [17] and will not be considered here.

In compositeness models it is assumed that all known fermions and bosons may be compound states of some more basic particles called preons [18]. In the model of Abbott and Fahri [19], sometimes called the 'Strongly Coupled Standard Model' (SCSM), the lagrangian is the same as in the standard model. However the parameters of the weak sector are chosen such that no spontaneous symmetry breaking occurs, and that the $SU(2)_L$ gauge interaction, refered to as 'hypercolour force', is confining at a scale $G_F^{1/2}$ (G_F is the Fermi constant). Thus all known fermions and bosons have to be $SU(2)_L$ singlets. The observable, left handed fermions are constructed as bound states of a left handed preonic fermion Ψ^a ($a=1...12$ for all flavours of quarks and leptons) and a fundamental scalar. In contrast, the right handed fermions are not composed. The familiar weak interaction is then a residual of the more fundamental gauge theory. It has been shown that parameters can be chosen such that in the low energy limit the compositeness model is indistinguishable from the standard model.

In addition to the known particles, new $SU(2)_L$ singlet, bound states occur naturally in these models. For example, the basic fermions might couple in the form $\Psi^a\Psi^b$ or $\Psi^a\bar{\Psi}^b$. These scalar or vector (or even tensor) particles S^{ab}, V^{ab} couple to the known fermions L_a as [20]

$$\mathcal{L}_S = \lambda_S\, S^{ab}\, \bar{L}_a^c \tau_2 L_b$$

$$\mathcal{L}_V = \lambda_V\, V_\mu^{ab}\, \bar{L}_a^c \gamma^\mu L_b$$

where γ^μ are the Dirac spinor matrices. In case of couplings to quarks and leptons these bosons are leptoquarks and may carry lepton and baryon quantum numbers. The coupling constants $\lambda_{S,V}$ are expected to be in the order of one [20].

2.6   Model Independent Leptoquark Couplings

Instead of separately considering all the different models predicting the existence of leptoquarks, it is more favourable to use a model independent framework for the analysis. As a 'low energy' limit of an underlying theory, Buchmüller, Rückl and Wyler [27] discussed an effective lagrangian which obeys baryon and lepton number conservation and is invariant with respect to the standard model transformations $SU(3)_c \times SU(2)_L \times U(1)_Y$. Their description includes *all possible* dimensionless Yukawa couplings[4] of scalar and vector leptoquarks to the known fermions. In table 1 scalar (vector) particles are denoted by S (V), and the index $0, \frac{1}{2}, 1$ stands for the weak isospin. The upper half

LQ name	electric charge	SU(2) representation	left handed couplings	right handed couplings
S_0	-1/3	singlet	$\lambda_{L S_0}\, \bar{q}_L^c\, i\tau_2\, \ell_L\, S_0$	$\lambda_{R S_0}\, \bar{u}_R^c\, e_R\, S_0$
$\tilde{S}_0$	-4/3	singlet		$\lambda_{R S_0}\, \bar{d}_R^c\, e_R\, S_0$
S_1	2/3, -1/3, -4/3	triplet	$\lambda_{L S_1}\, \bar{q}_L^c\, i\tau_2 \vec{\tau}\, \ell_L\, S_1$	
$V_{1/2}$	2/3, -1/3	doublet	$\lambda_{L V_{1/2}}\, \bar{d}_R^c\, \gamma^\mu\, \ell_L\, V_{1/2\,\mu}$	$\lambda_{R V_{1/2}}\, \bar{q}_L^c\, \gamma^\mu\, e_R\, V_{1/2\,\mu}$
$\tilde{V}_{1/2}$	2/3, -1/3	doublet	$\lambda_{L \tilde{V}_{1/2}}\, \bar{u}_R^c\, \gamma^\mu\, \ell_L\, V_{1/2\,\mu}$	
V_0	-2/3	singlet	$\lambda_{L V_0}\, \bar{q}_L\, \gamma^\mu\, \ell_L\, V_{0\,\mu}$	$\lambda_{R V_0}\, \bar{d}_R\, \gamma^\mu\, e_R\, V_{0\,\mu}$
$\tilde{V}_0$	-5/3	singlet		$\lambda_{R \tilde{V}_0}\, \bar{u}_R\, \gamma^\mu\, e_R\, V_{0\,\mu}$
V_1	1/3, -2/3, -5/3	triplet	$\lambda_{L V_1}\, \bar{q}_L\, \vec{\tau}\gamma^\mu\, \ell_L\, V_{1\,\mu}$	
$S_{1/2}$	-2/3, -5/3	doublet	$\lambda_{L S_{1/2}}\, \bar{u}_R\, \ell_L\, S_{1/2}$	$\lambda_{R S_{1/2}}\, \bar{q}_L\, i\tau_2\, e_R\, S_{1/2}$
$\tilde{S}_{1/2}$	-2/3 ,1/3	doublet	$\lambda_{L \tilde{S}_{1/2}}\, \bar{d}_R\, \ell_L\, S_{1/2}$	

Table 1: *Couplings of scalar (S) and vector (V) leptoquarks to fermions (ℓ_L and q_L denote left handed lepton and quark doublets, τ_i are the Pauli matrices.)*

of the table contains the particles with fermion number two (lepton– quark), the lower half those with fermion number zero (lepton– antiquark). Some of the leptoquarks only have lefthanded (λ_L) or righthanded (λ_R) couplings.

Generally leptoquarks might couple to fermions of any family, and the couplings to different families are independent. In this sense, ℓ, q, u, d, e, ν are doublets and singlets of any generation.

This classification scheme for leptoquarks will be used throughout the following discussions. The analysis of discovery or exclusion limits (chapter 5, 6) is carried out for all these leptoquark types individually.

---

[4]As all these particles carry charge, hypercharge and colour they also have electroweak and strong gauge couplings.

Comparing the quantum numbers and lagrangians of this phenomenological framework with those of the specific models discussed in the previous chapters, the following correspondence is found:

- The $SU(5)$ 'saver' leptoquarks of section 2.2 [5] corresponds to the $\bar{S}_{1/2}$.
- The $SU(15)$ model presented in section 2.2 [6] includes all leptoquark types!
- The R– parity violating version of the minimal supersymmetry (section 2.2 [8]) does not contain leptoquarks, but scalar quarks with couplings similar to those of leptoquarks.
- In superstring inspired E_6 models (chapter 2.4 [12]), the S_o leptoquark appears.
- In compositeness models, many types of scalar and vector leptoquarks are possible.

Generally, the $SU(2)_L$ multiplet leptoquarks of table 1 consist of different states, which might have different masses due to symmetry breaking. The situation is comparable to the mass splitting of the Z° and the $W^\pm$ in the standard electroweak theory. However, in this analysis, such a possible mass difference for leptoquarks will be neglected. So, all states of one multiplet are assumed to be degenerated in mass and experimentally, they can be distinguished only by their electric charge. Since this is very difficult, limits will be given only for the whole multiplet summing over all states.

2.7 Existing Limits for Leptoquarks

Bounds for masses M_{LQ} and Yukawa couplings λ of leptoquarks are obtained from virtual effects and from direct searches in collider experiments. Here only those limits are mentioned which are relevant for masses below the *HERA* c.m.s. energy of 314 GeV. As argued earlier, only baryon and lepton number conserving couplings will be considered. The limits discussed in the following chapters are summarized in figure 1.

Rare Processes

Low energy experiments constrain mainly effects which are either forbidden or which are of higher order in the standard model. All the following limits for leptoquarks are deduced from ref. [29]. Where possible these limits have been updated with more recent experimental results on rare processes reported in [30].

- Generally, leptoquarks are not restricted to couple only to fermions of one generation. Let λ^{ij}, with $i,j = 1,2,3$, where i labels the quark generation and j the lepton generation. Then the existence of λ^{12} together with λ^{11} would induce lepton flavour number violating processes like $\mu + u \rightarrow LQ \rightarrow e + u$. The limit of this reaction in muonic atoms yields

$$M_{LQ} \geq 200 \text{ TeV} \times \sqrt{\lambda^{11}\lambda^{12}}.$$

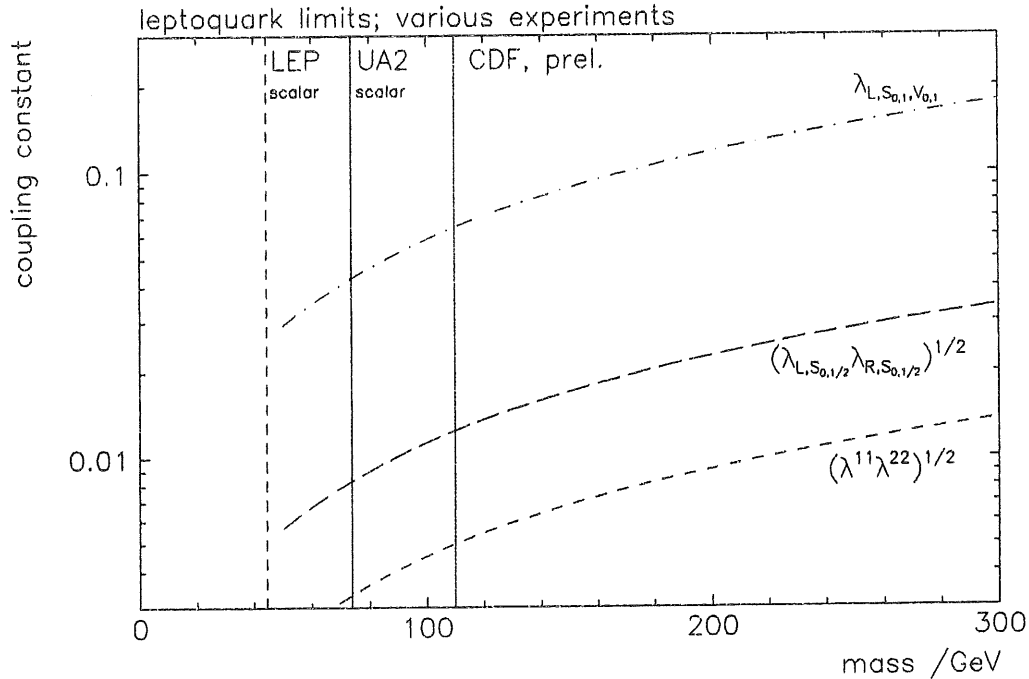Limits for λ^{i3} from conversions of τ leptons ($\tau \rightarrow \mu, e$) are much less stringent [31].

Figure 1: *Present limits for leptoquarks. Excluded are the regions above and right of the curves. See the text for further explanations and references.*

- Also the coexistence of λ^{11} and λ^{22} is severely constrained, since then $\bar{s} \to LQ + \nu_\mu \to \nu_\mu + \bar{\nu}_e + \bar{d}$ would be allowed, then. The limit for the flavour changing neutral current process $K^+ \to \pi^+ \nu \bar{\nu}$ yields

$$M_{LQ} \geq 22 \text{ TeV} \times \sqrt{\lambda^{11}\lambda^{22}}$$

For simplicity in the notation, generation indices will be omitted from now on, and only λ^{11} will be discussed.

- In the standard model, the decay $\pi^+ \to e^+\nu_e$ is helicity suppressed because the weak vector bosons couple only to left handed fermions. For scalar leptoquarks with couplings to left and right handed leptons this suppression does not exist. The small value of the branching ratio $\text{BR}(\pi^+ \to e^+\nu_e)$ can therefore be translated in limits for the S_0 and $S_{1/2}$ leptoquarks.

$$M_{S_0,S_{1/2}} \geq 8.8 \text{ TeV} \times \sqrt{\lambda_L \lambda_R}$$

for couplings to leptons and quarks of the first generation.

- The left handed couplings λ_L of S_0, S_1, V_0 and V_1 to the quark and lepton doublets allow the transitions $d \rightarrow lQ + \bar{\nu}_e \rightarrow u + e + \bar{\nu}_e$. These contribute to the beta decay process and would result in a modification of the Fermi constant G_F. Because the same constant measured in muon decay is not modified (at least not by leptoquark exchange alone), a comparison of both measurements restricts the coupling strength λ_L to

$$M_{S_0,S_1,V_0,V_1} \geq 1.7 \text{ TeV} \times \lambda_L$$

These indirect limits from virtual effects depend critically on the assumption that the occurrence of leptoquarks is the only low energy effect beyond the standard model interactions. If this is not the case the limits might be weekend substantially.

In conclusion, this means that for leptoquarks accessible at *HERA* with masses of a few hundred GeV, all flavour non-diagonal couplings should be very small. Also the existence of flavour diagonal couplings to more than one generation is strongly suppressed. This suggests, that each generation of fermions might have its own leptoquarks. The existence of both left and right handed couplings is also disfavoured but might still allow a small production of leptoquarks at *HERA* (see chapter 6).

If however the leptoquark couplings are chiral, there are (rather weak) constraints only for certain left handed couplings. In this case the couplings might even be of the same strength as gauge couplings, without beeing detected so far.

e^+e^- Colliders

In e^+e^- collisions leptoquarks may be produced either in pairs or single, or they might contribute only virtually.

In the pair production process of leptoquarks shown in figure 2.7, the $s-$ channel cross section only depends on the gauge couplings to bosons. The coupling to the photon is fixed by the leptoquark charge, while the interaction with the Z^o depends on the weak group structure of the specific leptoquark. The $t-$ channel exchange of a u- quark in comparison is sensitive to the Yukawa coupling λ of leptoquarks. However, as long as λ is not much larger than the gauge couplings, this cross section is much smaller [32]. At PETRA [33][34] and LEP [35], leptoquarks have been searched for – with negative results – in decay channels to all three generations. The limits obtained are typically only marginally below the kinematic boundary of half the center of mass energy. For scalar leptoquarks of mass M_S with couplings to electrons and muons, the lower mass limit at 95% confidence level is $M_S > 44.2$ GeV and $M_S > 41.4$ GeV for decays in $\tau-$ leptons. Limits for vector leptoquarks are not yet published but are expected to be of similar size. This also holds for 'The Next Linear e^+e^- Collider' (NLC) with a center of mass energy of 500 GeV [32].

At higher masses, $\sqrt{s} > M_{LQ} > \frac{1}{2}\sqrt{s}$, ($\sqrt{s}$ is the center of mass energy of the accelerator) the production of single leptoquarks becomes relevant. The cross section
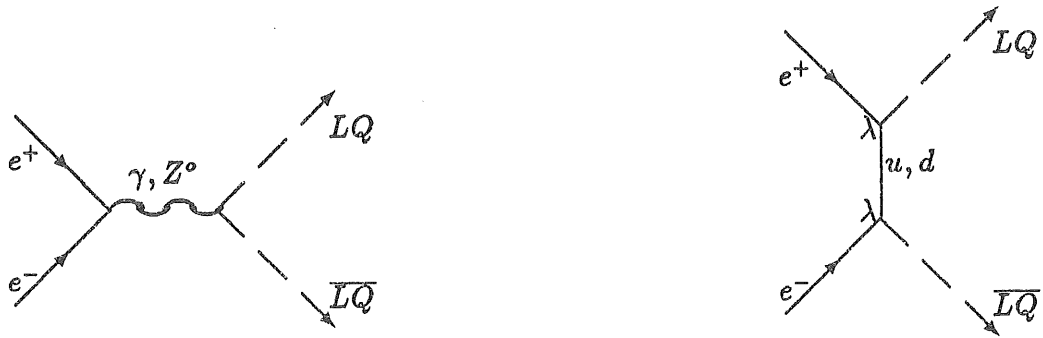
Figure 2: *Pair production of leptoquarks in e^+e^- collisions.*
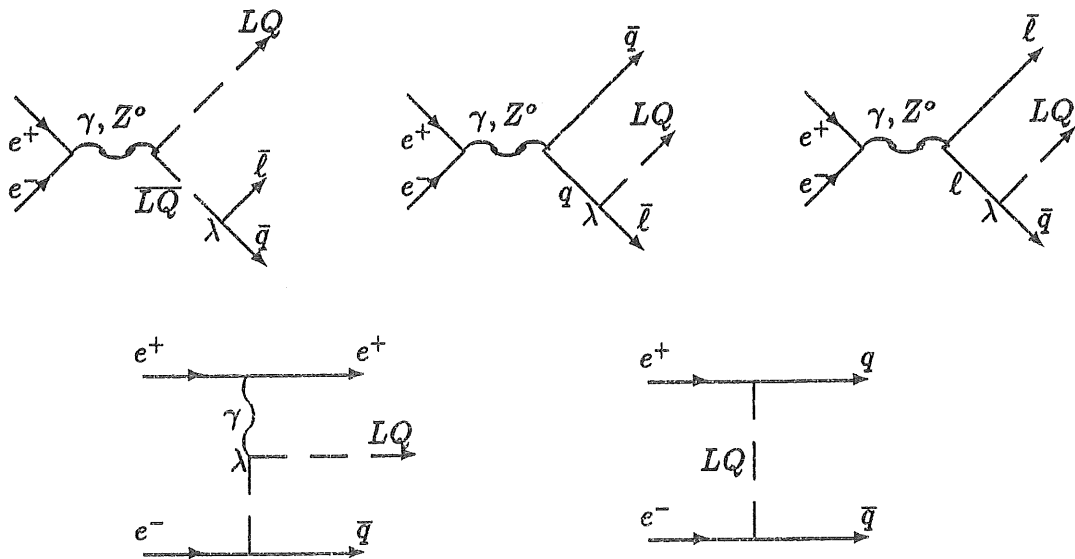*left: s-channel, right: u-channel.*

Figure 3: *Single production of leptoquarks in e^+e^- collisions*

then depends on the Yukawa coupling constant λ, as can be seen in the diagrams of figure 3. At LEP I, the graphs involving the Z^o are dominant, while at higher energies the lower left diagram becomes more important. It has been estimated[5] for LEP I [12] that for Yukawa couplings of electromagnetic strength, a leptoquark signal up to $M_{LQ} \approx 80$ GeV would be observable well above the background from heavy quarks. However, experimental limits from this search are not yet published.

Leptoquarks with even higher masses contribute in the $t-$ channel resulting in a final state of two quarks (lower right diagram in figure 3). Such events cannot be separated from the much higher s-channel pair- production via gauge bosons. As an example for LEP II, a 200 GeV leptoquark with a coupling of electromagnetic strength yields

_____

[5]Compare also [13] for the case of a future $\sqrt{s} = 1$ TeV collider.

just a 2% increase in the cross section. The limits obtainable (unpublished) depend quadratically on the Yukawa coupling.

$p\bar{p}$ Colliders

In $p\bar{p}$– collisions leptoquarks can be produced in pairs in $q\bar{q}$– annihilation or, dominating, in the fusion of two gluons [36][37]. These processes are shown in the first two diagrams of figure 4. In this case the colour properties of the leptoquark determines
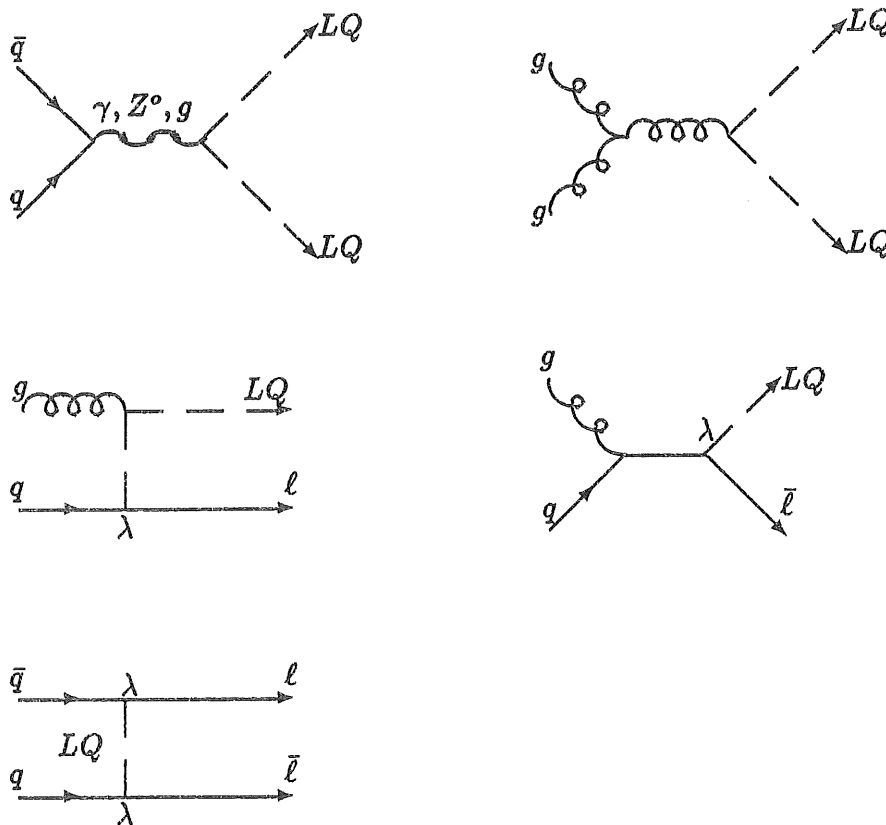

Figure 4: *Production of leptoquarks in $p\bar{p}$ collisions*

the interaction. The cross section does not depend on the electroweak couplings and is thereby independent of the weak group structure of the new theory. At the CERN SPPS collider, the UA2 experiment has searched for scalar leptoquarks decaying into an electron or neutrino[38]. The lower mass limits found are 74 GeV if only decays into electrons are allowed and 67 GeV for branching ratios of 50%. If the neutrino decay mode would be dominating, the limits are decreasing substantially and the LEP results are more restrictive. No limits are given for vector leptoquarks and for decays into leptons of higher generations.

In contrast to the pair production process, the Yukawa couplings of leptoquarks enter in the fusion process of a quark and a gluon, which gives a lepton and a single leptoquark in the final state (figure 4). Due to the steeply falling gluon spectrum the cross section is much smaller and the obtained limits are thus weaker.

For the CDF experiment no results are published[6]. Possible limits have been estimated [41] by extrapolating the data of the SPPS collider at CERN mentioned above. From the predicted cross sections at both accelerators, limits are expected [41] to reach up to $M_{LQ} > 110$ GeV for the presently collected integrated luminosity of 4.4 pb^{-1}. A future run with 25 pb^{-1} might restrict this further to $M_{LQ} > 150$ GeV. However, this extrapolation towards increasing center of mass energy assumes, that the cross section for the background in both experiments scales in the same way as the leptoquark cross section.

Virtual leptoquarks contribute via Yukawa couplings in the $t-$ channel to the process $q\bar{q} \rightarrow l^+l^-$. Compared to the production of real leptoquarks, the increase in sensitivity for higher masses is rather limited [36]. It has been estimated that with a coupling of electromagnetic strength, $\lambda^2/4\pi = \alpha_{elm}$, and a leptoquark mass of 250 (300) GeV, the cross section only changes by 1% for the SPPS (Tevatron).

2.8   Leptogluons

Leptogluons are generally predicted by all those compositeness models which assume that the weak gauge bosons are made of coloured constituents.

As an example, the Fritsch– Mandelbaum model [21] [22] includes two $SU(2)_L$ doublets, (α, β) with spin 1/2, and (x, y) with spin 0. All these states are colour anti-triplets. Then it is possible to construct bosonic states

$$W^+, W^{(3)}, W^- = (\bar{\beta}\alpha, \frac{1}{\sqrt{2}}(\bar{\alpha}\alpha - \bar{\beta}\beta), \bar{\alpha}\beta).$$

The colour singlet states are identified as the weak gauge bosons, and the corresponding colour octet states are new gauge bosons. The fermions may be constructed as

$$\nu_e = \alpha\bar{y} \qquad\qquad u = \alpha x$$
$$e = \beta\bar{y} \qquad\qquad d = \beta x$$

The colour singlet states of ν_e and e are supposed to be the physical neutrino and electron. But also colour octet states with lepton number are predicted, which are called leptogluons. The mass of these 'colour excitations' might well be in the order of 100 GeV [23], in spite of the fact that their known lepton relatives are very light.

---

[6]Preliminary results for scalar leptoquarks have been given in [39][40] yielding $M_{LQ,scalar} > 110$ GeV.

Leptogluons *LG* have dimensionless couplings only to gluons. The lowest dimensional, $SU(3)_c$ invariant couplings to leptons are the dimension 5 terms [23][24]

$$\mathcal{L}_{LG} = \frac{g_s}{4\Lambda} \, G^\alpha_{\mu\nu} \, \bar{\ell}_L \, \sigma^{\mu\nu} \, LG^\alpha$$

and

$$\mathcal{L}_{LG} = \frac{g_s}{4\Lambda} \, G^\alpha_{\mu\nu} \, \bar{e}_R \, \sigma^{\mu\nu} \, LG^\alpha$$

where $g_s^2/4\pi = \alpha_s$ is the strong coupling constant, $G^\alpha_{\mu\nu}$ is the gluon field and the superscript α is a colour index. Λ is the scale where the hypercolour interaction becomes strong[7]. Here it has already been assumed that only either left or right handed couplings to fermions exist. This is strongly suggested by low energy experiments [24].

These couplings are not renormalizable, but have to be seen as an effective, 'low energy' lagrangian of the underlying theory.

In addition to a colour octet charged lepton also the coloured partner of the neutrino should exist. In spite of the expectation that this particle might be much lighter [25], it cannot be produced in the $s-$ channel simply because of charge conservation. However, the existence of coloured leptons implies also coloured weak gauge bosons (see above). Their exchange would allow, also in *ep* collisions, the production of these coloured neutrinos with a signature similar to charge current events of deep inelastic scattering [23]. The cross sections depend strongly on the anticipated mass of these bosons.

e^+e^- Colliders

For leptogluons, no limits have been published yet by the LEP experiments. From a comparison with production and decay mechanisms of leptoquarks, it can however be anticipated that very similar limits ($M_{LG} < 41$ GeV) are valid. The gauge couplings to (at least) photons is the same as for leptoquarks, and the final state in both cases is very much the same. Only the quark jets have to be replaced by gluon jets and the difference in the spin angular distribution has to be considered. The published analysis are not very sensitive to this difference[8].

$p\bar{p}$ Colliders

In proton anti-proton collisions, leptogluons may be produced in pairs similar to the case of leptoquarks. Searches for both charged and neutral leptons from leptogluon decays have been performed at the SPPS collider. The limits are [26]

$$M_{LG,\nu} > 75 \text{ GeV}$$

$$M_{LG,e} > 110 \text{ GeV}.$$

---

[7]See the discussion on this in [23].

[8]See also the example from PETRA in [33],[34].

3 Leptoquark and Leptogluon Signatures at HERA

3.1 HERA

The *HERA* accelerator [43] at *DESY* is the first electron– proton collider. With a center of mass energy of $\sqrt{s} = 314$ GeV, lepton– nucleon scattering will be possible with momentum transfers up to $Q^2 \approx 10^5$ GeV. These are 2 – 3 orders of magnitude more than reached by fixed target experiments.

The ring tunnel with a circumference of 6336m lying underneath the city of Hamburg contains both the electron and the proton accelerator (figure 5). After reaching an energy of 14 GeV in *PETRA*, the electrons are accelerated to 30 GeV. The proton ring is equiped with superconducting magnets. After the injection with only 40 GeV the protons will finally obtain a momentum of 820 GeV. This asymmetric design is a consequence of the huge synchrotron energy losses of the electron beam at high energies. The filling time for both particles types is expected to be less than 20 minutes.

The design luminosity of *HERA* is $L = 1 - 2 \times 10^{31}$ cm$^{-2}s^{-1}$ corresponding to more than $\int L\,dt = 100\,pb^{-1}$ in one year. To reach this value, 210 bunches of each beam have to be stored, which yields a time difference between two bunchcrossings of only 96 ns. The bunch length of the proton beam will be around 44cm compared to 2.5cm for the electrons. So, the vertex position in the beam direction (z) will only be known to ±25cm and has to be determined for each event individually. The horizontal and vertical beam spot (x, y) however will be stable for a given beam orbit and can therefore be averaged over a whole run. The expected precisions are $\delta x = 0.3$ mm and $\delta y = 0.017$ mm respectively.

First *ep* collisions in *HERA*, however with a tiny luminosity, have already been achieved in autumn 1991 with beam energies of 30 and 480 GeV. The lifetime of both beams has been measured to be several hours, which is sufficiently high compared to the filling time. Also some polarization of the electron beam has been observed which would be an essential tool for measuring the helicity structure of known and possible exotic interactions. Positron runs in *HERA* are in principle also possible.

All figures and results given in this text have been calculated for an unpolarized electron beam of 30 GeV momentum and a proton beam of 820 GeV momentum.

Two experiments, *H1* and *ZEUS*, have been constructed and brought into beam position in spring 1992. The first luminosity runs with detectors are envisaged for summer 1992.
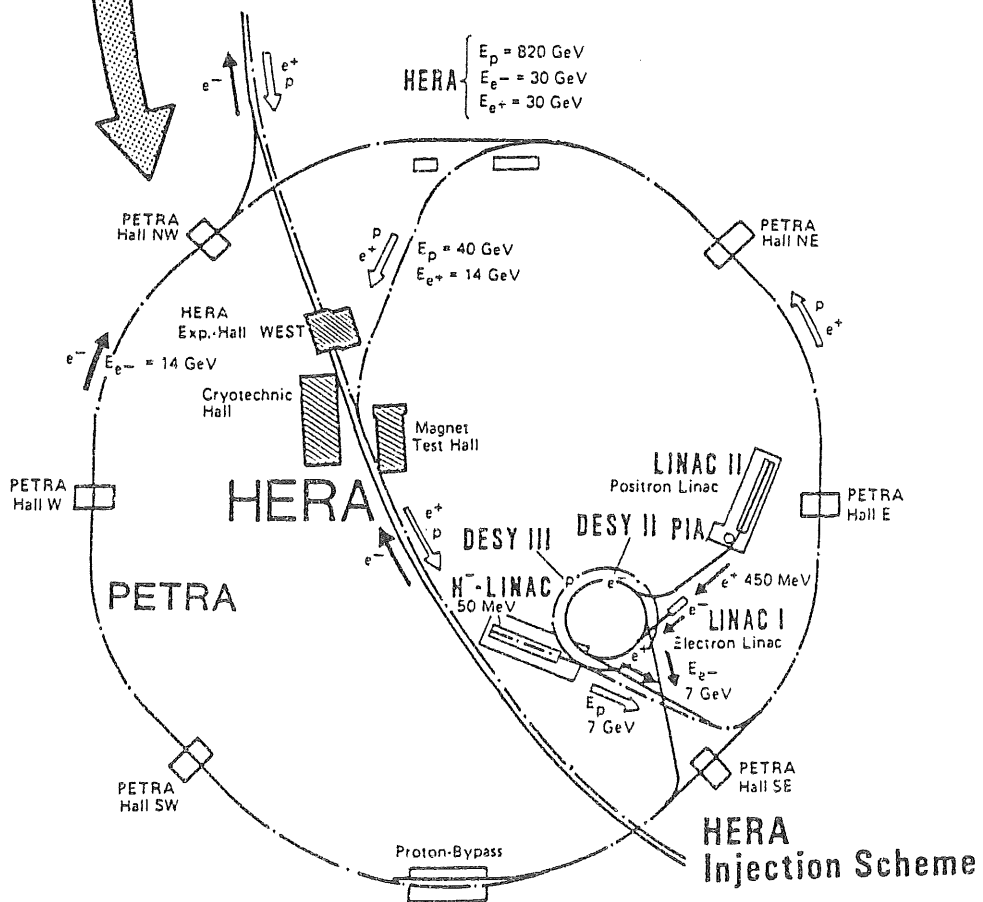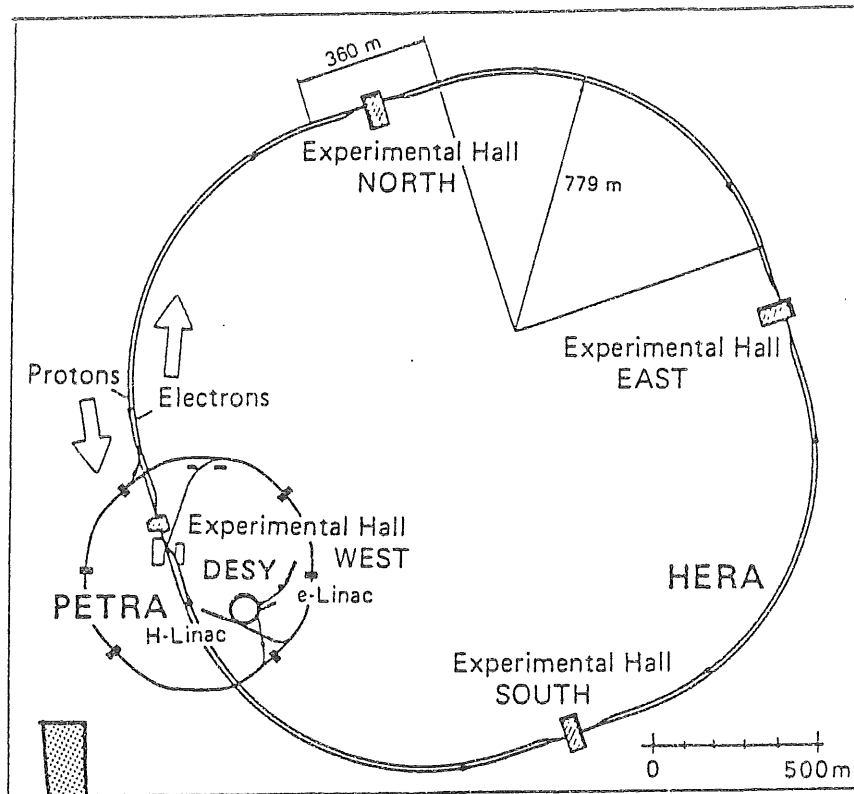
360 m

Experimental Hall
NORTH

779 m

Protons

Electrons

Experimental Hall
EAST

Experimental Hall
WEST

DESY

PETRA

e-Linac

H-Linac

HERA

Experimental Hall
SOUTH

0   500 m

$E_p = 820$ GeV
HERA $\{$ $E_{e^-} = 30$ GeV
$E_{e^+} = 30$ GeV

e^- e^+ / p

PETRA
Hall NW

p
e^+ $E_p = 40$ GeV
$E_{e^+} = 14$ GeV

PETRA
Hall NE

HERA
Exp.-Hall WEST

e^- $E_{e^-} = 14$ GeV

p
e^+

Cryotechnic
Hall

Magnet
Test Hall

LINAC II
Positron Linac

PETRA
Hall W

PETRA
Hall E

HERA

e^+
p

DESY III

DESY II PIA

e^+

PETRA

e^-

H$^-$-LINAC
50 MeV

p
e^-

e^+ 450 MeV

e^- LINAC I
Electron Linac

e^+

E_{e^-}
7 GeV

E_p
7 GeV

PETRA
Hall SE

PETRA
Hall SW

HERA
Injection Scheme

Proton-Bypass

Figure 5: *The electron proton collider HERA at DESY*

3.2   Deep Inelastic Scattering

One of the main reasons for building *HERA* is the possibility to study the structure functions of the proton in deep inelastic scattering events (DIS). For the first time neutral and charged current events measured in one experiment can be used for their evaluation.

The Born diagram for deep inelastic scattering is shown in figure 6 with the exchange of a photon, a Z^o or a $W^\pm$.
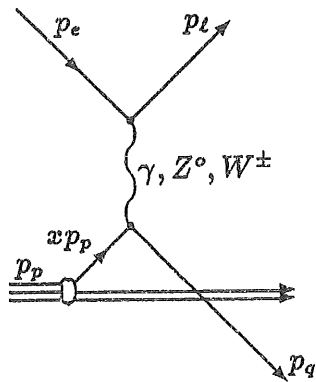

Figure 6: *Feynman diagram for deep inelastic scattering in electron proton collisions.*

The 4 momentum transfer q at the hard scattering vertex is

$$q = p_e - p_\ell = p_q - x p_p = p_h - p_p \tag{2}$$

where p_q is the four vector of the scattered quark and p_h is the four vector sum of all hadrons in the final state of the event. The Bjorken scaling variables x, y and Q^2 are defined as

$$Q^2 \equiv -q^2 \tag{3}$$

$$y \equiv \frac{p_p \cdot q}{p_p \cdot p_e} \tag{4}$$

$$x \equiv \frac{Q^2}{2 \, p_p \cdot q} = \frac{Q^2}{y \, s} \tag{5}$$

with $\sqrt{s}$ beeing the center of mass energy at *HERA*:

$$s = (p_e + p_p)^2 \approx 4 \, E_e \, E_p \tag{6}$$

Here as well as in all following equations, the masses of leptons, quarks and the proton will be neglected. In addition it will frequently be assumed that the incoming quark does not have transverse momentum.

The Mandelstamm variables are calculated as

$$\hat{s} = xs \tag{7}$$

$$\hat{t} = -Q^2 \tag{8}$$

$$\hat{u} = Q^2 - xs \tag{9}$$

In the parton model, x is interpreted as the momentum fraction of a parton in the proton.

3.3 Leptoquark Production

HERA opens the unique possibility to observe leptoquarks and leptogluons in direct collisions of electrons and partons. In contrast to e^+e^- or $p\bar{p}$ accelerators, the dominant cross section for these particles is not given by pair production via gauge couplings, but they can be created as single particles due to Yukawa couplings. Together with the high center of mass energy this means that a mass range will be accessible which has not been directly observable up to now.

Since the proton mainly consists of light quarks it is natural to consider for the production of leptoquarks at *HERA* only couplings to fermions of the first generation.

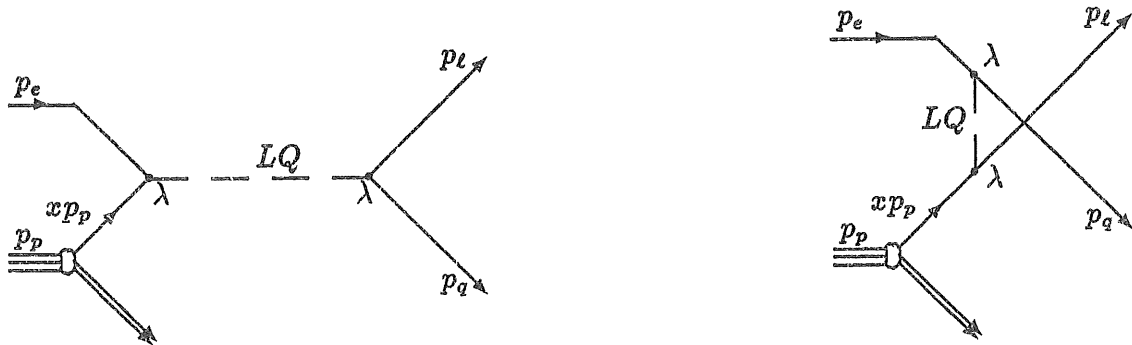The two lowest order diagrams are shown in figure 7. The corresponding production

Figure 7: *Feynman diagram for the s– channel (left) and u– channel (right) production of leptoquarks in ep collisions.*

cross sections for all leptoquark species have been calculated in [27].

In the *s*– channel the beam electron is fusing directly with a quark of the proton. The cross section σ for a scalar leptoquark can be written

$$\frac{d\sigma}{dx\,dQ^2} = \frac{1}{32\pi} \sum_q q(x, Q^2) \frac{\lambda_{L,R}^4}{(xs - M_{LQ}^2)^2 + M_{LQ}^2 \Gamma_{LQ}^2} \tag{10}$$

and for a vector leptoquark

$$\frac{d\sigma}{dx\, dQ^2} = \frac{1}{8\pi} \sum_q q(x, Q^2) \frac{\lambda_{L,R}^4}{(xs - M_{LQ}^2)^2 + M_{LQ}^2 \Gamma_{LQ}^2} \frac{u^2}{x^2 s^2}. \tag{11}$$

$q(x, Q^2)$ is the probability density function (PDF) for finding a quark q with momentum fraction x in the proton, evaluated at a 4 momentum transfer Q^2. The leptoquark is created on the mass shell and decays with unit probability. For the small couplings detectable at *HERA* (see later), the decay width

$$\Gamma_{LQ} = \lambda^2 M_{LQ} \times \frac{1}{16\pi(24\pi)} \tag{12}$$

(16π for scalar and 24π for vector leptoquarks) is typically between 0.01 MeV and 100 MeV. This means that leptoquarks will show up as an extremely narrow Breit–Wigner resonance in the invariant mass distribution of the decay products (see however the discussion in chapter 5.3.4). In the parton model, the incoming quark carries the momentum xp_p where p_p is the proton beam momentum and x is the Bjorken scaling variable. Therefore the mass of the leptoquark would become visible as a pole in the Bjorken– x distribution (see also chapter 5.3) at

$$M_{LQ}^2 = (p_e + xp_p)^2 \approx xs \tag{13}$$

where s is the center of mass energy and p_e denotes the momentum of the beam electron. Further on, x_o defined as

$$x_o \equiv \frac{M_{LQ}^2}{s} \tag{14}$$

will be used as a measure of the leptoquark mass. It corresponds to the peak position in the Bjorken x distribution for the s– channel Born diagram of leptoquark production.

The u– channel diagram in comparison does not have such a significance and moreover has a much smaller amplitude on the parton level. In addition, for leptoquarks with fermion number $F = 2$, the u– channel only contributes with anti– quarks from the sea, while mainly valence quarks are involved in the fusion process. Thus, at high masses and therefore high x_o, the u– channel is even more suppressed by the ratio of sea quarks over valence quarks.

However this situation is inverted for leptoquarks with $F = 0$. The low probability of finding a high energetic anti– quark in the proton reduces the s–channel cross section. At masses above 250 GeV this contribution is negligible and the coupling constants needed for a measurable cross section in the u– channel are already excluded by experimental data. These relations are of course exchanged in case of a positron beam.

As a rule of thumb, the integrated s– channel cross section for a specific final state can be parameterized as

$$\sigma_{ep \to LQ + X \to l + q + X} \approx \frac{\pi}{4s} \lambda^2 \sum_q q(x_o, Q^2) \times BR_{(LQ \to l + q)} \times 1(2) \tag{15}$$

with a factor 1(2) for scalar(vector) leptoquarks. λ is meant to be either λ_L or λ_R. The sum runs over all quark flavours contributing to the multiplet states of the leptoquark species. So the mass dependence of the cross section is determined only by the shape of the quark density $q(x_o, Q^2)$ in the proton at x_o. The cross section formula (15) applies only for a small natural width of the particle, and if the quark density does not vary significantly within this width.

Due to the limits for family violating transitions and baryon and lepton number conservation, only decays into eq or νq are considered. For the leptoquarks of table 1 the branching ratios BR are fixed. Separately for the left and right handed couplings, table 2 gives an overview of the contributing quark flavours and helicities for the cross sections. The column 'production' describes, in symbolic notation, the cross section for

type	left handed			right handed		
	production	decay		production	decay	
		eq	νq		eq	νq
S_0	$e_L u_L$	1/2	1/2	$e_R u_R$	1	0
$\tilde{S}_0$				$e_R d_R$	1	0
S_1	$e_L u_L + 2 e_L d_L$	$\frac{1/2u_L+2d_L}{u_L+2d_L}$	$\frac{1/2u_L}{u_L+2d_L}$			
$V_{1/2}$	$e_L d_R$	1	0	$e_R d_L + e_R u_L$	1	0
$\tilde{V}_{1/2}$	$e_L u_L$	1	0			
V_0	$e_L \bar{d}_R$	1/2	1/2	$e_R \bar{d}_L$	1	0
$\tilde{V}_0$				$e_R \bar{u}_L$	1	0
V_1	$2 e_L \bar{u}_R + e_L \bar{d}_R$	$\frac{1/2d_R+2\bar{u}_R}{\bar{d}_R+2\bar{u}_R}$	$\frac{1/2d_R}{\bar{d}_R+2\bar{u}_R}$			
$S_{1/2}$	$e_L \bar{u}_L$	1	0	$e_R \bar{u}_R + e_R \bar{d}_R$	1	0
$\tilde{S}_{1/2}$	$e_L \bar{d}_L$	1	0			

Table 2: *Lepton and quark flavours and helicities for s- channel production of leptoquarks. See text for explanations.*

leptoquark production in ep scattering. $e_{L,R}$ is meant to be the probability that a beam electron is left or right handed polarized, and $u_{L,R}(d_{L,R})$ is the probability to find a left or right handed u (d) quark in the proton with a momentum fraction $x_o = M_{LQ}/s$. The product of both, given in column 'production' of table 2, is proportional to the $s-$ channel cross section for leptoquark production with an electron beam of arbitrary polarization. This may be seen from equation 15. It is implicitly understood that the different states of the leptoquark multiplets are degenerated in mass.

For a specific final state, the column 'decay' in table 2 describes the relative probability of finding a decay with an electron or with a neutrino in an event of a given leptoquark type. Again it is summed over all states in the multiplets. This probability

depends on the production channel for the different states in the multiplets, and therefore on the structure functions of u and d quarks and on the mass of the leptoquark. An experimental measurement of this value allows, to some degree, a distinction of the different leptoquark types (see chapter 6.5). Both columns together explain the relations between the different cross sections shown in figure 8.

The full cross sections are given in figure 8 for an arbitraryly chosen, small coupling constant of $\lambda_{L,R} = 0.01$. An unpolarized electron beam is assumed and for each leptoquark only either the lefthanded or the righthanded coupling is taken to be different from zero. As expected the vector leptoquarks V have a higher cross section than the scalar ones S. Also the suppression of the $F = 0$ particles due to their couplings to anti– quarks is obvious. All other details can be deduced from table 2 and equation 15 and the x– dependent shape of the quark densities (The d– quark spectrum is harder than that of the u– quark).

It is evident that for most of the leptoquark species a sizeable event rate can be expected at *HERA* for masses close to the kinematic limit of $\sqrt{s} = 314$ GeV. To give an example, after one year of measurement with the nominal luminosity of $\int L\,dt = 100\,pb^{-1}$, a 200 GeV scalar leptoquark with a coupling constant below the excluded values ($\lambda_{L\,S_0} = 0.1$) would produce in the order of 1300 events.

The spin of the leptoquark determines the y dependence of the cross sections. In their rest frame, scalar particles decay isotropically. Since the lepton scattering angle with respect to the proton direction, ϑ_ℓ^*, is related to the four momentum transfer Q^2 like $1 + \cos\vartheta_\ell^*$, and $Q^2 = x_o y s$, the cross section is flat in y. Vector particles with either lefthanded *or* righthanded couplings decay with an angular distribution $\sim (1 - \cos\vartheta_\ell^*)^2$. This yields a y– dependence $\sim (1 - y)^2$.

The final state of leptoquark events consists of the spectator jet from the proton remnant, together with a lepton and a jet from the decay of the resonance, which are balancing each other in transverse momentum P_T. Therefore

  • the signatures of leptoquark decays are identical to the neutral and charged current modes in deep inelastic scattering (DIS).

This means that both processes will interfere and that DIS events are the most dangerous background for leptoquark searches. Both event classes can only be separated by statistical and not by topological arguments. Furthermore, the kinematic methods applied to DIS analysis can be used directly to determine x_o as a measure of the leptoquark mass. In fact, most of the kinematic considerations given later (chapter 5) can be applied to DIS events and to leptoquarks.

Higher order diagrams for leptoquark production in ep scattering have been studied in ref. [15]. The diagrams considered are shown in figure 9. In the first 4 diagrams the final state of the hard scattering consists of an on– shell leptoquark accompanied by either a gluon or a quark. Also for these diagrams the cross section scales with λ^2.
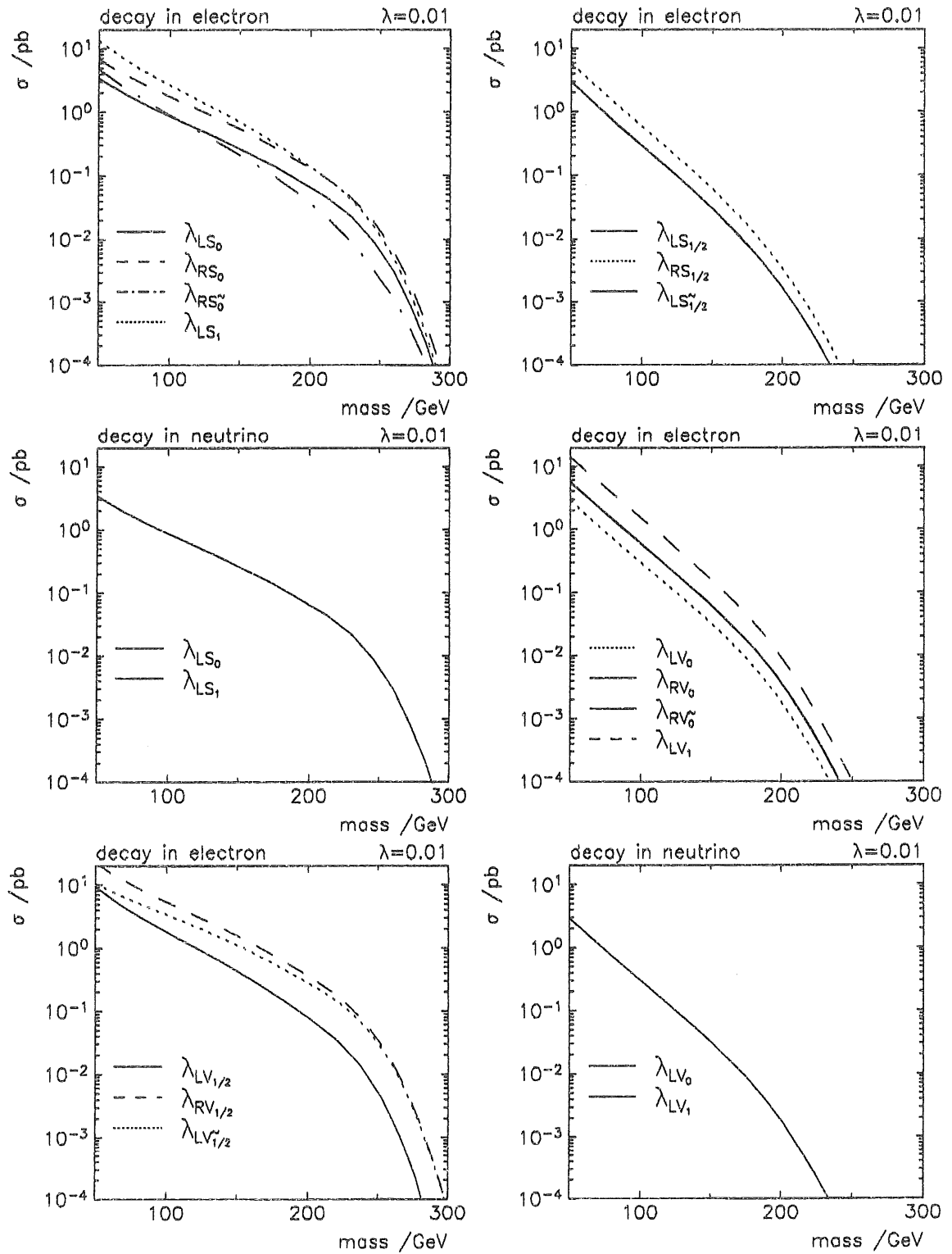
Figure 8: *Cross sections for leptoquarks at HERA for an unpolarized electron beam with* @lambda = 0.01. *The structure functions used are from ref.* [28].
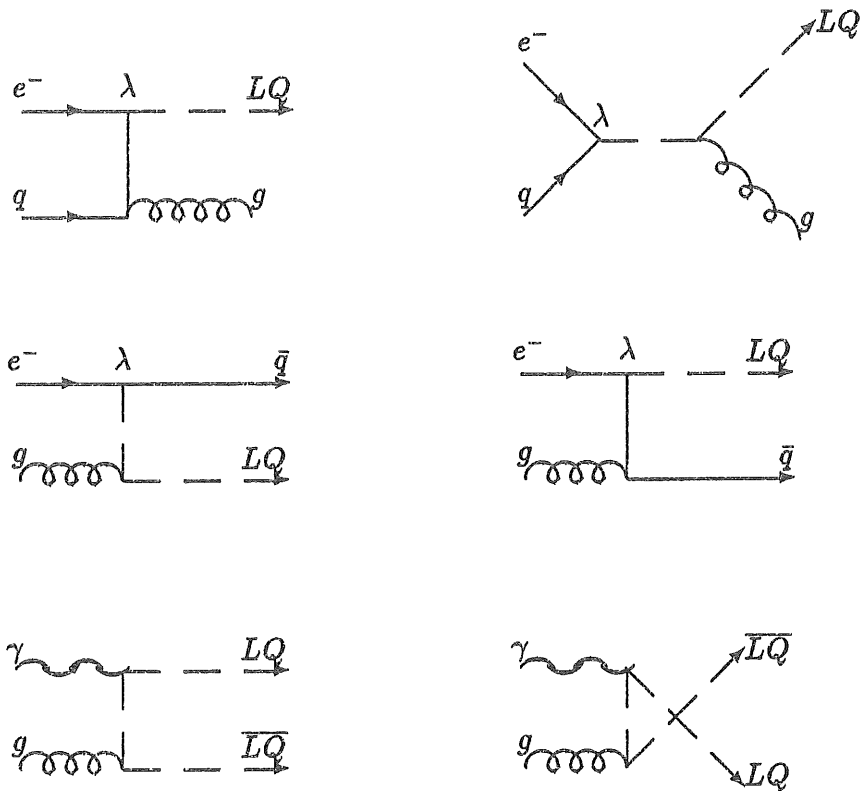
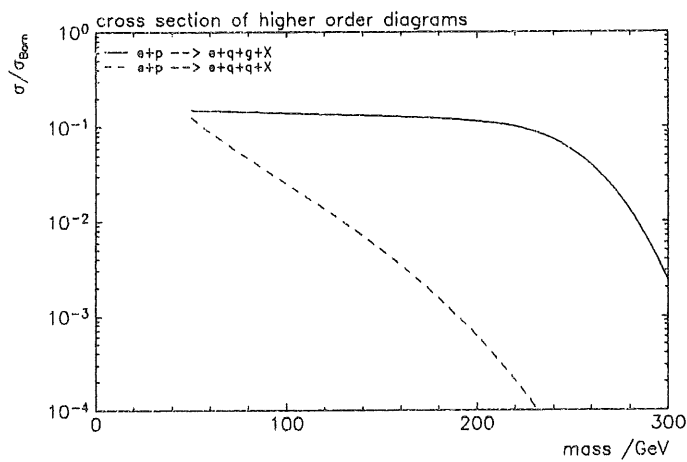Figure 9: *Higher order diagrams for leptoquark production in ep scattering*

Figure 10: *Ratio of the cross section of higher order diagrams to the cross section of the Born diagrams.*

Infered from ref. [15], the ratio of the cross sections for these higher order diagrams with respect to the ones given in figure 7 for the s– channel production are shown in figure 10 for the S_o leptoquark. For this figure a minimum transverse momentum of 5 GeV for the final leptoquark (and the gluon or quark) was required. At masses up to $\approx$200 GeV the higher order diagrams contribute quite substantially (10–20%) while their cross section vanishes at higher masses. Requiring more than 5 GeV transverse momentum would reduce this additional cross section further.

The leptoquark pair production shown in the last 2 diagrams of figure 9 is independent of the Yukawa coupling λ. The cross section however is extremely small, $\sigma \approx 4 \times 10^{-2}$pb at $M = 50$ GeV and $\sigma \approx 10^{-4}$pb at $M = 100$ GeV. In spite of the very nice signature, it will not be possible at *HERA* to observe this reaction, especially if one takes into account the limits reported from UA2 and CDF.

3.4 Leptogluon Production

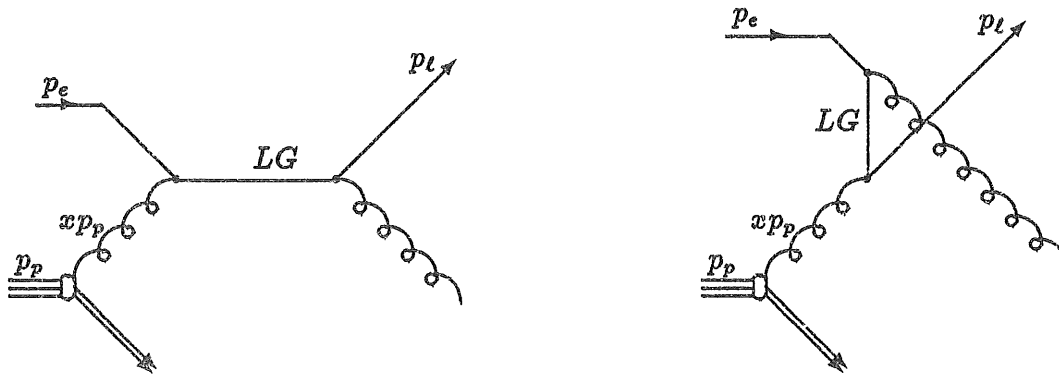The diagrams for leptogluon production are shown in figure 11. The similarity to the

Figure 11: *Feynman diagram for the s– and u– channel production of leptogluons in ep collisions.*

leptoquark diagrams is obvious, just the incoming quark has to be replaced by a gluon. Thus the signatures discussed in chapter 3.3 also hold for leptogluons. However charge conservation does not allow decays in neutrinos and there are, at least for the Born terms, no interferences with the deep inelastic scattering diagrams.

The decay width of leptogluons depends strongly on the ratio M_{LG}/Λ, where Λ sets the scale of the underlying interaction [24][42].

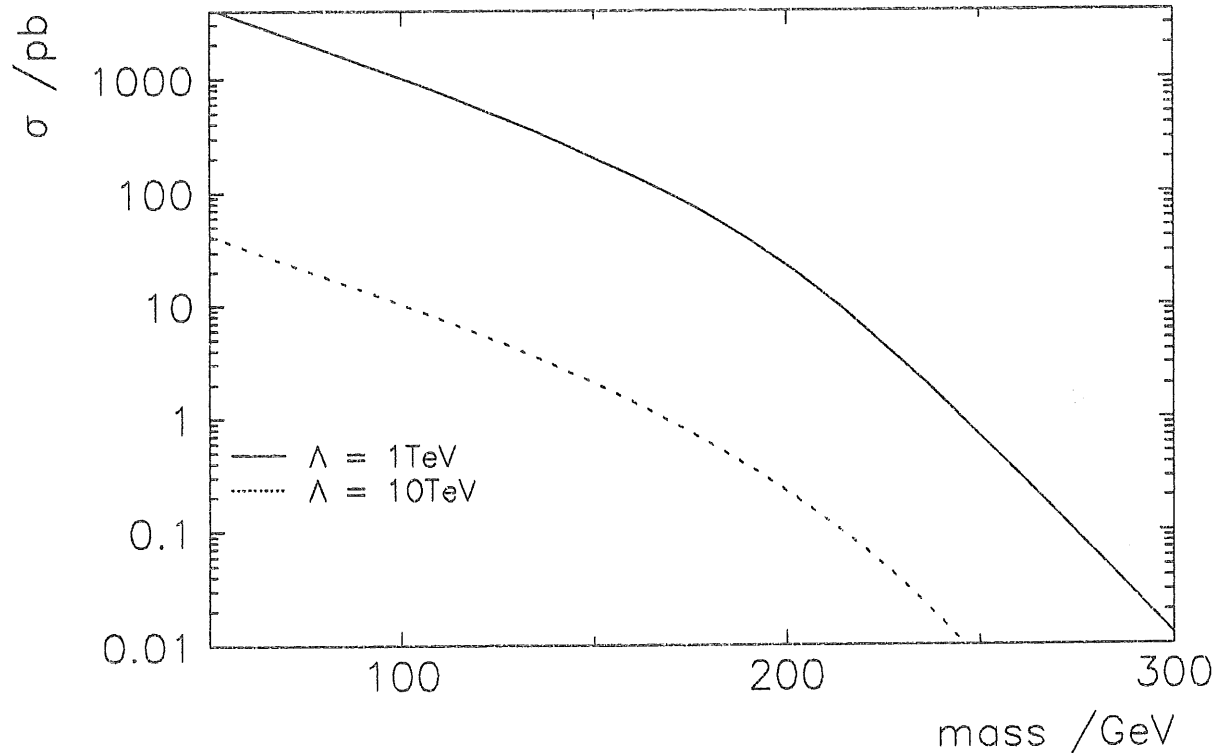$$\Gamma_{LG} = \frac{\alpha_s}{4} \frac{M_{LG}^3}{\Lambda^2} \tag{16}$$

Figure 12: *Cross section for leptogluons at HERA. The gluon structure function used is from [28].*

For the high scales observable at *HERA* ($\Lambda > 1$ TeV) this width is always below 1 GeV. In this case the total cross section is [23][24][42]

$$\sigma_{ep \to LG} \approx \frac{2\pi^2 \, \alpha_s}{s} \left(\frac{M_{LG}}{\Lambda}\right)^2 g(x_o, Q^2) \tag{17}$$

with $g(x_o, Q^2)$ being the gluon density in the proton.

The total cross section for $\Lambda = 1$ TeV and $\Lambda = 10$ TeV is shown in figure 12. The mass (x) dependence reflects the steeply falling gluon density in the proton. For small scales an extremely large event rate would be observable. In the simplest case leptogluons have spin 1/2. Therefore the shape of the cross section is proportional to $(1 - y)$.

3.5 Event Generation

The event generator used for this analysis is COMPOS 1.3 [42] which includes all the leptoquark and leptogluon processes. In addition, COMPOS treats initial state bremsstrahlung from the electron using the Weizsäcker– Williams approximation. The Lund JETSET 7.3 program is used for final state parton showering and fragmentation.

Interferences between leptoquark production and deep inelastic scattering diagrams are included at the born level in the calculations of [27] as well as in the COMPOS generator. These interference terms become important only for masses above the center of mass energy and have been discussed in the framework of contact interactions [44][40]. Here the analysis will be restricted to $M_{LQ} < \sqrt{s}$, which means that the interferences imply only a minor modification of the results and will be ignored. Instead a better description of final hadronic states with higher order QCD corrections is considered to be more important for analysis up to $\int L\, dt = 100\, pb^{-1}$. For these reasons LEPTO 5.2 [45] has been used in order to generate the background from neutral and charged current interactions.

Set II of the EHLQ parameterization [28] is used for the structure functions $q(x, Q^2)$. The influence of this choice on the results in discussed in chapter 6.6. A matter of discussion in the literature is the question, which scale Q^2 has to be used for the evaluation of $q(x, Q^2)$. Most authors prefer to insert the 4 momentum transfer defined in equation 3, and this is also done in this text. An alternative would be [15], for example, to use the mass of the leptoquark itself.

4   Simulation of the H1 Experiment

4.1   The H1 Detector

The *H1* detector [47] is one of the two multi purpose experiments at *HERA*. A basic constraint for the apparatus is given by the asymmetric beam conditions. With momentums of 820 GeV for the protons and 30 GeV for the electrons the center of mass system is not at rest but moves with high velocity ($\beta \approx 0.93$) in the proton direction[9]. The detector layout shown in figure 13 is reflecting this asymmetry. The high center of mass energy and the Lorentz boost in the forward direction produce lepton and parton energies, which are often ranging up to several hundred GeV. The resulting, very narrow jets and large particle momenta stress the importance of calorimetric detectors in comparison to tracking devices.
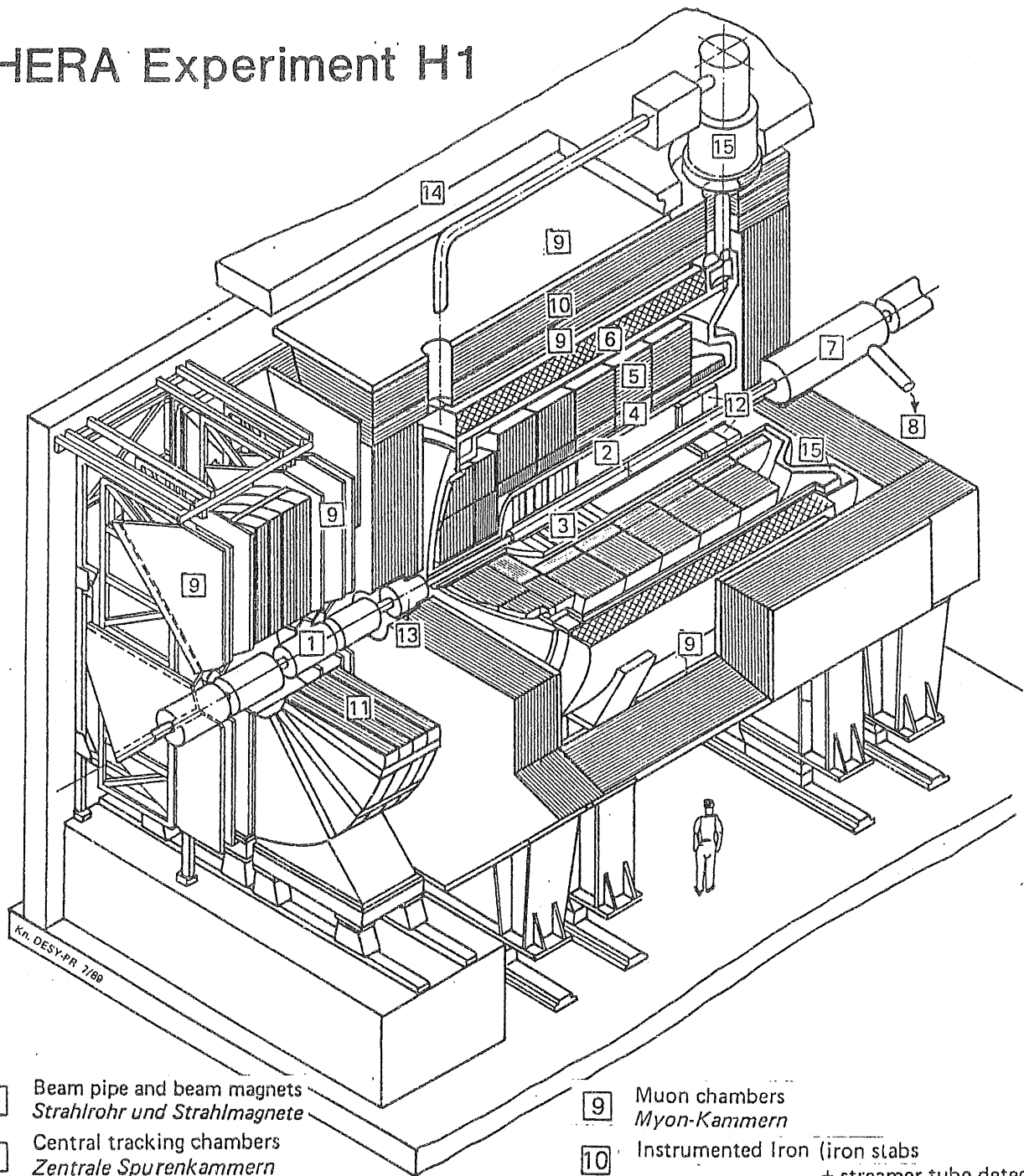
Here only a short overview of the different detector components will be given. Their expected experimental properties is demonstrated with help of the simulation program H1PSI in the next chapters.

- The inner tracking detector is divided into two separate components, the central tracker and the forward tracker. The central part is composed of an inner and an outer drift chamber (called 'jet' chamber) for the measurement of transverse momenta. They are combined with a backward proportional chamber and two drift chambers for the determination of polar angles such that charged particles between 15° and 176° are detected. Interleaved are detector layers for trigger purposes.

- For a good coverage in the forward direction down to 5° the central tracker is complemented by the forward tracking detector which consists of three supermodules with radial and planar chambers.

- These inner tracking detectors are embedded in a very homogeneous magnetic field of 1.2 Tesla. The superconducting magnetic coil surrounds also the main calorimeter. Thus the amount of inactive material in front of the electromagnetic calorimeter is minimized and, for the measurement of muons in the outer parts, the integrated field strength is increased compared to a smaller coil.

- The main calorimeter consists of a liquid argon– lead and liquid argon– iron sampling for the electromagnetic and hadronic part respectively. The calorimeter is not compensating, which means that the response for electromagnetic and hadronic interacting particles is different. This effect has to be corrected by weighting algorithms in the offline software. The whole liquid argon calorimeter is surrounded by a single cryostat.

---

[9]Throughout this text the coordinate system used is the standard *H1* system, which is righthanded and defined by the proton beam momentum as $P_{z\,p} = +820$ GeV, $\cos \vartheta_p = 1$. This will sometimes be called the 'forward' direction. The $+x$ axis is pointing to the center of *HERA* and the $+y$ axis is pointing upward.

HERA Experiment H1

1	Beam pipe and beam magnets *Strahlrohr und Strahlmagnete*		**9**	Muon chambers *Myon-Kammern*
2	Central tracking chambers *Zentrale Spurenkammern*		**10**	Instrumented Iron (iron slabs + streamer tube detectors) *Instrumentiertes Eisen (Eisenplatten + Streamerröhren-Detektoren)*
3	Forward tracking chambers and Transition radiators *Vorwärtsspurkammern und Übergangsstrahlungsmodul*			
4	Electromagnetic Calorimeter (lead) *Elektromagnetisches Kalorimeter (Blei)*	Liquid Argon *Flüssig Argon*	**11**	Muon toroid magnet *Myon-Toroid-Magnet*
5	Hadronic Calorimeter (stainless steel) *Hadronisches Kalorimeter (Edelstahl)*		**12**	Warm electromagnetic calorimeter *warmes elektromagnetisches Kalorimeter*
6	Superconducting coil (1.2 T) *Supraleitende Spule (1,2 T)*		**13**	Plug calorimeter (Cu, Si) *Vorwärts-Kalorimeter*
7	Compensating magnet *Kompensationsmagnet*		**14**	Concrete shielding *Betonabschirmung*
8	Helium cryogenics *Helium Kälteanlage*		**15**	Liquid Argon cryostat *Flüssig Argon Kryostat*

Figure 13: *The H1 detector.*

- In the backward region down to $173°$, a lead calorimeter with scintillator read out (called BEMC) is used to measure mainly the scattered electron.

- In the very forward direction between $0.6°$ and $3°$ the 'PLUG' calorimeter is supposed to detect remnants from the spectator jet of the proton.

- To achieve a good containment of hadronic showers, the iron return yoke for the magnetic field is interleaved with streamer tubes. The chambers surround all calorimeters and are used also to identify muons.

- In the forward direction outside the return yoke an additional high precision tracking detector with a toroidal magnetic field is added to measure the momentum of high energy muons.

- For luminosity measurements using the reaction $ep \rightarrow ep\gamma$, electron and photon detectors are inserted down the beamline in the electron direction.

All together the calorimeters extend down to $0.6°$ in the forward and $176°$ in the backward direction providing an excellent containment.

4.2 Parameterized Simulation (H1PSI)

4.2.1 Motivation and Requirements

The expected, extremely high electron– proton interaction rates (table 3) are one of the biggest difficulties in running the *HERA* experiments. This concerns the data acquisition as well as the analysis. In order to understand the errors of measurement caused by

interaction		event– numbers
DIS	$Q^2 > 5$ GeV^2	4×10^7
$c\bar{c}$	γ– gluon fusion	4×10^7
$b\bar{b}$	γ– gluon fusion	2×10^4
jet γ	photoproduction, $\hat{P}_T > 3$ GeV	5×10^4
jet jet	photoproduction, $\hat{P}_T > 3$ GeV	1×10^8

Table 3: *Expected electron– proton interaction numbers at HERA for $\int L\, dt = 100\, pb^{-1}$. $\hat{P}_T$ is the minimum transverse momentum of the partons in the hard scattering process.*

imperfections of the detector it is necessary for each acquired event to process several artificially generated events through a monte carlo simulation program of the detector. This is especially true for those processes where generators need to be tuned to the measured data. Also for the unfolding of structure functions from DIS data, iteration procedures with improved parton density functions might become necessary. Therefore,

the number of events that really have to be simulated might be by factors higher than the ones mentioned in table 3 (see also the discussion in chapter 4.4).

The CPU– time requirements for the most important *H1* computer programs are summarized in table 4 (see also figure 14). H1SIM [52] is an application of the GEANT–

program		CPU– time	event size
LEPTO 5.2 [45]	DIS event generator	≈ 0.05 s	≈ 5 kbyte
H1SIM [52]	detector monte carlo		
	detailed version	≈ 300 s	≈ 50 kbyte
	fast version (H1FAST)	30 - 100 s	≈ 50 kbyte
H1REC [51]	reconstruction program	1 - 2 s	≈ 100 kbyte
H1PHAN [50]	physic analysis program	≥ 0.03 s	≈ 0.5 kbyte
H1PSI [48]	parameterized simulation	0.05 - 0.1 s	≈ 20 kbyte

Table 4: *CPU time requirements per event and event size of the most important H1 programs for typical DIS events (IBM 3090, 1 processor).*

program [53], which tries to achieve a precise simulation of the detector behaviour by using an extremely detailed description of the detector geometry. All interactions of particles with matter are modeled using measured cross sections for electromagnetic [54] and hadronic [55] particles. This description obviously leads to an unacceptable slow simulation. Large effort has been spent to speed up the program (H1FAST) by averaging details of the geometry and by approximating the time consuming electromagnetic (and partially also the hadronic) interaction cascades by a parameterization of shower profiles. However in spite of a big improvement a real breakthrough has not been achieved.

The numbers in table 4 have to be judged on basis of the trigger rate, which is expected to be 5 s^{-1}. So, real events will be collected much faster than monte carlo events, unless computer resources far in excess of 150 IBM 3090 processors (or equivalents) are permanently available for simulations. Since this is not the case, the statistical precision of simulated events, and not of the actual data, might impose the most severe limitations for analysis.

For *H1* as well as for other experiments [56] this problem has led to the need for an alternative, much faster simulation concept [57]. Such a concept has to allow for a detailed simulation of all detector components in less than one second CPU– time. Because then the much slower reconstruction program H1REC would be the limiting step in the analysis chain, the concept has to include also reconstruction algorithms. Furthermore a simple and homogeneous environment for the following analysis requires that the same event data structures as in the reconstruction program are to be produced (figure 14).

HERA   event generator

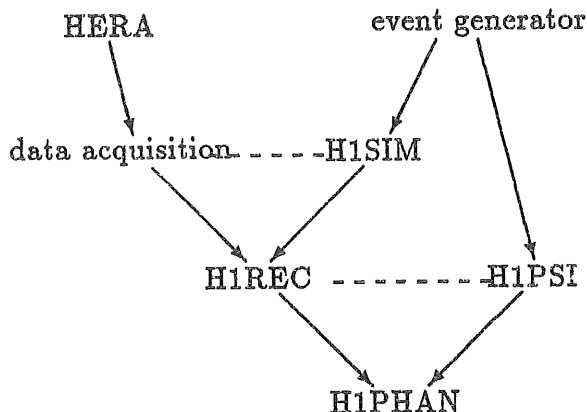data acquisition_ _ _ _ _ -H1SIM

H1REC - - - - - - - -H1PSI

H1PHAN

Figure 14: *Analysis programs for H1*

In the next chapters the program H1PSI [48] (Parameterized SImulation) will be presented, which forms a central part of this thesis project[10]. As already mentioned in table 4, this program is more than a factor 300 faster than H1SIM or H1FAST for typical DIS events.

Possible applications and limitations of the concept of a very fast (and therefore maybe also less accurate) simulation will be discussed in chapter 4.4. Recently, some analysis examples using H1PSI have been published in [49].

4.2.2   Concepts of H1PSI

Due to the extreme speed requirements for H1PSI, it is necessary to use a large number of approximations. These approximations must be chosen in such a way that the most important effects for following analysis steps are correctly reproduced:

- geometric efficiency,

- resolutions (gaussian and non– gaussian behaviour),

- correlation between the measurements of particles which are close together in space.

In standard simulation programs most of the calculation time is spent in geometric operations in the complicated structure of the calorimeters. Pattern recognition and helix fitting in the tracking chambers however limit the speed of reconstruction programs. The most important concluding simplifications for H1PSI are summarized here and will be commented in greater detail in the corresponding chapters:

---

[10]Already here, i would like to thank all those who contributed to this program

- In all components the detector is treated as cylindrical symmetric around the beam axis.

- Separately for many small volumes, the material is described by average values of the corresponding densities, radiation length and interaction length.

- The magnetic field is homogeneous and constant within the tracker volumes and neglected in the calorimeters.

- The results of all detector components are reconstructed, calibrated quantities. Intermediate calibration steps are neglected.

- Within the tracking detectors no single ionization hits are produced but the track parameters are fluctuated according to the resolutions of the different chambers.

- All calorimeter cells are projective with respect to the vertex. The full read out granularity is kept in the lateral direction and reduced by about a factor 1/3 in the radial direction.

- The energy deposited in calorimeter cells by electromagnetic and hadronic showers are calculated using lateral and longitudinal shower profiles.

Program Lay Out In order to realize these features H1PSI is split into three consecutive parts. In the 'General Tracking Module' all particles are tracked from the vertex to the inner surface of the calorimeter. In the 'Subdetector Modules' the response of all detector parts is determined using the information from the first part. Finally these results are combined together in the 'Reconstruction Modules'. A more detailed flow diagram of the program is shown in figure 15.

Fragmentation products of the spectator jet generally have very small scattering angles with respect to the beam direction. The reason is again the specific kinematic situation at *HERA* with the center of mass system moving fast in the proton beam direction. In practice this means that most of them never enter the active parts of the detector but disappear in the beam pipe. In order to save computing time these particles are suppressed from the very beginning (compare figure 15).

Charged particles with momenta below ≈ 150 MeV are bended by the magnetic field such that they are curling inside the tracking detectors. The pattern recognition of the reconstruction program will therefore frequently fail to detect these particles. When they are finally leaving the track detectors through their ends at high or low z, they deposit almost all of their energy in the cryostat and support material in front of the active parts of the calorimeter. Therefore these particles are also neglected a priori in the simulation which further reduces the necessary CPU time.

Inside the inner tracking detectors, the material density and specifically the number of radiation length a particle has to transverse is relatively small (compare figure 17). This implies that here energy losses due to ionization and changes in direction due to multiple scattering are disturbing the particle trajectory only slightly. Especially for the calculation of geometric acceptances or of track lengths inside active volumes these
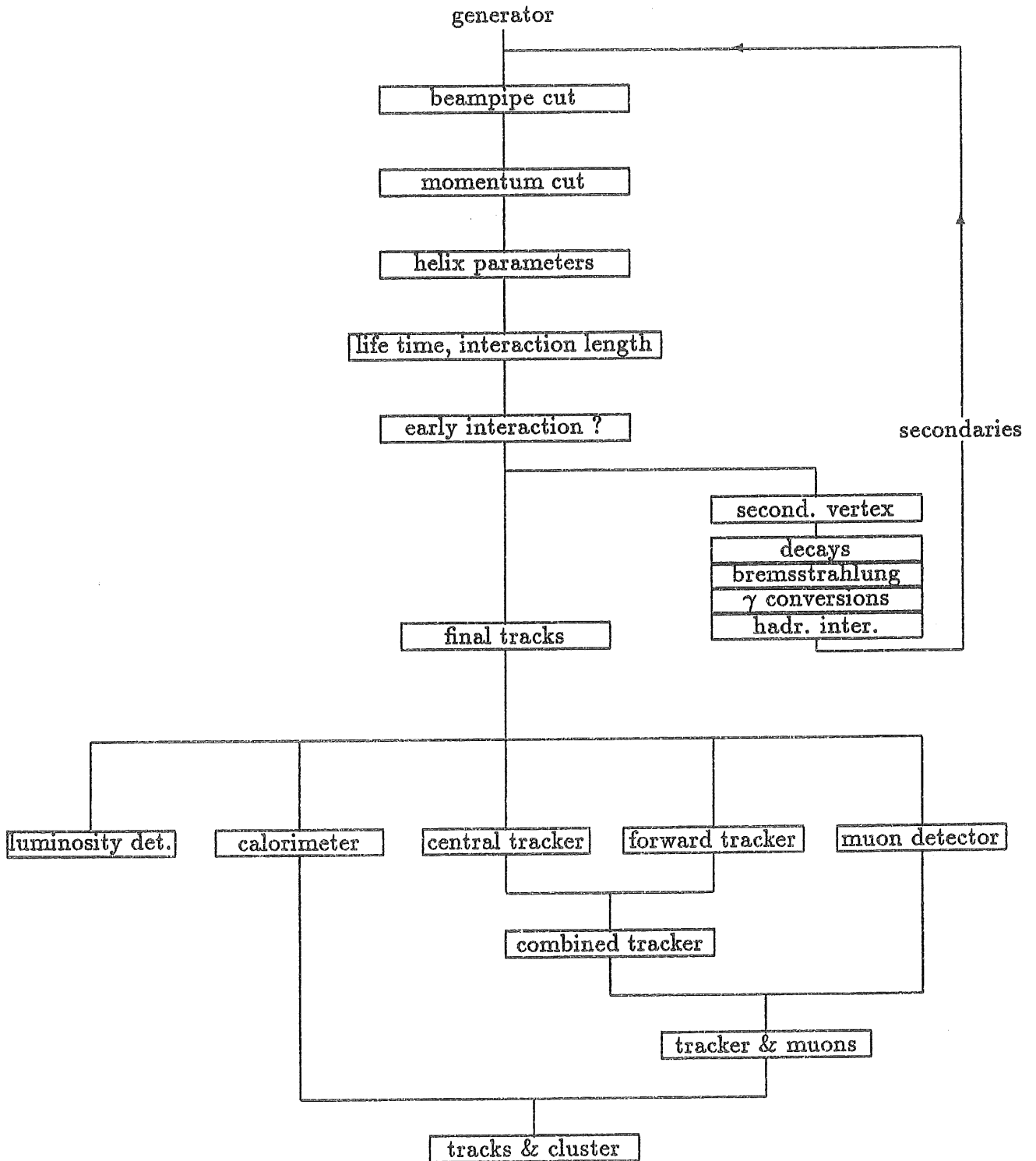
generator

beampipe cut

momentum cut

helix parameters

life time, interaction length

early interaction ?

secondaries

second. vertex

decays
bremsstrahlung
γ conversions
hadr. inter.

final tracks

luminosity det.   calorimeter   central tracker   forward tracker   muon detector

combined tracker

tracker & muons

tracks & cluster

Figure 15: *Flow diagram for the program* H1PSI. *See the text for explanations.*

effects may be neglected. Multiple scattering only becomes important if hits have to be produced along the trajectory. In a helix fit to these hits, the displacement of the hits would then dominate the momentum resolution at low incident momentum. In H1PSI however, no hit positions in the tracking devices are calculated. For the resolutions of the chambers (see chapter 4.3.2), analytical expressions are used containing for the multiple scattering dependence only the total number of radiation length passed by the particle. This means that the determination of the overall trajectory in the simulation has not to be precise on the level of hits. So the particle does not have to be tracked in a very time consuming way ($\approx$ 10s in H1FAST) in small steps through the detector materials updating after each step the momentum vector. The trajectories are merely described by a single set of helix parameters which are valid until the first inelastic interaction or a possible decay.

At the very beginning of the calculations the time of flight before a possible decay is determined together with the number of radiation or absorbtion length until the first interaction. The low density of materials inside the tracking volumes indicate that such an interaction happens for most particles only in the calorimeter. This is checked very early, and if so, the particle is not tracked in detail through the inner detectors, as discussed above. All other particles are followed step by step through the cylindrically approximated tracking chambers until they undergo one of the following interactions:

- a decay ($\mu, \pi, K, ...$)
- a $\gamma-$ conversion to $e^+ e^-$
- a bremsstrahlungs process (electrons only)
- a secondary hadronic interaction (not yet implemented).

In all these cases routines from GEANT have been adopted. The secondary particles created that way are fed in the particles buffers and are treated in just the same way. This procedure continues until all particles have either interacted or reached the calorimeter.

At this stage, the 'fate' of the event is completely determined in the sense that all detector effects which might change the event topology are known. This can be used to reduce the number of events to be simulated if one looks for unusual sources of background (see chapter 4.4).

Up to here only the trajectories of the particles are predefined. This information is thus decoupled from the response of the various detector components, which are calculated in separate, stand alone modules.

The basic ingredient for the simulation of the central and forward tracker, the calorimeters, the muon detectors and the luminosity system is the particle state vector at the beginning of the active volumes and the track length until the volumes are left. These parameters are obtained by each module individually in calling a utility routine which is using the predetermined fate of the particles.

Only in a last step, the measurements of all subdetectors are combined and stored in a form equivalent to the one produced by the reconstruction program H1REC.

The high degree of *modularity* inside the program also means an additional speed up. So it it possible to switch on or off any detector component or particle interaction without interfering with the results of other parts of the apparatus. This allows the rejection of events already on basis of specific detector effects and it is not necessary to simulate the full event (see chapter 4.4).

The modularity also implicates *parallel tracking of particles*, which means that each module treats all particles in one single call. As an example, this permits the use of random generators which produce vectors of random numbers. Effectively, these are around a factor 3 faster than scalar versions.

Generally, most parts of the simulation involve calculations which have to be repeated for all particles again. Examples for this are geometric operations in the calorimeter, integration of shower shapes, energy loss calculations for particle identification, etc. To save CPU time, these calculations are either carried out in the initialization phase of the program, or their results are read in from a database. In both cases, the results have to be stored thereby increasing the necessary memory to almost 3 megabyte. This is considered to be tolerable in comparison to the gain in computing time.

4.3 Properties of the H1 Experiment

In this chapter features of the *H1* detector are discussed which are relevant for the understanding of experimental results. This is done by means of the simulation program H1PSI, which is understood to describe all necessary effects.

4.3.1 Geometry

For H1PSI a data base has been set up containing information about the basic geometric properties of the *H1* detector. This includes all information to calculate the frequency of secondary interactions and the shape of calorimeter showers, such as geometric boundaries, energy losses, radiation— and absorbtion length. The numbers are obtained from the very detailed descriptions used for H1SIM but averaged with respect to the azimuthal angle φ [58]. Technically this was done by tracking particles ('geantinos') through the detector and averaging along their path the materials as obtained from the GEANT geometry description.

The inner detector is approximated by 24 cylinders representing the most prominent active and passive zones in the forward and central tracker including the backward proportional chamber BPC (figure 16). Each volume is chosen such that its material density is fairly homogeneous or, where this is not possible, the volumes are small enough to allow a reasonable precise description. Figure 17 shows the amount of material
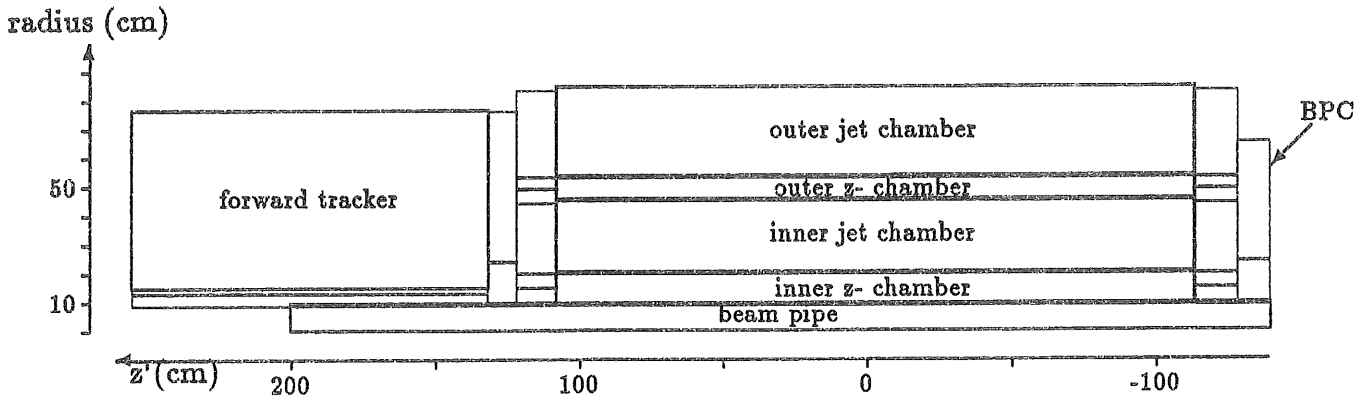
radius (cm)

Figure 16: *Geometric volumes in the tracking chambers used to describe material densities. The interaction vertex is at $z = r = 0$, the proton beam is entering from the right side as in all following figures showing the detector. The volumes between the BPC and the jet chambers and in front of the forward tracker contain read out and support structures with high material densities (compare figure 17).*
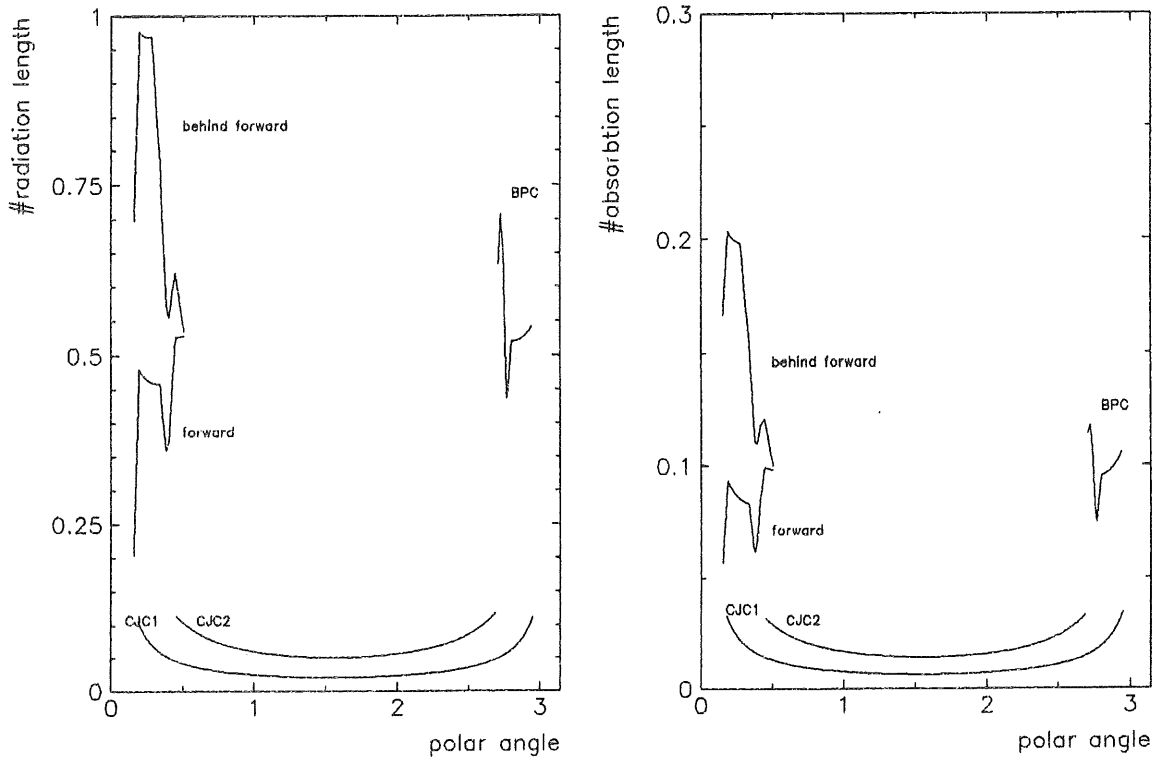

Figure 17: *Material densities between the vertex and the inner jet chamber CJC1, the outer jet chamber CJC2, the backward proportional chamber BPC, the forward tracker and including the forward tracker itself.*

which a particle, coming from the nominal vertex, has to transverse before entering the different tracking chambers.

In front of the central jet chamber CJC1 there are ≈ 0.03 radiation length. Especially in the forward direction at $\vartheta \leq 30°$, the material density is high and there will obviously be very many and sometimes even multiple, shower– like electromagnetic interactions.

The calorimeters in H1PSI are described as projective towers pointing to the interaction vertex (figure 18). Also here the geometry is approximated by cylinders. The octagonal structure of the liquid argon/ iron return yoke calorimeter and the rectangular shape of the backward calorimeter cells are thus neglected. This is unavoidable to guarantee a fast simulation. In the following the geometry used for the description of the material distribution and the one for the read out cell structure are discussed separately.

The material parameters are sampled in 100×128 bins in polar angle ϑ and azimuthal angle φ. This choice is motivated by the small size of the read out cells in the liquid argon calorimeter (compare chapter 4.3.3). The φ– bins are chosen equidistant, the ϑ– bins are adjusted in 11 different regions to the changing granularity of the electromagnetic calorimeter. For each $\vartheta - \varphi$ bin, six longitudinal segments are introduced to describe (figure 18) from the outside to the inside

- the instrumented iron and plug calorimeter
- the layer in front of the instrumented iron and plug calorimeter (coil,...)
- the hadronic calorimeter
- the electromagnetic calorimeters
- the layer between tracker volumes and calorimeter
- the tracker volumes (not displayed)

The edges in figure 18 between the innermost and the second layer origin from the fact that the first layer is defined as the end of the active tracker volumes. Visible is thus for example the material between central and forward tracker as a spike in the second layer.

All these layers are assumed to be intrinsically homogeneous enough to allow a consistent description of shower developments. Figure 19 gives an overview of the containment properties of the *H1* detector for the different calorimeter layers in terms of number of radiation length and absorption length. Due to the large amount of material in front (1 - 2 radiation length), the electromagnetic energy measured in the calorimeters is reduced by 5 – 10 %. In many cases the hadronic calorimeter will also not contain all the shower energy but corrections must be applied with help of the calorimeter in the iron return yoke.
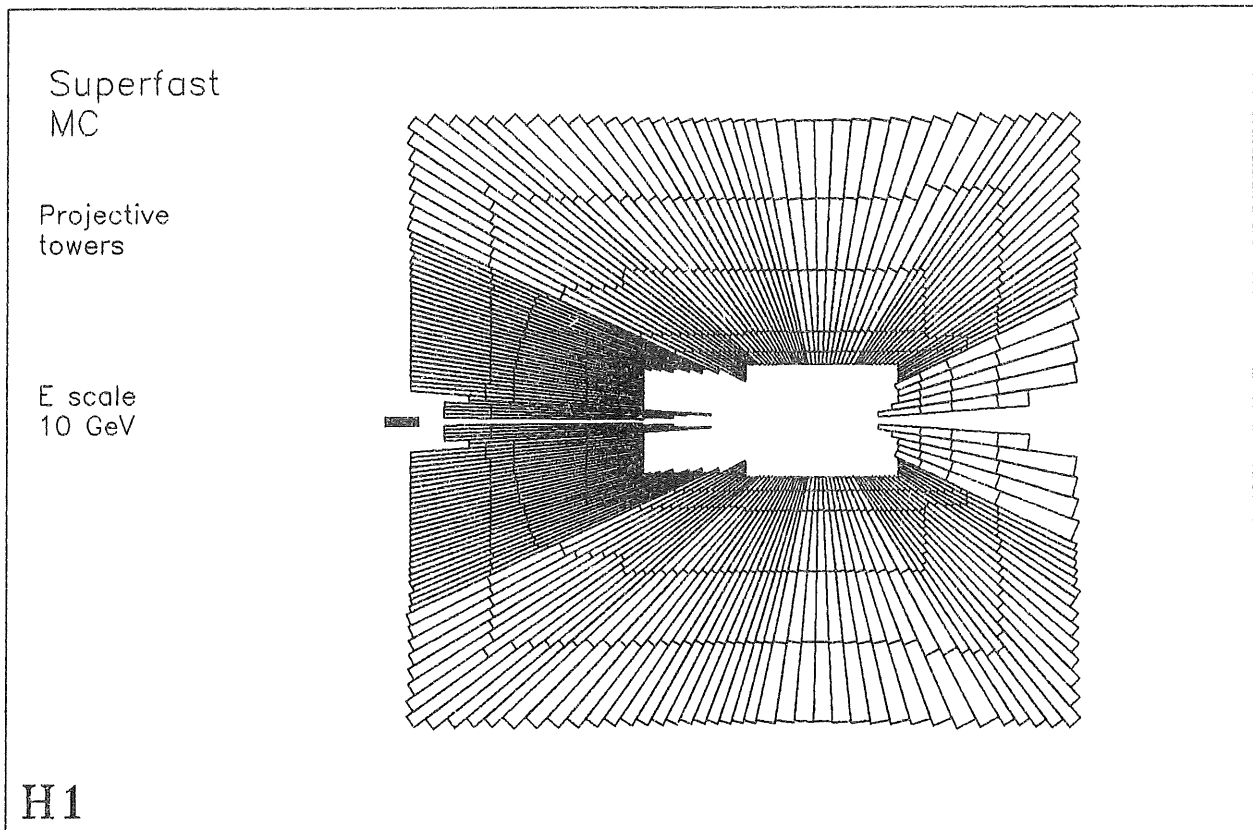
Figure 18: *Sampling of materials in the calorimeter for* H1PSI. *Shown are the outermost 5 layers of the geometric description. The stacks are pointing to the interaction vertex. Their segmentation in polar angle depends on the the read out structure of the H1 detector (see text).*

4.3.2 Tracking Chambers

In case of the tracking chambers it is not possible to produce individual ionization hits, since even in a simplified geometry this would increase the computing time by more than a second. In addition, the pattern recognition and fitting procedures of the reconstruction program H1REC need about 0.5 seconds.

In H1PSI, the simulation is performed without referring to single hits. The basic properties of the tracking chambers are

- the geometric acceptance
- the efficiency for a hit
- the hit resolution
- the double hit resolution
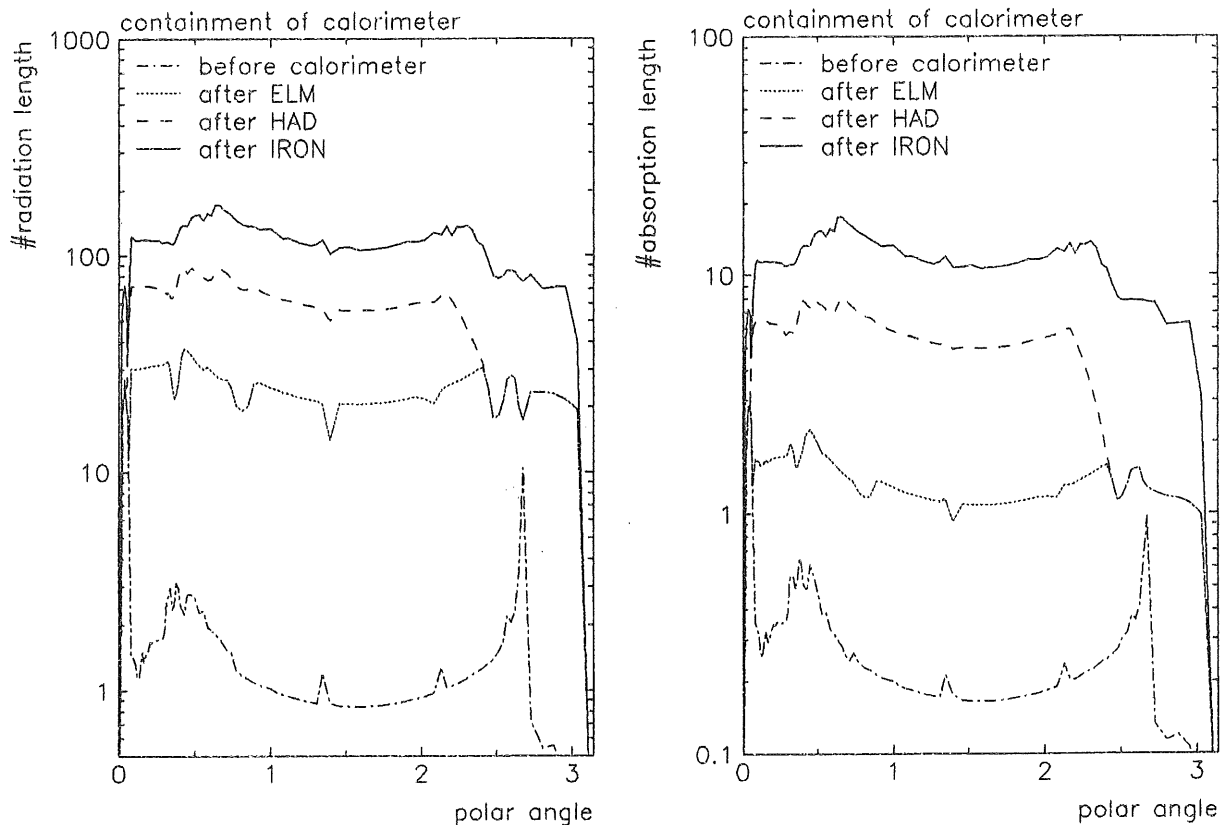
Figure 19: *Containment of calorimeters in radiation and absorption length for a particle starting at the interaction vertex. 'ELM' is the electromagnetic, 'HAD' the hadronic calorimeter and 'IRON' denotes the streamer tube calorimeter in the iron return yoke of the magnet. In the backward region, there is no hadronic calorimeter.*

● multiple scattering in front of and inside the chamber.

The momentum and the angular resolutions have to be evaluated in dependence of all these items. Once they are known analytical formulae can be used to determine the resolutions of the final track parameters and to smear these accordingly.

Central tracker   For the simulation of the central tracker the geometry is approximated as a double cylinder. For each charged particle, the total track length inside the two jet chambers is used to determine the number of hits. For particles between $37^\circ < \vartheta < 142^\circ$, up to 64 wires may collect charge. The efficiency of the chamber is taken to be 90%.

The track reconstruction inside a dense jet is limited since hits might not be assigned to the right track and the spatial resolution of hits is reduced. This correlation between

two or even many particles is taken into account by a simple model for the double track resolution, which reduces the effective number of hits for the contributing tracks. The double hit resolution efficiency ϵ in the $x - y$ plane is assumed to be a linearly rising function of the distance d between two tracks

$$
\epsilon = \left\{ \begin{array}{ll} 0 & \text{if } d < a \\ (d-a)/(b-a) & \text{if } a < d < b \\ 1 & \text{if } b < d \end{array} \right.
$$

where the parameters a and b are determined to 1mm and 2.7mm respectively. Since in practice no hits are produced, all tracks are extrapolated to three given radii. At these three master points, the distances between all pairs of tracks are determined. For a pair of nearby tracks which are within double track resolution, either partly or along their whole length, one track is chosen randomly and the track piece within double track resolution is suppressed. This leads either to a reduction of the number of hits, or, if the remaining number of hits is below $N_{cut} = 3$, to a complete loss of the track. The z-coordinate is measured much worse and is not taken into account here.

Following ref. [59] the resolution for the curvature measurement $\delta \left(\frac{1}{r} \right)$ is then given by

$$
\delta \left(\frac{1}{r} \right) = \sqrt{ (\delta x)^2 \, l'^4 \, \frac{720}{N+5} + \frac{\sigma_{ms}^2}{l^2} }
$$

where $\delta x = 0.015$ cm is the hit resolution in the $x - y$ plane, N is the effective number of hits, l' is the track length projected on the plane transverse to the magnetic field, l is the total track length and σ_{ms} is a measure for multiple scattering depending like $1/P^2$ on the incident momentum (see [30] for details). Similar equations are used for the resolutions of angular measurements and distance of closest approach to the z axis [48]. The measurement of the z- coordinate at the vertex and thereby the polar angle are dominated by the precision (± 0.3mm) of the z- chambers which are interleaving the jet chambers. At high ϑ, the backward proportional chamber measures the x, y position to about ± 0.2cm, which determines the angular resolution in this region.

Forward tracker The forward tracker consists of three supermodules each of them containing planar and radial chambers. The pattern recognition and the momentum resolution of the forward tracker depends to a large degree on the three radial chambers [60]. The planar chambers are mainly used to resolve ambiguities in linking track elements of different modules.

Similar to the procedure described for the central tracker, particles are extrapolated to the radial chambers. These are approximated as a plane perpendicular to the beam direction. For each particle the wire number and the drift length to it are determined. If the drift length difference of other tracks at the same wire is smaller than 2mm, the information of this radial chamber is assumed to be useless for both particles. So due to double track resolution, and of course geometric acceptance, less than three radials

will influence the momentum resolution. Due to the different lever arms with respect to the vertex the parameterization of the error of the momentum P is

$$\delta\left(\frac{1}{P}\right) = F \sqrt{a^2 + \left(\frac{b}{P}\right)^2} \; \frac{c}{\tan\vartheta}$$

where ϑ is the polar angle and F is a scaling factor describing the number of contributing radial chambers:

$$F = \begin{cases} 1 & \text{if the first and the last radial contribute} \\ 1.5 & \text{if the first two or the last two radial contribute} \\ 2 & \text{if only one radial contributes} \end{cases}$$

The parameter a corresponds to the chamber resolution. b is determined by multiple scattering which is of special importance here because the region between the central and forward tracker alone contains about 1/2 of a radiation length, as can be seen from figure 17. c is a geometric constant. The parameters have been determined from a fit to the results of the pattern recognition program in H1REC [60].

Combining Central and Forward Tracker   In a certain angular region particles are measured both in the central and in the forward tracker. Assuming that ambiguities in the linking step of track elements can be resolved, the track parameters of both detectors have to be combined. This is done by taking the weighted mean of both measurements for the curvature and the angles. The distance of closest approach and the $z-$ coordinate at this point however are taken from the central tracker alone since there is a lot of multiple scattering in front of the forward tracker.

The resulting momentum resolution as function of the momentum of the particle and the polar angle is shown in figure 20. The number of hits in the central tracker is maximum in the central region between $\approx 50°$ and $130°$ degrees and leads to a resolution for the transverse momentum P_T of $\delta(1/P_T) \approx 0.003 \; \text{GeV}^{-1}$ for high energetic particles. Towards the ends the geometric efficiency is reduced, until at $\approx 30°$ the forward tracker starts to dominate the measurement. The edges in the resolution at even lower angles are explained by the geometric position of the radial chambers of the forward tracker.

4.3.3 Calorimetry

All the different calorimeters of *H1* are not compensating, which means that their response is different for hadrons and for electromagnetic interacting particles of the same energy. A shower originating from a hadron generally also has an electromagnetic part through the creation of $\pi°$ or η. This fraction is energy dependent and shows large fluctuations. leading to deviations from a linear response and distortions of the energy resolution. For *H1*, this effect is compensated in the reconstruction program by identifying the electromagnetic component in a shower and reweighting it properly. The
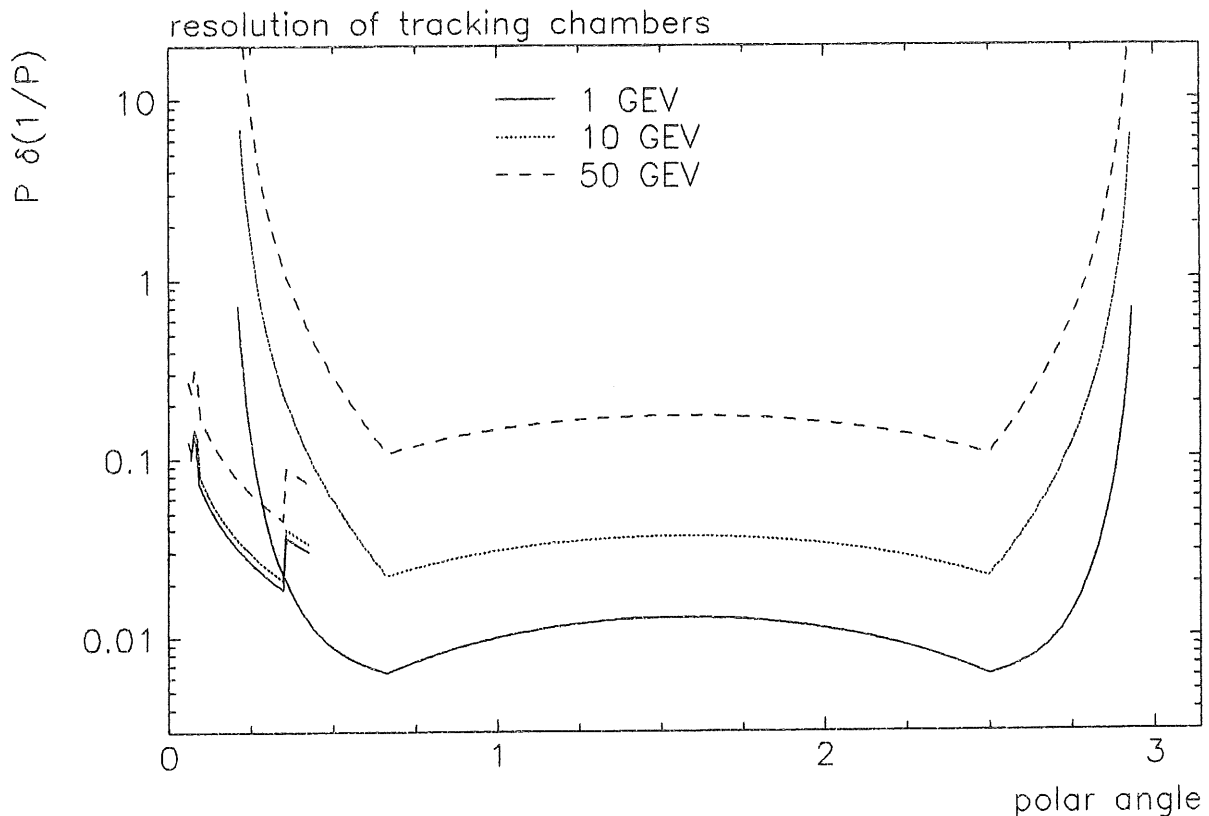
Figure 20: *Momentum resolution of the tracking chambers in dependence of polar angle and of the incident momentum. The measurement of the forward tracking detectors dominates at low polar angle the resolution of high momentum particles.*

identification depends entirely on a precise description of the internal structure of the shower development and a fine granularity of the calorimeter. The resulting energy resolutions for the liquid argon calorimeter after this correction are given in table 5 together with the measured resolutions of the other calorimeters.

In H1PSI there is no time for a detailed shower simulation with thousands of particles and also the geometry is approximated. Therefore, a weighting algorithm does not seem feasible. It is merely recommended to simulate directly the final, measured energies as obtained after all calibration steps and after the weighting procedure.

In addition to this, it is also required to get a realistic description of shower shapes and of the primary measured, 'visible' energy depositions used for the calorimeter triggers. Both are strongly influenced by the π^0 fluctuations and also by energy losses through nuclear breakups, etc. (called invisible energies).

The shower description in H1PSI follows closely the model described in [61], which has been developed for the simulation of the *H1* calorimeters in H1FAST.

Calorimeter	for electrons	for hadrons
Liquid Argon unweighted weighted	0.12 0.12	0.55 0.44
BEMC	0.12	1
Plug	–	1
Iron yoke	–	1

Table 5: *Energy resolutions of calorimeters. Given is the constant c in the parameterization* $\frac{\sigma_E}{E} = \frac{c}{\sqrt{E}}$.

Rather than simulating individual particles inside a shower, only the overall shower shape is considered. Following this reference, the deposited energy of showers may be factorized in longitudinal and lateral functions

$$d E_{dp} = f_{dp} E_0 \, f(z) \, dz \, f(r) \, dr \, f(\varphi) d\varphi \tag{18}$$

where $f_{dp} \leq 1$ reduces the primary particle energy E_0 by the invisible energy of hadronic showers.

For electromagnetic showers, the factor f_{dp} is 1, z is the distance along the shower axis measured in radiation length, r is the distance to the shower axis measured in Moliere radii and φ the corresponding azimuthal angle.

The mean longitudinal energy profile of electromagnetic showers can be described by a gamma function

$$f(z) = \frac{(\beta z)^{\alpha-1} e^{-\beta z}}{\Gamma(\alpha)} \tag{19}$$

with energy dependent parameters α and β. The radial profile f(r) is parameterized as

$$f(r) = \frac{2r R_{50}^2}{\left(r^2 + R_{50}^2\right)^2}. \tag{20}$$

Again R_{50} is a parameter depending on energy and shower depth

$$R_{50}(z, E) = [R_1 + (R_2 - R_3 \ln E) \, z]^n. \tag{21}$$

with $n = 2$ for electromagnetic and $n = 1$ for hadronic showers. R_1, R_2 and R_3 are constant parameters. No azimuthal dependence is considered

$$f(\varphi) = \frac{1}{2\pi}. \tag{22}$$

For hadronic showers the ansatz chosen is to split the complete longitudinal shape in three components, namely a purely hadronic component, an early π^o component

originating from the first hadronic interaction, and finally a late π^o component created by further inelastic interactions of hadrons. Both the first and the last part are not scaling with radiation but with absorbtion length. They are parameterized in the same way as the purely electromagnetic cascades, but of course with different parameters α and β. Therefore the relative ratio of the three components determines the overall longitudinal shower shape.

The factor f_{dp} is less than 1 for hadrons and depends strongly on the size of the hadronic component. For this reason f_{dp} and the hadronic fraction are fluctuated in correlation to each other. Then, the relative ratio of the early and the late π^o component are smeared too.

All parameters (α, β, f_{dp}, R_{50}) are determined from fits to results of detailed simulations and experimental data [62].

In the more general attempt of [61] also other parameters like R_{50} and the different α and β are fluctuated taking into account also possible correlations between the parameters. This however is neglected for the fast simulation required in H1PSI. In total this means that

● the lateral shower profile depends on the incident energy only and is not smeared

● the longitudinal shower shape is determined by the randomness of the shower starting point and of the size of the π^o components.

For the trigger read out, charges are calculated by applying sampling fluctuations for either hadrons or electrons to the various shower components.

For the calibrated and weighted response, the energies are simply scaled in order to correspond to the measurement errors given in table 5.

After the determination of the shower shapes and the energy smearing, the energies have to be deposited in the calorimeter cells. In order to save computing time in this mapping procedure, the approximated geometry of figure 18 is used, with each material tower beeing one cell. The correspondence between both simplifies greatly the calculations.

It is further required by computing time constraints, that the axis of the shower development has to be parallel to the tower structure, and is thus always pointing away from the interaction vertex. Essentially this means that for charged particles, the bending of the magnetic field is considered only for the determination of the impact point to the calorimeter. It is however neglected inside the calorimeter. This leads to an underestimation of the azimuthal shift of the shower due to the magnetic field. Taking the dimensions of trackers and calorimeters into account, the most prominent bending effect however is simulated[11].

---

[11]For a cluster (see below) with a charged track pointing to it, this is no problem, because the direction should anyhow be determined from the much better measurement in the tracking devices. In regions with high particle densities (jets), it will be difficult to assign individual tracks to clusters. Due to neutral particles in the jet, the calorimeter information is preferred here, and only then the bending effect enters. In any case, the displacement is small for high momentum tracks, while low momentum particles are stopping rather soon in the calorimeter, which also diminishes the effect.

In practice, the simulation of the energy deposition is done in several steps:

- Determination of the shower starting point for the individual particle.

- Ionization losses (dE/dx) in the calorimeter cells up to the shower starting point. Straggling is taken into account.

- Energy smearing and determination of the fluctuations for the longitudinal profile as described above. The increase of the measured energy due to annihilation in case of an incident anti- baryon is taken into account.

- Integration of the longitudinal profile within each calorimeter cell. This is done by interpolating in a table containing the integrated gamma function.

- Spreading of the shower energy corresponding to the lateral profile. The cylindrical symmetric shower has to be mapped to the $\vartheta - \varphi$ grid of the calorimeter description. This is done by an analytical approximation instead of really integrating the lateral profile in each cell.

- Mapping to read out cells.

Concerning the last item, the geometric description of materials described so far does not correspond to the real read out structure of the calorimeters of *H1*, but is chosen to allow a reasonable fast simulation of the shower development. Therefore, this discrepancy is reduced by an additional mapping of the energies to the new read out cells shown in figure 21.

For the dimensioning of the read out cells in H1PSI, the aim is to keep the fine granularity of the *H1* detector in lateral direction in order to allow studies of shower overlaps. Therefore, as in reality, the lateral size of cells in ϑ and φ varies strongly with the layer number and ϑ. For timing and space reasons, the longitudinal segmentation however is reduced by roughly a factor of 3. So there is only one layer for the electromagnetic, hadronic and iron return yoke calorimeter, while in reality there are 3-4, 4-5 and 2 layers respectively (figure 21). Since the lateral size of the 'material towers' is always smaller or equal to the size of the read out cells, the deposited energies are easily mapped to the read out structure (compare figure 18 and 21).

The energy losses in the 'dead' materials in front of the electromagnetic layer and the iron yoke calorimeter have to be corrected for in the reconstruction program. In H1PSI this is done for the final calibrated and weighted response by (up to now) simply adding these energies to the active layers, at least in case some energy has been deposited there.

For the simulation of the trigger response, this correction should not be applied. Instead it has to be considered, that the information of the very first layer of the electromagnetic and the very last part of the hadronic calorimeter is not used everywhere in the trigger. This fine segmentation does not exist in H1PSI, but is taken into account in the integration steps of the longitudinal shower profile.
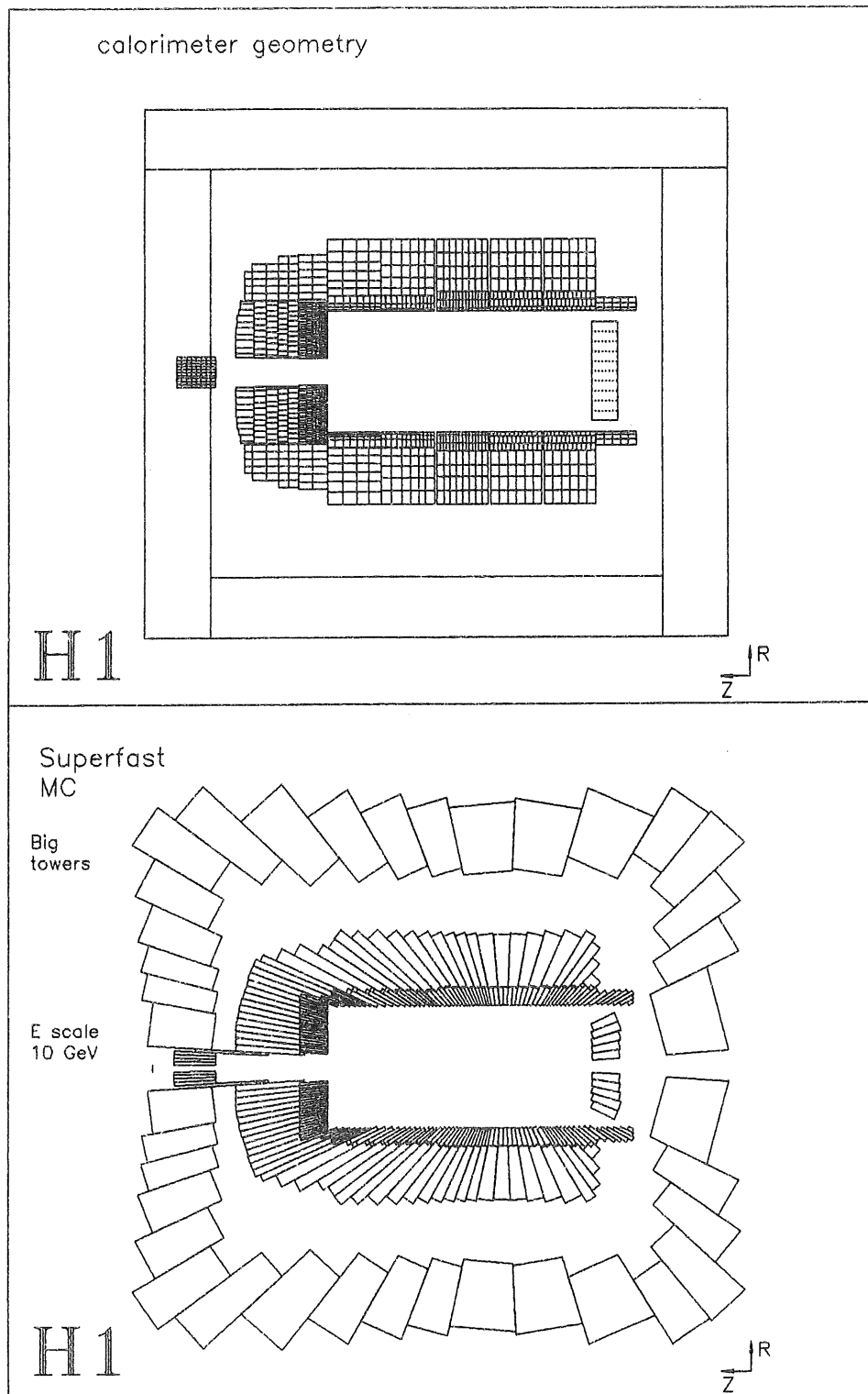
Figure 21: *Comparison of the calorimeter read out structure of H1 (top) and the approximation made in* H1PSI *(bottom). Details of the streamer tube system are not displayed in the top figure.*

Finally, for each event the overall energy distribution is analysed by a cluster[12] algorithm [63]. Starting in the electromagnetic part cells with the highest energy densities are building the start of a 'cluster' and connected cells are added until an increase in energy density is observed. This carries on until all cells are joined to clusters. In the next layers, cells are either added to what is lying in front of them or form new clusters.

4.3.4 Lepton Identification

Muon and especially electron identification is of great importance for physics analysis at HERA. In both cases information of single detectors together with correlations between measurements from different parts of the apparatus will be applied. Here only the first item will be discussed because the latter step is only carried out in the physics analysis program H1PHAN.

dE/dx The central tracker read out allows to measure the ionization on single wires. This leads to the possibility of separating electrons, muons and pions from heavier particles in the low momentum region. Here a parameterization is used [64][30] to describe the fluctuations of the truncated mean of the ionization losses, which depend on the number of wires and the effective track length for each wire. With this result the probability of (mis)identifying the particle as an electron, muon, pion, etc. is computed.

Transition Radiation Within each of the three supermodules of the forward tracker, transition radiation layers are inserted. The photons are measured as additional ionization in the radial chambers. The resulting efficiencies for electron identification are parameterized [65] from data of the full simulation program H1SIM. At 5 GeV (60 GeV) the pion contamination is less than 1% (10%) for an electron efficiency of 90%.

The Calorimetric Particle Identification depends on the rather different shower profiles for electrons and hadrons. A detailed analysis of these shapes relies entirely on a correct description af all shower fluctuations and on a fine sampling of the read out structure of the calorimeter. Both are only approximated in H1PSI. It has however been shown that just the 'electromagnetic fraction', here defined as the ratio of energy in the electromagnetic calorimeter with respect to the total measured energy, allows a separation of electrons and pions at a level of better than 10^{-2}. This is simply explained by figure 19 showing that the width of the electromagnetic calorimeter only corresponds to $\approx 2\lambda$. This ratio is not very sensitive to details of the geometry and depends mainly on the π^o fluctuation in the hadronic shower simulation, which is rather well described. It is however clear that a more detailed investigation of shower profiles in H1PSI is not

---

[12]In the reconstruction these clusters are used to apply weighting algorithms, which is not necessary here.

reasonable. For the future it is envisaged to parameterize directly the misidentification probability of a generated particle.

In any case the search for electrons, and namely the scattered electron, should be cross checked by alternative methods like isolation criteria or kinematic constraints. These will be discussed in chapter 5.

The Muon System consists out of the forward muon spectrometer and of the streamer tubes in the magnetic return yoke. Similar to the treatment of the inner detectors no complete tracking can be done. Especially the extrapolation of the tracks through the dense material of the calorimeter would be too time consuming.

An approximation for the momentum cut off of particles reaching the muon system has been obtained from the detailed simulation. The results are determined in dependence of the polar angle and averaged with respect to the azimuthal angle φ. The momentum cut off ranges from below 1 GeV in the backward direction (no hadron calorimeter) to almost 2 GeV in the forward region for the instrumented iron. The first detector layer of the forward muon system in front of the toroid is reached by particles with more than 2.8 GeV, and the layer behind requires 5 GeV.

While the geometric efficiency of the toroid system may be considered as perfect, the situation is rather complicated in case of the irregularities of the streamer tube chambers. Therefore, the geometric efficiency of the instrumented iron is averaged in φ and sampled in bins of polar angle ϑ with help of the full simulation program H1SIM. This is done for each of the 16 chamber layers individually with respect to the wire and the strip read out. For each particle, the number of hits are then fluctuated neglecting correlations between the two types of information. A cut on the required number of wires and strips is then applied as a threshold against noise. A particle is considered to be identified as a muon if it has survived these cuts.

The forward muon system is measuring with high precision also the particle momentum. A parameterization similar to the one for the inner tracking detectors is chosen [66]. In contrast, the cell size of the streamer tubes of about 1cm allows only a very limited momentum resolution. Implemented are effects for multiple scattering in the iron and the toroid, stopping muons, the spatial resolution of the chambers, the variation of the magnetic field and the number of wires beeing hit by the muon.

4.3.5 Luminosity Measurement

The luminosity system of *H1* consists of an electron tagger in the electron beam direction at $z = -33$m and a photon detector even more downstream at $z = -102$m. Particles can thus be detected at polar angles $\vartheta > 180° - 0.28°$ and $\vartheta > 180° - 0.028°$ respectively. The energy resolutions are either parameterized empirically, but also a more detailed shower simulation is possible [67]. The massive shielding (3.5 radiation length) in front of the photon detector is taken into account as a probability for reaching the detector without interactions.

4.3.6 Trigger

Beside synchrotron radiation from the electron beam, interactions of protons with the remaining gas and of the proton beam halo with the material of the beam pipe are expected to be severe sources for background events.

The last item, probably the more important one, imposes severe problems for a simulation in H1PSI. Interactions with the beamwall are most often taking place a few meters in front of the nominal interaction region. Secondary hadrons are then scattered through the material in the BEMC region producing sizeable energies in the backward detectors. Often particles are also entering the tracking detectors and are finally hitting the forward parts of the calorimeters. In H1PSI however, hadrons are only described via their shower shapes, and no individual secondaries are produced. This means, that for this type of background events, H1PSI cannot be used. The simulation of the trigger response for beam gas interactions and for electron– proton events however is possible.

The high luminosity and bunchcrossing rates at *HERA* require rather complicate trigger setups. In *H1* up to four consecutive trigger levels are envisaged. The main rejection of events happens at level 1 which will reduce the trigger rate to approximately $50s^{-1}$. While level 2 and 3 are foreseen to be implemented only later, the level 4 is a software trigger running on a multiprocessor farm. The use of algorithms, which are as close as possible to the final reconstruction program, will enable detailed investigations of event topologies such that the trigger rate can be reduced to $5s^{-1}$. This is the limit for data transfer from the experiment to the storage media. The critical level for the trigger efficiency of events from *ep* collisions is therefore level 1, which has been implemented in H1PSI [68].

The Calorimeter Trigger simulation has already been discussed in chapter 4.3.3. Following closely the implementation in the full simulation program H1SIM, the H1PSI read out cells are grouped together to so called 'trigger tower' arrays, which are used for building energy sums for the different angular regions of the detectors (see chapter 5.1 for further discussions).

Track triggers are constructed from the multi wire proportional chambers MWPC and from the drift chambers.

The MWPC in the central and forward tracker are used to determine the z position of the vertex. The event is triggered if the vertex position is lying inside the predicted range of -25 cm $< z <$ 25 cm. The vertex is determined by analysing a histogram, which contains the z positions of all track candidates obtained from combining the information of the inner and outer (inner and forward) MWPC chambers. All possible combinations of hits in the chambers are considered, which results in a flat distribution for incorrect combinations and in a peak at the correct vertex position.

In H1PSI this trigger is simulated by calculating the number of tracks pointing to the vertex. Taken into account are the size of the read out pads of the chambers and inefficiencies. The probability to find a vertex in the event is then parameterized, by using the detailed simulation, in dependence of the number of tracks in the forward and in the central part.

Complementary to the MWPC's, the drift chambers are measuring the $r - \varphi$ coordinates of tracks with very good precision. In the trigger a hard wired logic looks for patterns pointing to the vertex. A minimal number of tracks is then required for a trigger.

In H1PSI, the pattern recognition is simulated by asking for charged particles with more then 450 MeV and a reasonably small distance of closest approach (DCA) to the vertex. This approximation gives a good one to one correspondence on event by event level in comparison to the full simulation.

4.4 Potential and Limitations of Parameterized Simulations

H1PSI is meant as a complement to the full detector monte carlo program H1SIM. It provides a general purpose simulation of all detector components and of their reconstruction, and is at least 300 times faster than the detailed programs[13]. To give an example, 1 million deep inelastic scattering events can be simulated within about 1 day CPU time on an IBM 3090 processor. Thus it is a tool for fast physics analysis projects. Moreover it might be the only reasonable choice if the simulation of really large event samples have to be considered (see below). Generally the aim is to

- describe on average correct the efficiencies of detectors and the gaussian parts of their resolutions
- describe to some degree also the non gaussian parts of the resolution functions by including decays, gamma conversions, electron bremsstrahlung, punch through, leakage, dead materials in the calorimeter, the double track resolution in the tracking chambers, shower overlaps,..

The first item should guarantee the correct systematic behaviour with respect to analysis cuts, etc., while the second gives some handle also on tails of the simulation.

It is however obvious that such a fast simulation cannot describe all detector effects. Which effects are to be included depends entirely on the CPU time available and the importance of the effect with respect to analysis. In practice one has to assure in a specific analysis that all critical ingredients are simulated[14]. This can be deduced from the previous chapters. Some obvious examples for features not included are

---

[13]The speed of the program can even be improved by switching of detector parts, which are not necessary for a specific analysis.

[14]It is of course hoped that this is the case for really important effects.

- effects of the octagonal structure of the calorimeter
- bending by the magnetic field inside the calorimeter stacks.
- correlations between error on energy measurements and the longitudinal shower profiles
- fluctuations of the lateral shower profile
- the reduced sampling of calorimeter cells in longitudinal direction
- correlations of the errors of track parameters between central and forward tracker due to multiple scattering in front of the central tracker
- ...

Most of these effects are small but may still have bad influence if they are overlooked. As an example the electron identification should not be based entirely on lateral shower profiles since these are not fluctuated. In this sense H1PSI should not be used as a 'black box' like, may be, the detailed simulation programs. On the other hand, additional features are easy to add.

Tuning   An essential requirement and advantage of a parameterized simulation is the possibility to tune the program to real data. Finally, the quality of the data description after a detailed tuning will determine the possible applications of, not only, the fast simulation.

Tuning here means that properties of the experiment in the real beam conditions have to be deduced from the data and have to be used as input to the simulation.

In a first step, the basic detector properties have to be determined:

- the efficiencies of chambers
- the geometric acceptance, which might differ from the anticipated one (which is described in H1PSI anyhow) due to dead channels, noise problems, synchrotron radiation background in certain parts of the apparatus
- spatial resolution of hits in track chambers, ...

In order to simplify the tuning, all such parameters of the simulation are stored in the H1PSI data base, and can easily be changed by users. This is true not only for resolutions but also for the definitions of active chamber volumes, etc.

From other experiments, is is well known that also after this first tuning step there are most probably still differences between data and monte carlo events. This is also to be expected for very detailed simulation programs. Reasons herefore are calibration problems, imperfections in the geometry descriptions, uncertainties in the cross sections used for the shower description, undetected inefficiencies, noise and electronic problems in the read out, etc..

In a full detector simulation program, it is extremely difficult to correct for such problems due to the fact that they are very large and complicated, and that many single physics processes together determine, for example, the energy resolution of the calorimeters. Even more difficult than changing the parameters of physics processes might be to modify the geometry description in the calorimeters. This would be a method to, for example, improve on the description of the energy resolution in regions with cracks in the sampling structure[15].

In contrast to this, in a parameterized simulation, the resolutions are inserted from the user, and are not the result of complicated calculations. They can even be adjusted independently in different regions of the detector and are thus easily adapted to the specific experimental situation.

Up to here, only the tuning of parameters for the given parameterizations are discussed. If these turn out to be not adequate for the description of data they can easily be extended or even changed completely.

Presently, the parameterizations chosen are guided by physics principles $(1/\sqrt{E}$ resolution of calorimeters, ...). Higher order corrections to these formulas are of course reasonable, but completely new parameterizations or empirical fits of arbitrary functions to the measured data are questionable. If these turn out to be necessary, it is presumably better to upgrade H1PSI by introducing more details of the geometry, a more precise description of shower developments, etc., in order to describe the effects. The natural limitation of such an attempt is of course the speed of the program. It should not be the aim to create a program similar to GEANT. If CPU time turns out to be a problem, one would have to restrict the use of H1PSI to applications which are not critical with respect to these details.

Applications H1PSI has been used in the past for a large variety of physics studies. Many examples have been published in [49]. Some of the applications are mentioned in the following list.

- Reconstruction of the kinematic variables x, y and Q^2 in deep inelastic scattering (see also chapter 5)

- Determination of the gluon structure function $g(x, Q^2)$ from the reconstruction of J/ψ events [69].

- Determination of α_s from jet ratios in DIS [70].

- Calibration of the liquid argon calorimeter by comparison with information of the tracking detectors [71].

- Background studies for exotic events [72][1] (see also chapter 5 and 6).

- Determination of the efficiency of the luminosity counter [67].

---

[15]From this it is also evident that for the parameterized simulation, tuning to real data and not to data of the detailed monte carlo should be preferred.

  • Influence of gamma conversions inside the tracking detectors

In these analysis H1PSI has been treated as a tool for the development of analysis strategies.

Another application is seen in a fast understanding of detector effects. Because the detector parameters are very easy to change in H1PSI, it is possible to increase or decrease effects of particle properties (decays, interaction probabilities) and of detector effects (efficiencies, resolutions, crack sizes). Their influence on the final physics distributions can thus be estimated. Most important is therefore, that

  • systematic errors of physics results due to detector effects can be estimated very fast by running H1PSI with different detector parameters.

The high speed of the program also allows the determination of other systematic errors, which require extremely large event samples, like

  • dependence on structure function parameterizations
  • dependence on fragmentation models
  • dependence on parameters in the generators and tuning of generators

Also for feasibility studies of possible upgrades of the *H1* detector, the program has been used.

Filter   One of the motivations for a very fast simulation program has been that it could be used as a filter for the huge background event samples expected at *HERA* [57]. Examples for a very unfortunate signal to background ratio are for example low Q^2 events as background to high Q^2 events in DIS, the $c\bar{c}$ background for $b\bar{b}$ events, or the low P_T photoproduction events for the high P_T events, and presumably also tails of standard physics distributions as background for 'exotic' events from physics beyond the standard model.

The idea of the filter is to select with H1PSI only those background events which might enter the region of experimental interest. These 'shifted' events are then supposed to be treated by the detailed simulation program in order to finally determine efficiencies with high accuracy.

The problem of such an approach is, that events with large fluctuations in a specific run of a monte carlo program will generally show a different behaviour in another run (or in a run of another simulation program), due to a different status of the random generator. Thus the background would be largely underestimated. A solution to this suggested in ref. [57] was a complicated mixture of the fast and the slow (detailed) monte carlo, which later turned out to be generally impossible [73].

An alternative approach however can be suggested (see the example in section 5.2). Large shifts of background events origin mainly from:

- fluctuations on the generator level:
  initial state radiation, parton shower and fragmentation effects, ...

- wrong interpretation of the event topology:
  electron from heavy quark decays taken to be the scattered beam electron, ...

- specific event topologies together with detector effects:
  $\pi^-\pi^\circ$ overlaps or gamma conversions leading to electron misidentification, leakage, cracks, ...

The first two items do not depend very much on the description of the detector. Running the fast monte carlo on the whole sample of background events will give a reasonable estimate of such a background. Analysing these events might then allow to find save cuts on the level of the generated 4 vectors in order to select all these events for a later simulation with the detailed monte carlo program. These cuts will of course accept also additional background events which also have to be simulated, but this number is expected to be much smaller then the original sample.

For events considered in the last item of the list above, a fairly good description of the tails of detector effects is required. Such a good description might be difficult to obtain with the approximations of a fast simulation program. The quality is also hard to cross check with the detailed monte carlo, because of the limited statistic obtainable with this program. For this reason it is suggested to use a version of H1PSI, where all 'dangerous' detector effects (assuming they are described at all) are increased by a certain factor. So for this 'bad' detector, the lifetimes of all particles should be decreased in order to allow more decays, the material thicknesses of passive zones should be increased and those of active zones decreased, more particle misidentification is inserted, etc. Such a 'bad' version of the detector is easily created in case of a parameterized simulation. Running it on the whole background statistic will give an upper estimate of events migrating in regions of physics interest. Then, as above, save cuts can be found accepting all potentially 'dangerous' background events. An example for such cuts is given in chapter 5.2.

Recently, an alternative to the method of simulating a complete set of background events has become popular. To be explicit, the example of DIS events is taken, where the cross section is roughly $\sim 1/Q^4$. The region of physics interest is assumed to be at high Q^2, measured in presence of a background from low Q^2 events.

The idea is to generate and simulate events not according to their cross section, but, to give an example, flat in Q^2. Each event then gets a weight, so that the weighted event sample corresponds to the original cross section. The result is that in regions of special interest (high Q^2) but low cross section, more events are simulated, and regions of lower interest are suppressed. In case of such a very steep spectrum, this leads very soon for the low Q^2 events to weights as large as 10^4 and even larger.

A typical problem for the analysis of rapidly falling cross section are migrations from regions of high cross section towards those of low cross section due to measurement errors. Depending on the size of these fluctuations and the shape of the distribution such events may even dominate the measurement at high Q^2. In the scenario of weighted events this might mean, that single events with extremely high weights appear in the distributions at high Q^2, disturbing completely the interpretation.

Even more dangerous is the case, when there are no events with high weights measured at high Q^2. The reason is that this might simply mean that not enough events are produced at low Q^2 in order to determine the background in the region of interest. In this case only an upper limit can be given. At 90% confidence limit the non observation of background events implies that the mean of the background distribution is not larger than 2.3 events. This number has to be scaled by the weights for these events resulting in an upper limit for the background of 2.3×10^4 events! The only way out of this problem is either

- to assume a priori that there is not such background, or

- to simulate such, that no high weights occur, in especially also high event numbers at low Q^2. This can only be done by a fast detector monte carlo.

5 Leptoquark Search

5.1 Trigger

The measurement of structure functions in deep inelastic scattering is clearly a major priority for the *HERA* experiments. The trigger settings are adjusted to this requirement. The similarity of their event characteristics implicate that also for leptoquarks, the triggers for DIS events will be effective.

For both neutral and charged current topologies the main level 1 trigger is based on the calorimeters. The charges deposited in the hadronic and electromagnetic stacks are scaled in a simple way for the different responses of hadrons and electrons of the non compensating calorimeters. As discussed in chapter 4.3.6 and 4.3.3, the results are not the final reconstructed energies due to the missing of weighting, the neglection of certain calorimeter layers, dead material corrections and the very coarse granularity of the trigger towers, etc. The energies are summed up in different angular regions of the detector to allow triggers in a large kinematic range.

For leptoquark events the two most important triggers are based on the total transverse energy flow E_T defined as

$$E_T = \sum_i E_i \, e_{z,i}$$

and, for leptoquark decays into neutrinos, the total transverse missing energy $E_{T,miss}$.

$$E_{T,miss.} = \left| \sum_i E_i \, \vec{e}_{T,i} \right|$$

where E_i is the scaled energy deposited in trigger tower i, $\vec{e}_i = (e_{x,i}, e_{y,i}, e_{z,i})$ is a unit vector pointing from the nominal vertex to this trigger tower and $\vec{e}_{T,i} = (e_{x,i}, e_{y,i})$. Since $E_{T,miss}$ corresponds roughly to transverse momentum, a trigger threshold in $E_{T,miss}$ leads for a given leptoquark mass to a rejection of events only at very high and at very low y[16]. The distributions for E_T and $E_{T,miss}$ are shown in figure 22 for the example of a scalar leptoquark of 100 GeV and 200 GeV respectively. The trigger thresholds[17] chosen for the start of *H1* are

$$E_T > 20 \ \text{GeV} \qquad\qquad E_{T\,miss} > 12 \ \text{GeV}.$$

---

[16]From equations 5, 13 and 29, it follows:

$$y = \frac{1}{2} \pm \frac{\sqrt{M_{LQ}^2 - 4P_T^2}}{2M_{LQ}}. \tag{23}$$

[17]This trigger is combined with a veto counter against background from interactions of the proton beam halo with the material of the beam pipe in front of the detector.
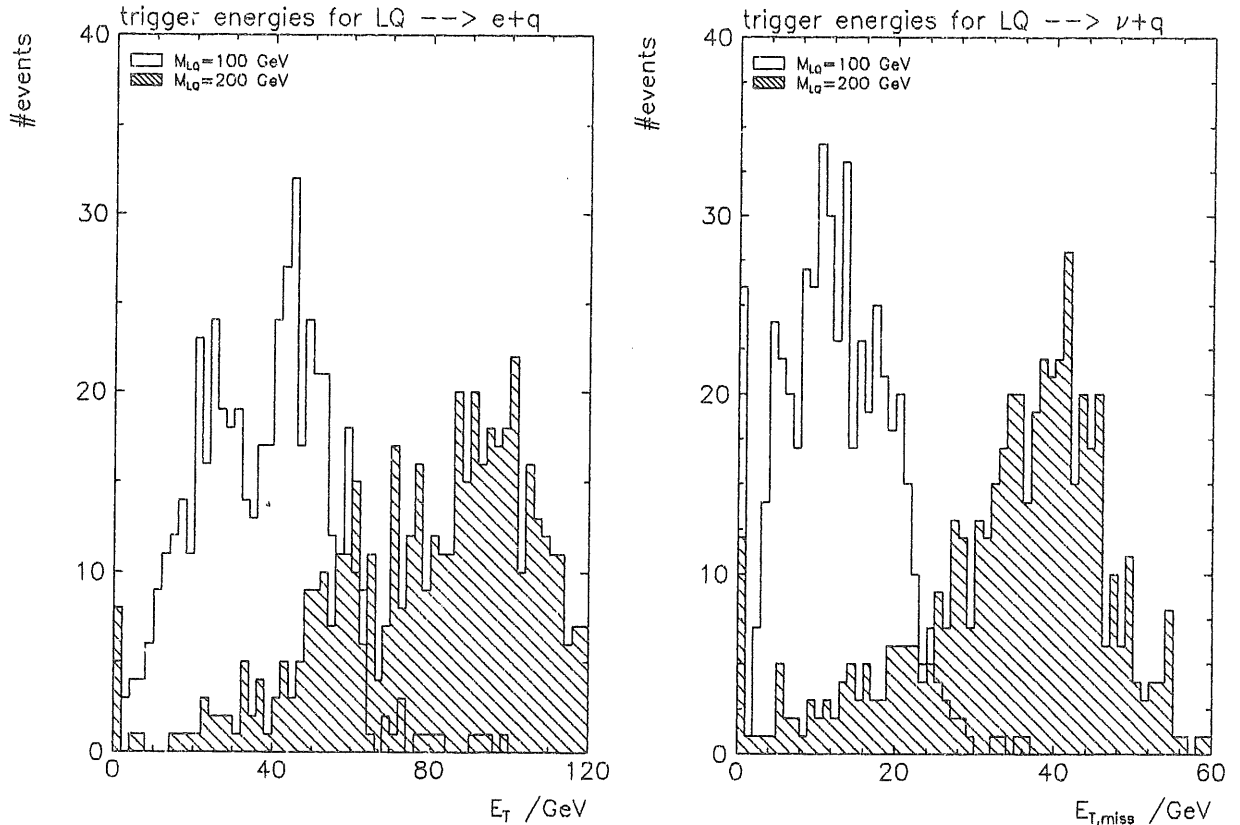
Figure 22: *Trigger energy sum distribution for 500 scalar leptoquarks of 100 GeV and 200 GeV. Left: transverse energy flow for leptoquark decays into electron and quark. Right: missing transverse energy flow for decays into neutrino and quark.*

Obviously these triggers are well suited for leptoquarks with high masses. For low mass leptoquarks decaying into neutrinos, the $E_{T,miss}$ threshold reduces the trigger efficiency severely. In this case however, calorimeter triggers in combination with triggers from the drift chambers improve the situation largely.

The final trigger efficiencies for different masses are shown in figure 23. Based on 500 events for each mass point the efficiency is always above 96%.

5.2 Event Selection

The high event rates expected at *HERA* require a fast reduction of data. In *H1*, this problem is approached by the concept of event classification, which means, that each event is flagged as a possible candidate for specific physics processes. This selection will
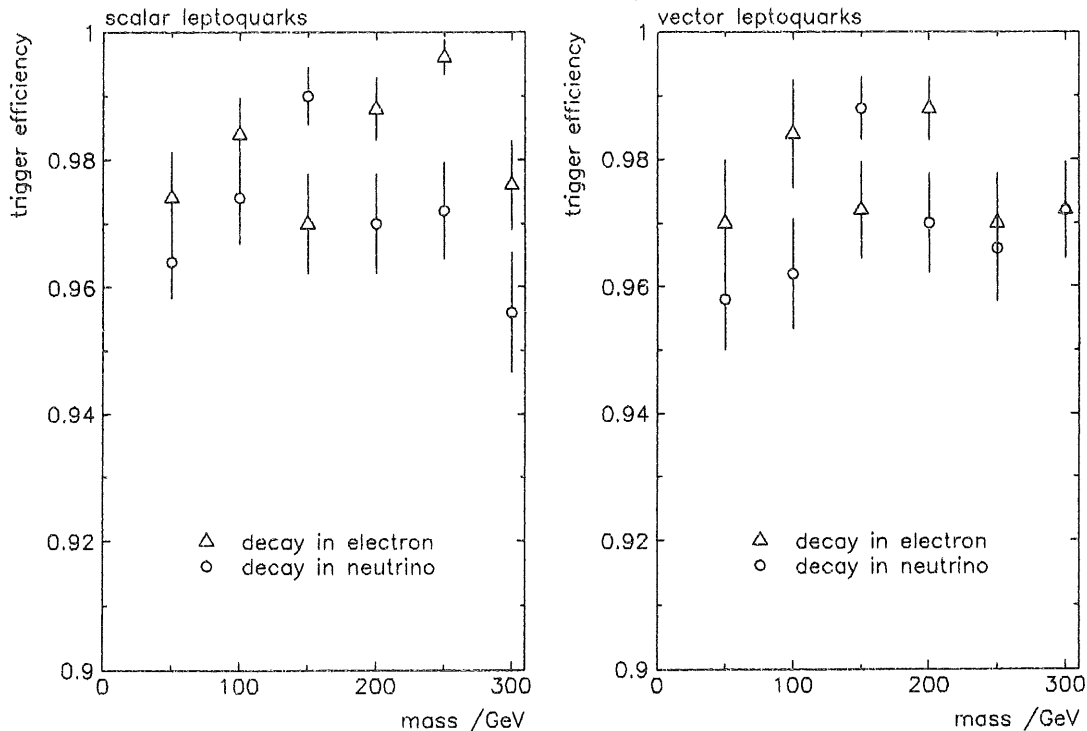
Figure 23: *Trigger efficiency for scalar (left) and vector leptoquarks (right).*

allow fast access to the desired event sample, but it also implies the danger of loosing valuable events.

In principle, this problem is very similar to the one discussed in chapter 4.4, where the fast simulation was used to preselect events for the detailed detector monte carlo. Essentially these selections work like a trigger, since it would be very tedious, if not technically impossible, to go back to the original data samples.

So for each analysis it is necessary to define save cuts, which for sure include all interesting events, but still have some discriminative potential against the large background.

For the analysis of leptoquarks, and implicitly for DIS events at high x and Q^2, these cuts are defined by using a modified, 'bad' description of the detector within the framework of the H1PSI monte carlo (see chapter 4.4). They can be used for both applications, the event classification and the monte carlo preselection. This has the additional advantage that the same systematic behaviour (and may be systematic error) can be expected in the data and in the monte carlo event sample.

A principle in the definition of these cuts should be to use quantities which have a simple physical interpretation in terms of phase space and event topology.

Of special importance is the definition of the scattered electron. This cannot be done with particle identification methods, since these are not available for the preselection, which is working on 4 vectors only. Therefore only topological and kinematic cuts are envisaged.

- The scattered electron should be isolated with respect to other particles in the event. This is nicely seen in figure 24, where the distance with respect to azimuthal angle φ and pseudorapidity η between the electron and other particles in the event is shown. Distances close to $\delta\varphi = \pi$ are dominating, because the jet of the decay quark compensates the transverse momentum of the electron. For other particles but the electron, very short distances are dominating as a consequence of the jet structure of the events. A cut

$$\Delta = \sqrt{(\delta\phi)^2 + (\delta\eta)^2} > 0.3$$

  as the shortest distance to another charged particle was selected as a requirement for the scattered electron.

- Figure 25 shows the correlation between the minimal distance Δ to the next particle and the transverse momentum of the scattered electron and other particles in the same event. Obviously, those particles which are isolated by more than $\Delta = 0.3$ are mainly low energetic spill off's from jets. Therefore the scattered electron is finally defined to be the particle with the highest transverse momentum among those, which are isolated as explained above.

The scattered electron beeing defined in this way, the kinematic variables x, y and Q^2 can be calculated and used for further event classifications. More severe cuts are possible if one introduces in addition kinematic constrains. This question will be addressed in chapter 5.3.3.
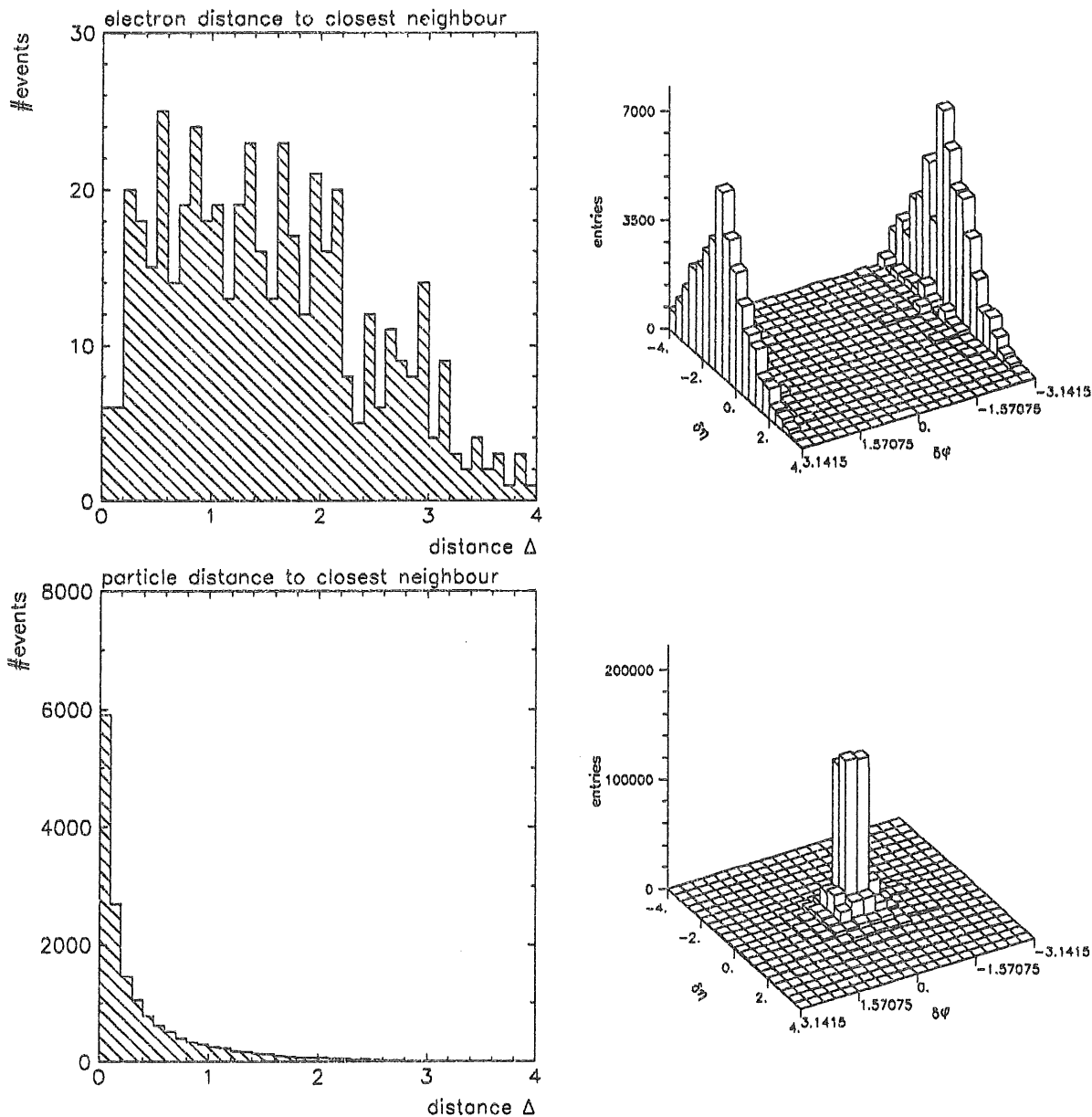
Figure 24: *Isolation of electrons from the decay of a 200 GeV scalar leptoquark.*
Top left: distance $\Delta = \sqrt{(\delta\phi)^2 + (\delta\eta)^2}$ *between the electron from the leptoquark decay and the closest neighbouring particle in the event. Below the same, but instead of the electron for all other particles in the event. Top right: distance between the decay electron and all particles in the event. The position of the electron is* $\delta\phi = \delta\eta = 0$. *Below the same, but instead of the electron for all other particles in the event.*
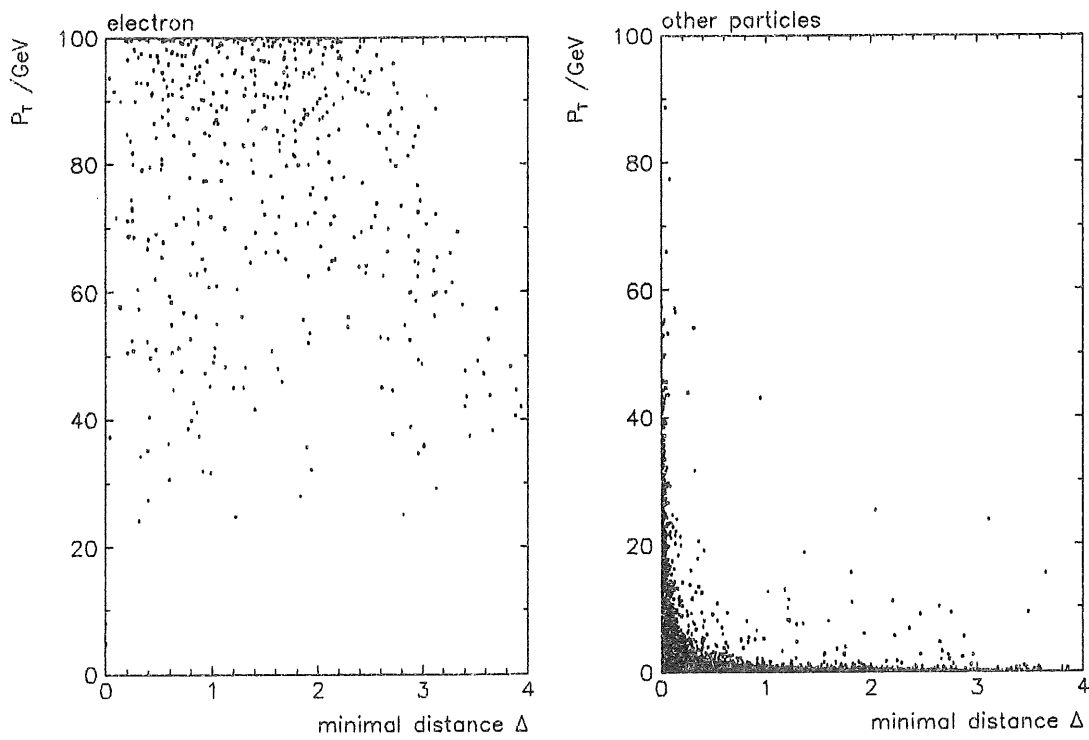
Figure 25: *Isolation and transverse momentum of electrons from the decay of a 200 GeV leptoquark.*
Left: transverse momentum of the electron from the leptoquark decay versus the distance
$\Delta = \sqrt{(\delta\phi)^2 + (\delta\eta)^2}$ *to the closest neighbouring particle in the event. Right: the same, but for all other particles in the event.*

5.3 Reconstruction of Leptoquark Masses

Since the topologies of leptoquark events and of deep inelastic scattering events are indistinguishable and the natural width of leptoquarks is very small, an optimum reconstruction of the leptoquark mass is of greatest importance[18].

There are basically two different approaches to compute the mass. It is possible to use the decay products of the leptoquarks, the electron and the quark. This method has been tried out using a Jade algorithm [75] in order to define the quark jet. The main deficiency of this method is the imperfection of the jet reconstruction giving rather moderate mass resolutions (10– 20 GeV) with long tails to lower and higher masses.

A much more efficient approach is to use the relation $M^2 = xs$ (see chapter 3.3). However, in contrast to the previous method, this introduces effects of radiative corrections which depend on the reconstruction scheme used for x. The most important part of this is initial state bremsstrahlung from the electron shown in figure 26. Since
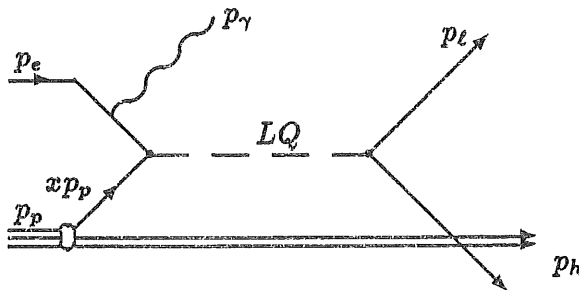
Figure 26: *Feynman diagram for s– channel production of leptoquarks with initial state bremsstrahlung.*

the radiated photon is dominantly collinear to the incident particle the main effect is a reduction of the energy of the incoming electron, E_e, to

$$E_e \rightarrow E_e - E_\gamma$$

Only 10 – 20 % of the radiated photons are measured by the luminosity counters. So in the calculations it is generally not possible to insert the reduced electron energy (see however chapter 5.3.3). Thus, the reconstructed kinematic variables x_{rec}, y_{rec} and Q^2_{rec} are shifted systematically with respect to the ones at the hard scattering vertex, $\hat{x}, \hat{y}$ and $\hat{Q}^2$. These shifts turn out to depend on the various reconstruction methods and will be calculated in the next chapters.

It must be stressed that the effect of an undetected photon from initial state bremsstrahlung is somewhat different for deep inelastic events compared to leptoquarks. Assuming a very narrow resonance of the exotic particle, the energy loss of the incoming

---

[18]The approximations used in the following kinematic relations have been explained in chapter 3.2.

electron must be compensated by a higher quark momentum $\hat{x} P_p$ in order to produce the same invariant mass. Therefore $\hat{x}$ is given by

$$M_{LQ}^2 = (\hat{x} p_p + p_e - p_\gamma)^2 = 4\,\hat{x}\,E_p\,(E_e - E_\gamma) \tag{24}$$

A radiated photon of 1 GeV already produces a shift on $\hat{x}$ of about 3%. This is an important contribution if compared with the experimental resolution for x itself (see below). Compared to the reconstructed mass

$$M_{rec}^2 = x_{rec} s \tag{25}$$

this gives

$$\frac{M_{rec}^2}{M_{LQ}^2} = \frac{x_{rec}}{\hat{x}}\, f \tag{26}$$

where

$$f = \frac{E_e}{E_e - E_\gamma} \tag{27}$$

For this reason the effect of initial state radiation will be discussed for the different reconstruction schemes.

Charged current events are usually reconstructed with the Jacquet– Blondel method [77], which was designed to reduce the dependence on energy losses in the beam hole in the direction of the proton, specifically by the spectator jet of the proton remnant. Only the total hadronic energy flow is used here which guarantees independence of the jet structure of the final hadronic state. In neutral current events the kinematic can also be calculated from the electron measurement. The behaviour of these two basic reconstruction schemes with respect to measurement errors and initial state radiation are summarized in the following chapters.

For neutral current events the kinematic is over– determined and many reconstruction algorithms are possible using combinations of the electron and the hadron measurements. All these combinations vary in their systematic behaviour in the presence of bremsstrahlung and, since the electron and the hadrons are measured with different precision, the resolutions for x, y, and Q^2 depend strongly on the kinematic region considered. In chapter 5.3.3 a new ansatz for the calculation of kinematic variables will be introduced. The aim of this procedure is to provide optimal reconstructed variables independent of the kinematic region and independent of initial state radiation.

In the following calculations the measurement errors (denoted by δ) are assumed to be gaussian and their correlations (if existing) are ignored. In most cases this is a very good approximation since angles are usually taken from track chamber measurements and energies from calorimeter data. Errors on beam energies can be neglected.

5.3.1 Observing the Scattered Electron

Using only the energy E_ℓ and angle ϑ_ℓ of the scattered lepton the basic equations are:

$$y_\ell = 1 - \frac{E_\ell}{2E_e}(1 - \cos\vartheta_\ell) \tag{28}$$

$$Q_\ell^2 = 2\,E_e\,E_\ell\,(1 + \cos\vartheta_\ell) \tag{29}$$

$$= \frac{P_{T\ell}^2}{1 - y_\ell} \tag{30}$$

$$x_\ell = \frac{E_e\,E_\ell\,(1 + \cos\vartheta_\ell)}{E_p\,(2\,E_e - E_\ell\,(1 - \cos\vartheta_\ell))} \tag{31}$$

Without measurement errors and initial state radiation these equations correspond to the definitions given in chapter 3.2. For given x, y, Q^2 the electron variables are recovered as

$$E_\ell = \frac{Q^2}{4\,E_e} + E_e\,(1 - y) \tag{32}$$

$$\cos\vartheta_\ell = \frac{Q^2}{2\,E_e\,E_\ell} - 1 \tag{33}$$

Assuming that the measurement errors of E_ℓ, ϑ_ℓ are uncorrelated, the resulting errors for the kinematic variables are:

$$\frac{\delta y_\ell}{y_\ell} = -\frac{1 - y_\ell}{y_\ell}\left(\frac{\delta E_\ell}{E_\ell} \oplus \cot\frac{\vartheta_\ell}{2}\,\delta\vartheta_\ell\right) \tag{34}$$

$$\frac{\delta Q_\ell^2}{Q_\ell^2} = \frac{\delta E_\ell}{E_\ell} \ominus \tan\frac{\vartheta_\ell}{2}\,\delta\vartheta_\ell \tag{35}$$

$$\frac{\delta x_\ell}{x_\ell} = \frac{\delta Q_\ell^2}{Q_\ell^2} \ominus \frac{\delta y_\ell}{y_\ell} \tag{36}$$

$$= \frac{1}{y_\ell}\frac{\delta E_\ell}{E_\ell} \oplus \left(\frac{1 - y_\ell}{y_\ell}\cot\frac{\vartheta_\ell}{2} - \tan\frac{\vartheta_\ell}{2}\right)\delta\vartheta_\ell \tag{37}$$

The $\oplus$ and $\ominus$ symbols mean that the errors should be added quadratically. However, they distinguish an increase or decrease of the derived variable in dependence of the measurement error. In case of substantial initial state radiation the reconstructed variables x_ℓ, y_ℓ, Q_ℓ^2, are related to the ones at the hard interaction $\hat{x}$, $\hat{y}$, $\hat{Q}^2$ like

$$\frac{1 - y_\ell}{1 - \hat{y}} = \frac{1}{f} \tag{38}$$

$$\frac{Q_\ell^2}{\hat{Q}^2} = f \tag{39}$$

$$\frac{x_\ell}{\hat{x}} = \frac{\hat{y}}{y_\ell} = \frac{1 - (1 - y_\ell)\,f}{y_\ell} \tag{40}$$

where f is defined in equation 27. For the case of leptoquarks with the additional constraint of equation 26, the reconstructed mass is

$$\frac{M_\ell^2}{M_{LQ}^2} = f\,\frac{1 - (1 - y_\ell)\,f}{y_\ell}. \tag{41}$$

5.3.2 Observing the Hadronic Energy Flow

Using only hadronic measurements imposes the problem that a large fraction of the hadronic energy is carried by the proton remnant and therefore vanishes in the beam hole at very low angles. Requesting momentum balance in the transverse plane between the scattered lepton and the hadronic vector, $P_{Tl} = P_{Th}$, Jacquet and Blondel [77] tried to minimize beam hole effects in the proton direction via:

$$y_h = \frac{E_h - P_{zh}}{2\,E_e} \tag{42}$$

$$Q_h^2 = \frac{P_{Th}^2}{1 - y_h} \tag{43}$$

$$x_h = \frac{Q_h^2}{y_h\,s} \tag{44}$$

where the total hadronic 4 vector is defined as $p_h = \sum p_{hadrons}$. Since the measurement errors for this method depend on the event topology and fragmentation effects, a precise analytical error prediction can not be made. On the parton level however the proton remnant does not carry transverse momentum or mass and the energy and angle of the scattered quark (E_q, ϑ_q) can be written as

$$y = \frac{E_q}{2\,E_e}\,(1 - \cos\vartheta_q) \tag{45}$$

$$Q^2 = \frac{(E_q\,\sin\vartheta_q)^2}{1 - y} \tag{46}$$

or

$$E_q = \frac{(1 - y)\,Q^2 + 4y^2\,E_e^2}{4\,y\,E_e} \tag{47}$$

$$\cos\vartheta_q = \frac{Q^2(1 - y) - 4\,E_e^2\,y^2}{Q^2(1 - y) + 4\,E_e^2\,y^2} \tag{48}$$

One may assume in addition that after parton shower and fragmentation into hadrons the jet corresponding to the scattered quark has a negligible mass. The errors of the jet energy and angular measurement δE_q, $\delta\vartheta_q$ propagate like

$$\frac{\delta y_h}{y_h} \approx \frac{\delta E_q}{E_q} \oplus \cot\frac{\vartheta_q}{2}\,\delta\vartheta_q \tag{49}$$

$$\frac{\delta Q_h^2}{Q_h^2} \approx \frac{2 - y}{1 - y}\,\frac{\delta E_q}{E_q} \oplus \left(2\cot\vartheta_q + \frac{y}{1 - y}\cot\frac{\vartheta_q}{2}\right)\delta\vartheta_q \tag{50}$$

$$\frac{\delta x_h}{x_h} \approx \frac{1}{1 - y}\,\frac{\delta E_q}{E_q} \oplus \left(2\cot\vartheta_q + \frac{2y - 1}{1 - y}\cot\frac{\vartheta_q}{2}\right)\delta\vartheta_q \tag{51}$$

Initial state radiation modifies similar to the previous case the measured quantities to

$$\frac{y_h}{\hat{y}} = \frac{1}{f} \tag{52}$$

$$\frac{Q_h^2}{\hat{Q}^2} = \frac{1 - \hat{y}}{1 - y_h} \tag{53}$$

$$\frac{x_h}{\hat{x}} = \frac{1 - \hat{y}}{1 - y_h} = \frac{1 - y_h f}{1 - y_h} \tag{54}$$

Again, for leptoquarks this leads to

$$\frac{M_h^2}{M_{LQ}^2} = f \frac{1 - y_h f}{y_h}. \tag{55}$$

One way to combine electron and hadron measurements is to use only the angles of the scattered electron and quark. In the parton picture equation 2 gives for the transverse– respectively energy– and longitudinal components

$$E_\ell \sin\vartheta_\ell = E_q \sin\vartheta_q \tag{56}$$

$$x(E_p - P_{zp}) + E_e - P_{ze} = E_\ell - P_{z\ell} + E_q - P_{zq} \tag{57}$$

and

$$2 E_e = E_\ell(1 - \cos\vartheta_\ell) + E_q(1 - \cos\vartheta_q) \tag{58}$$

and from this

$$E_\ell = 2 E_e \frac{\sin\vartheta_q}{\sin\vartheta_q (1 - \cos\vartheta_\ell) + \sin\vartheta_\ell (1 - \cos\vartheta_q)} \tag{59}$$

$$E_q = 2 E_e \frac{\sin\vartheta_\ell}{\sin\vartheta_q (1 - \cos\vartheta_\ell) + \sin\vartheta_\ell (1 - \cos\vartheta_q)} \tag{60}$$

Thus the lepton and quark energy are expressed in terms of the angles and can be inserted in equation 28,29,31.

$$y_{2\vartheta} = 1 - \frac{\sin\vartheta_q (1 - \cos\vartheta_\ell)}{\sin\vartheta_q (1 - \cos\vartheta_\ell) + \sin\vartheta_\ell (1 - \cos\vartheta_q)} \tag{61}$$

$$Q_{2\vartheta}^2 = 4 E_e^2 \frac{\sin\vartheta_q (1 + \cos\vartheta_\ell)}{\sin\vartheta_q (1 - \cos\vartheta_\ell) + \sin\vartheta_\ell (1 - \cos\vartheta_q)} \tag{62}$$

$$x_{2\vartheta} = \frac{E_e}{E_p} \frac{\sin\vartheta_q (1 + \cos\vartheta_\ell)}{\sin\vartheta_\ell (1 - \cos\vartheta_q)} \tag{63}$$

The problem of defining the quark angle is overcome by using the complete hadronic state in form of the Jacquet– Blondel formulas equations 42,43. Inserting them in equation 48:

$$\cos\vartheta_{qh} = \frac{P_{Th}^2 - (E_h - P_{zh})^2}{P_{Th}^2 + (E_h - P_{zh})^2} \tag{64}$$

Assuming as above that the current– jet is massless and that the spectator– jet carries no transverse momentum the angle ϑ_{qh} is largely independent of hadronic energy measurement errors. This is indeed expected because these approximations correspond to a

single particle seen in the detector in the direction of the scattered quark. Measurement errors influence the kinematic variables like:

$$\frac{\delta y_{2\vartheta}}{y_{2\vartheta}} = (1-y)\left(\frac{-\delta\vartheta_\ell}{\sin\vartheta_\ell} \oplus \frac{\delta\vartheta_{qh}}{\sin\vartheta_{qh}}\right) \tag{65}$$

$$\frac{\delta Q^2_{2\vartheta}}{Q^2_{2\vartheta}} = \frac{y-2}{\sin\vartheta_\ell}\delta\vartheta_\ell \oplus \frac{-y}{\sin\vartheta_{qh}}\delta\vartheta_{qh} \tag{66}$$

$$\frac{\delta x_{2\vartheta}}{x_{2\vartheta}} = \frac{-\delta\vartheta_\ell}{\sin\vartheta_\ell} \oplus \frac{-\delta\vartheta_{qh}}{\sin\vartheta_{qh}} \tag{67}$$

It is interesting to note that initial state radiation from the electron does not disturb the measurement of ϑ_{qh}, since the primary electron energy drops out of equation 64. This also means that $y_{2\vartheta}$ is radiation independent while

$$\frac{Q^2_{2\vartheta}}{\hat{Q}^2} = f^2 \tag{68}$$

$$\frac{x_{2\vartheta}}{\hat{x}} = f \tag{69}$$

and for leptoquarks

$$\frac{M^2_{2\vartheta}}{M^2_{LQ}} = f^2 \tag{70}$$

If ϑ_{qh} is calculated as described above it is possible to make the double angle method completely independent of radiation. The unknown electron energy at the hard interaction, $E_e - E_\gamma$, has to be replaced by the measured energy of the scattered lepton E_ℓ. Equations 58 and 56 give

$$E_e = E_\ell\,\frac{\sin\vartheta_q\,(1-\cos\vartheta_\ell) + \sin\vartheta_\ell\,(1-\cos\vartheta_q)}{2\,\sin\vartheta_q}. \tag{71}$$

This can be inserted in equation 62,63:

$$Q^2_{2\vartheta\,E_\ell} = E_\ell^2\,\frac{\{\sin\vartheta_q\,(1-\cos\vartheta_\ell) + \sin\vartheta_\ell\,(1-\cos\vartheta_q)\}\,(1+\cos\vartheta_\ell)}{\sin\vartheta_q} \tag{72}$$

$$x_{2\vartheta\,E_\ell} = \frac{E_\ell}{2\,E_p}\,\frac{\sin\vartheta_q\,(1+\cos\vartheta_\ell) + \sin\vartheta_\ell\,(1+\cos\vartheta_q)}{\sin\vartheta_q} \tag{73}$$

As mentioned above the equation for $y_{2\vartheta}$ does not need modifications. The errors of $E_\ell, \vartheta_\ell, \vartheta_{qh}$ propagate like

$$\frac{\delta Q^2_{2\vartheta\,E_\ell}}{Q^2_{2\vartheta\,E_\ell}} = 2\frac{\delta E_\ell}{E_\ell} \oplus \left\{2\cot\vartheta_\ell - \frac{y_{2\vartheta}}{\sin\vartheta_\ell}\right\}\delta\vartheta_\ell \oplus \frac{y_{2\vartheta}}{\sin\vartheta_{qh}}\delta\vartheta_{qh} \tag{74}$$

$$\frac{\delta x_{2\vartheta\,E_\ell}}{x_{2\vartheta\,E_\ell}} = \frac{\delta E_\ell}{E_\ell} \oplus \left\{\cot\vartheta_\ell - \frac{y_{2\vartheta}}{\sin\vartheta_\ell}\right\}\delta\vartheta_\ell \ominus \frac{1-y_{2\vartheta}}{\sin\vartheta_{qh}}\delta\vartheta_{qh} \tag{75}$$

5.3.3 The Constrained Kinematic Fit

The kinematic of neutral current events is over-determined and can be evaluated from the measurement of electron variables or hadron variables or combinations of both. Which of the many possibilities should be used depends on the precision obtained finally for x, y and Q^2. These are very different for the various kinematic regions and therefore one would have to choose alternative algorithms depending on the phase space area considered. This however is dangerous because changing from one method to another at some boundary might introduce threshold effects in the resulting distributions.

Here an attempt is made to avoid these difficulties by using a method that takes into account the measurement errors from the electron and hadrons in the calculation of the event kinematic. For over-determined systems, the standard method promising optimum resolutions is a **constrained kinematic fit**. This is independent of the kinematic region considered because in any case all event information, including measurement errors, are taken into account. In the following a new ansatz for such a fit will be introduced. Besides solving the difficulties mentioned above, it will be shown that this ansatz provides a powerful tool to reject badly measured events and to distinguish different physical processes.

The basic idea is *not* to fit directly the kinematic variables x, y, Q^2, as it has been suggested by other authors. This would mean to loose the azimuthal (φ) information of the event (only $|P_T|$ would be constrained). Instead, the measured 4-vectors p_ℓ, p_h of the scattered lepton and hadrons are fitted directly with respect to 4-vector conservation. Let p_γ be the 4-vector of a possible photon from initial state radiation, which is (in most cases) not observed in the detector:

$$p_e + p_p = p_\gamma + p_\ell + p_h$$

The radiated γ is assumed to be collinear to the electron beam giving for the transverse momentum components $P_{x,\ell}, P_{y,\ell}$ of the lepton and $P_{x,h}, P_{y,h}$ of the hadrons

$$P_{x,\ell} + P_{x,h} = 0 \qquad (76)$$

$$P_{y,\ell} + P_{y,h} = 0 \qquad (77)$$

Since a large fraction of hadronic energy is lost in the beamhole only the combination '$E - P_z$' is considered (like in the Jacquet-Blondel formulae). Neglecting proton and electron masses and using $E_e = -P_{z_e}$ and $E_\gamma = -P_{z_\gamma}$ yields

$$2E_e = 2E_\gamma + (E_\ell - P_{z_\ell}) + (E_h - P_{z_h}) \qquad (78)$$

So there are three constraining equations and one unmeasured variable E_γ.

The results of the fit are an improved reconstruction of the electron and hadron momentum vectors and the radiated photon, which was not seen in the detector, will also be reconstructed.
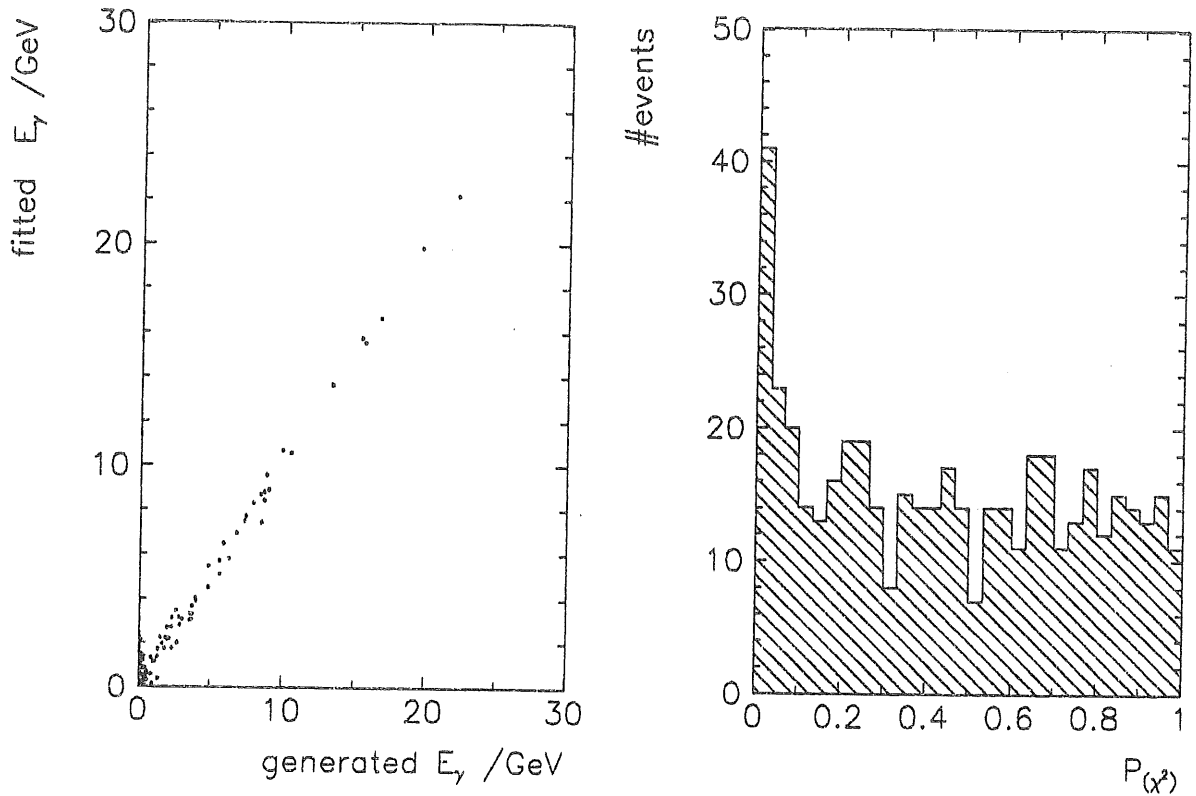
Figure 27: *Photon energy and χ^2 probability distribution as obtained from the constrained fit.*

Figure 27 shows, as a result of the constrained fit, the reconstructed energy of the (unmeasured) radiative photon. The fitted γ energy is well correlated to the generated value even at energies as low as ≈ 3 GeV. The corresponding probability function $P(\chi^2)$ distribution is flat as expected with exception of the first bin. This was found to be due to events with either high leakage outside the detector or with secondary interactions of particles in the tracking chambers. Sometimes the fit is also disturbed if those hadrons which are lost in the beamhole have very large transverse momentum. Since all these cases have not been treated in the covariance matrix, some increase at low $P(\chi^2)$ is expected and obviously, a cut at $P(\chi^2) \leq 0.05$ is a powerful tool to suppress badly measured events. This cut is also very well suited to distinguish neutral current from charged current events as $P(\chi^2)$ is sensitive to missing transverse momentum.

The kinematic variables can now be calculated by replacing the energy of the incoming electron with help of the fitted γ- energy $E_e^{fit} = E_e - E_\gamma^{fit}$. As initial state radiation is now taken into account explicitly and the fit enforces consistency in the P_T and '$E - P_z$' measurements between the scattered lepton and the hadrons, all differences of the various reconstruction schemes mentioned above have disappeared. Any formula

can be used then, *with the fitted lepton or hadron vectors*, to determine $\hat{x}$, where $\hat{x}P_p$ is the momentum of the parton entering the hard interaction. The mass of the leptoquark is then determined by

$$M_{LQ}^2 = \hat{x}s\frac{E_e^{fit}}{E_e}$$

Figure 28 shows a comparison of the various reconstruction methods with the fitting procedure suggested here for a scalar leptoquark of $M_{LQ} = 100$ GeV. As discussed in
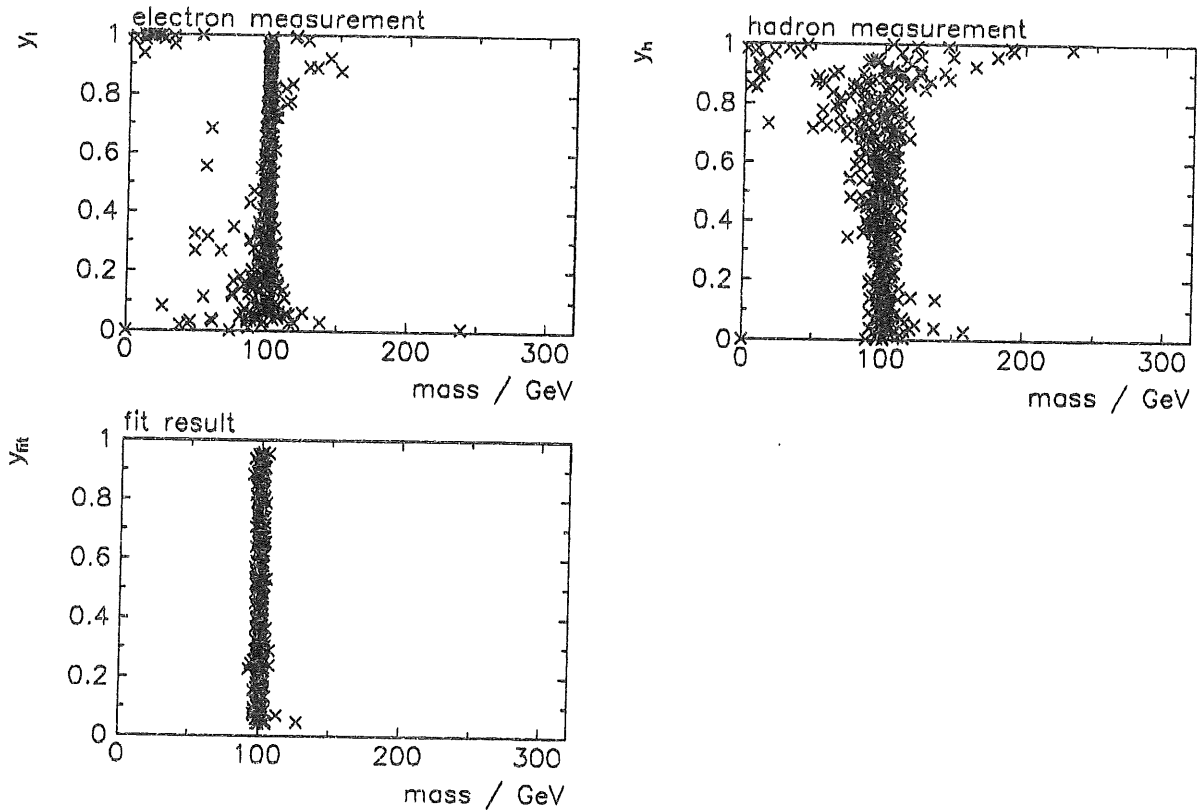
Figure 28: *Mass reconstruction in dependence of y using only the electron, only the hadrons or the constrained fit.*

chapter 3.3, the natural width is expected to be very small, and the cross section is flat in y.

For the calculation of the leptoquark mass in the first two figures, the equations $M_{LQ}^2 = x_\ell s$ and $M_{LQ}^2 = x_h s$ are used (see eq. 25). Therefore, the experimental signature shown here can readily be explained with the kinematic relations derived in the previous sections.

The upper left plot shows the reconstruction with help of the measurement of the scattered electron only. The experimental mass resolution is rather good at high y and

decreases substantially at lower y. This behaviour is expected from the $1/y$ dependence of the error on the x measurement as derived in equation 36. Tails in the distribution are also visible towards high masses at high y and towards low masses at low y. These events are due to high energetic initial state radiation from the electron. The shift in the observed mass corresponds to equation 41.

Compared to this, the hadronic measurement shows a rather complementary behaviour. The resolution for x is very limited at high y, which is a consequence of the $1/(1-y)$ dependence on the hadronic energy measurement (see equation 51). Also the effect of initial state radiation shows up at high masses and low y respectively low masses and high y. This is indeed anticipated from equation 55.

In both schemes, the few events at large y and low masses originate from a misidentification of the scattered electron.

The result of the fitting procedure is clearly a big improvement of the mass resolution. Also the tails due to initial state radiation are recovered. The experimental width (≈ 2 GeV) has become almost independent of y which very much simplifies a further separation from deep inelastic scattering background.

In summary the fit has the following advantages:

* All event information from the electron and the hadrons are taken into account. They are properly weighted with their experimental errors.

* Optimum use is made of the fact that the kinematic is over– determined. This includes the azimuthal structure of the event.

* Consistency between the electron and hadron measurement is enforced. There is no longer an ambiguity of how to reconstruct the kinematic variables.

* Events with bremsstrahlung of the incoming electron are tagged. The fitted γ– energy can be used to reconstruct the kinematic variables at the hard interaction independent of initial state radiation.

* The method is independent of fragmentation effects since only the total energy flow is used. No approximations are made on jet masses.

* Beamhole effects are suppressed by using only '$E_h - P_{zh}$'. This is similar to the Jacquet– Blondel method.

* The χ^2 of the fit gives a handle to separate neutral current from charged current events.

* Badly measured events can be rejected by a cut in χ^2.

* Another application of the constrained fit is the possibility to distinguish leptoquarks and deep inelastic scattering from photoproduction events of light and heavy quarks. This will be considered in chapter 6.1.

It is noted again, that this method of applying a constrained fit is valid for every type of event which is balanced in transverse momentum (does not contain a neutrino). This is the only necessary requirement. The results are always improved event parameters which can be used further on. In case of the analysis presented here, they have been used to control radiative corrections and to improve the measurement of the leptoquark mass and of x. In DIS analysis, the results might well be used in the same sense, but may be also for the reconstruction of x and Q^2, ignoring effects of initial sate radiation. Also in photoproduction processes, the fit can be used to determine the energy of the primary electron, and thereby of the initial photon.

An additional field of application is the calibration of the detector. Requiring momentum balance in the transverse plane might allow to check or even constrain calibration constants of the calorimeter. This however needs further studies.

However, the result of the fit will get uncertain, if the total transverse momentum of the event gets close to the losses of transverse momentum due to particles, which disappear undetected in the beampipe. In these kinematic regions, the fit might even disturb the measurements and has to be avoided.

5.3.4 Kinematic Influence of QCD Effects

Being colour triplets and octets, leptoquarks and leptogluons are strongly interacting particles. This leads to the question, whether parton shower and fragmentation effects may destroy the nice experimental signature of a state with a width in the order of 1–2 GeV.

Unfortunately, a complete higher order matrix element calculation for QCD effects is not available for ep scattering[19]. In alternative, the COMPOS generator uses the Lund Jetset parton shower monte carlo. However the parton shower is not applied to the leptoquark directly, but only in the final state to the quark from the decay and to the 'diquark' remnant of the proton. In the fragmentation, both together are considered to be the colour singlet in the string fragmentation. This is only a, may be crude, approximation, as the following discussion will show.

Since for a numerical study a more elaborate event simulation would be necessary, only qualitative arguments can be given. Especially, the kinematic influence on the reconstruction of the leptoquark mass will be considered for those effects which are not taken into account explicitly in the simulation.

There are two basic items which influence the measurement of the mass:

- If due to some effect the 'velocity' (expressed in terms of $'E_{LQ} - P_{zLQ}'$) of the leptoquark is changed, then this will be seen as a difference in the y (and therefore also x) measurements from the electron, y_ℓ, and the hadrons, y_h.

$$E_{LQ} - P_{zLQ} = 2E_e(1 - y_\ell + y_h).$$

---

[19]See however chapter 3.3 and [15]. For $p\bar{p}$ collisions large corrections to cross sections have been found [37].
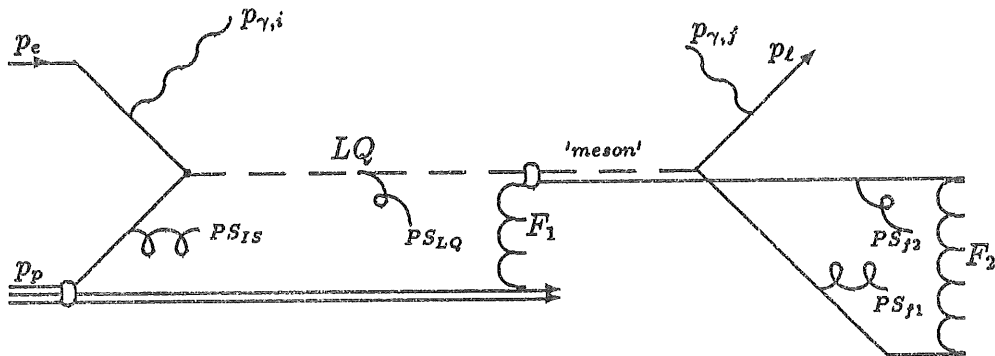
Figure 29: *Parton shower and fragmentation in leptoquark events. See the text for explanations.*

One example for this is given in the discussion of QED radiation in chapter 5.3.3. Whatever the physical reason, the constrained fit will interpret any such occurrence as an initial state photon and therefore compensate automatically for it! In the further discussion, this case will therefore be just ignored.

• On the other hand the leptoquark might get transverse momentum, which means that the decay products will not longer balance each other in P_T. Since the total event is still balanced the fitting procedure cannot identify this case. The azimuthal angle of the decay is not correlated to the direction of $P_{T\,LQ}$ so the result is a random fluctuation for P_T of both electron and hadrons and therefore also for Q^2 and x.

A schematic illustration of the following discussion is given in figure 29. The kinematic effects arise mainly from parton showering and from fragmentation, but for completeness also bremsstrahlung is shown.

• Initial state bremsstrahlung from the electron labeled '$p_{\gamma,i}$' has been extensively discussed before and can be compensated for.

• Final state bremsstrahlung ($p_{\gamma,f}$) is generally less important since the photon is most often collinear with the final state electron and is thus measured with the electron in the same calorimeter cluster.

• Through initial state parton showering (PS_{IS}) the quark from the proton might get some transverse momentum before fusing with the electron.

• After the electron– quark fusion the leptoquark will radiate gluons (PS_{LQ}) and thereby get some transverse momentum. Since it is very heavy, radiation should however be very much suppressed in comparison to initial state parton showering from light quarks.

- The width of leptoquarks and leptogluons accessible at *HERA* ranges from ≈ 0.01 MeV to 100 MeV. To give an example, a leptoquark with $M_{LQ} = 100$ GeV and $\lambda = 0.01$ has a velocity of $\beta = 0.47$ and a lifetime of more than 10^{-21} seconds. After this time the leptoquark and the proton remnant are more than 100 fm apart. However confinement becomes important already at ≈ 1 fm. So one has to assume that the leptoquark itself participates in fragmentation before it decays (F_1). (As mentioned above, the available event generator does not consider these effects for the leptoquark and applies parton shower and hadronization only to the leptoquark decay products.) Therefore, at larger distances, colour forces become strong and strings to the proton will influence the leptoquark. Finally the leptoquark will be bound into some colour– singlet 'meson' or 'baryon'– like system (compare also [15],[34]). For the kinematic this means, that some additional transverse momentum is added. The situation is analogous to the fragmentation of heavy quarks which are also stable enough to create mesons. Ignoring that the leptoquark is not a fermion, one might argue that the fragmentation function of the leptoquark should behave similar to those of heavy quarks, which are known to be very hard. This would mean that the leptoquark is almost unaffected by the fragmentation process.

  The final 'meson' however will have some mass, different, but close to the leptoquark mass. It is well plausible, similar to the spectroscopy of heavy quark mesons, to assume the existence of several mass states within the observable mass range. This would lead to a completely new experimental signature.

- Then the decay of the leptoquark inside this colour– singlet will happen. This is a state with light quarks only and substantial parton shower (PS_{f1}, PS_{f2}) effects are to be expected. The quark partner of the leptoquark in the meson will behave like a spectator jet, while the quark from the leptoquark decay gets high transverse momentum.

How to estimate the size of all these effects is not clear, and requires a detailed monte carlo study with a modified event generator. Even if one ignores the effects denoted by PS_{LQ}, $F1$ and the creation of a meson, there are remaining uncertainties.

Through final state parton showering the quark originating from the decay of the leptoquark acquires some mass m_{ps}. Two different models for the treatment of this mass in the decay have been suggested. The authors of the COMPOS program, which is used in this analysis, considered the decay and the parton shower to be independent and consecutive steps. In the PYTHIA generator however, the decay of the leptoquark is treated like a decay into a heavy quark of mass m_{PS}, which changes substantially the decay kinematic. This difference in the treatment of final states yields for PYTHIA to a shift to lower reconstructed masses

$$M^2_{recons.} = M^2_{LQ} \frac{1 - \mu}{1 + \mu \frac{1-y}{y}} \tag{79}$$

with $\mu = \frac{m_{ps}^2}{M_{LQ}^2}$. In principle m_{ps} can be measured but this would again introduce some dependence on jet algorithms. The effects of the PYTHIA– treatment for the final state parton shower is shown in figure 30. The sharp peak in the mass distribution has got tails towards lower reconstructed masses as expected from equation 79. In comparison to this the effect of initial state parton showering and initial state bremsstrahlung seems to be moderate. The calculated shift in the mass is independent of the reconstruction scheme.

Following the scheme used in PYTHIA the number of events inside the expected signal area (and the limits) would be reduced by about 10%.

The size of all other effects are not known and their determination would need improved event generators.
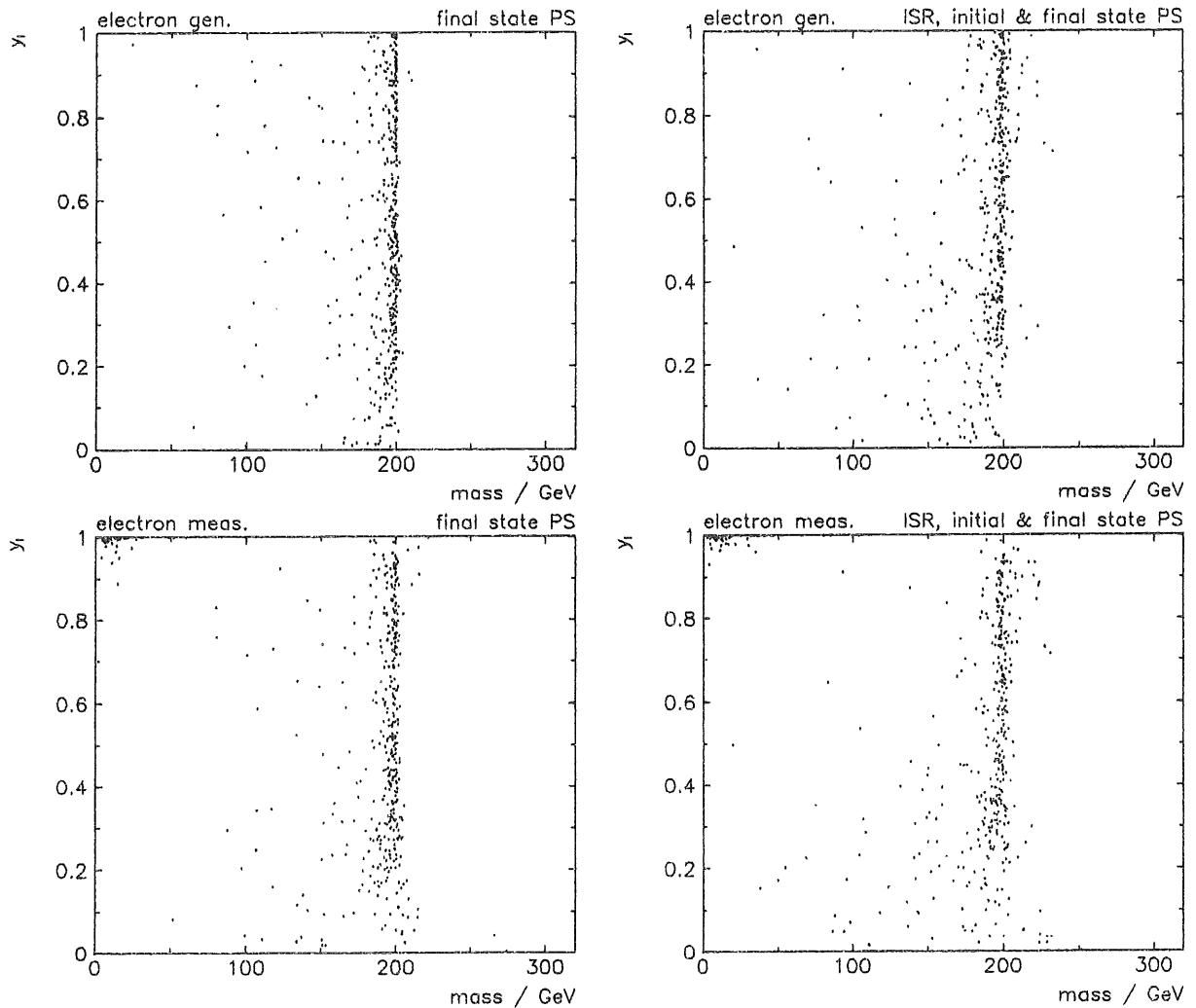
Figure 30: *Effect of the PYTHIA model of parton shower masses on the reconstruction of the leptoquark mass using the generated electron (upper figures) or the reconstructed electron (lower figures). The left figures show the effect of final state parton showers, the right ones the combination of initial and final state parton shower and initial state radiation (ISR).*

6   Results

6.1   Background from Photoproduction

Looking for rare processes requires a very good knowledge of any background at the level of a few events. The extremely high cross sections for the photoproduction of light and heavy quarks imply that in spite of different topology these might contribute to the background for leptoquarks. Possible reasons are large accidental fluctuations on the generator level or imperfections in the detector performance. Therefore a systematic survey of the non deep inelastic background was performed using the PYTHIA 5.6 generator [46] for direct and resolved photon processes including $c\bar{c}$ and $b\bar{b}$ production.

In most of these reactions, the scattered electron is not visible but disappears in the beamhole. However, another real or misidentified electron with high transverse momentum might then be assumed to be the primary scattered electron. One example for this are electrons originating from the decay of heavy quarks. Also prompt photons may contribute to the background if they produce an asymmetric electron pair in the beampipe. Such photons are typically balanced in transverse momentum by a jet and therefore show the topology of a deep inelastic event. In addition, misidentified electrons, as an example from $\pi - \gamma$ overlaps, might be produced by any physical process. For these reasons all direct and resolved photoproduction processes have been analyzed with special emphasis on potentially dangerous channels. Table 6 gives an overview of the considered number of events and the corresponding statistical significance. All together 0.2 million events have been simulated for the *H1* detector.

final state		# events	luminosity
$c, \bar{c}$		100000	0.25 pb^{-1}
$b, \bar{b}$		6000	30 pb^{-1}
jet– γ,	$\hat{P}_T > 3$ GeV	9000	17 pb^{-1}
jet– jet,	$\hat{P}_T > 3$ GeV	83000	0.07 pb^{-1}
	$\hat{P}_T > 10$ GeV	5000	0.28 pb^{-1}
	$\hat{P}_T > 20$ GeV	9000	12 pb^{-1}

Table 6: *Simulated photoproduction events and the corresponding integrated luminosities. $\hat{P}_T$ is the minimum transverse momentum of the partons in the hard scattering process.*

To suppress the photoproduction background four basic cuts have been applied.

- For the electron, a simple fiducial cut with respect to the most problematic (φ) cracks in the calorimeter is applied in order to avoid too large measurement uncertainties.

- Only those electron candidates are accepted which are isolated in a pseudorapidity–φ cone of $\sqrt{(\delta\eta)^2 + (\delta\varphi)^2} \leq 0.3$. This reduces both the background from decays of heavy quarks and from accidental $\pi - \gamma$ overlaps, since in most cases a jet is expected to be relatively close by.

- In semileptonic $b(c)$–decays the electron is accompanied by a neutrino and therefore often also by missing transverse momentum. In this case, the same $P(\chi^2)$ cut as mentioned above turns out to be very efficient because the constrains in the fit require P_T balanced events.

In addition, also the constrained fit suggested in chapter 5.3.3 can be applied to distinguish leptoquark and deep inelastic scattering processes from photoproduction events with light and heavy quarks. The principle is to use the sensitivity of equation 78 for undetected energy losses in the the backward direction (-z). In case of photoproduction events, this energy is most often due to the scattered electron. This distinguishes them from DIS events and allows an additional consistency check on the event interpretation.

Equation 78 shows that the fitted photon energy E_γ^{fit} does not depend upon which of the particles is considered to be the scattered electron. The equation is symmetric under exchanges of leptons and hadrons. If however the *real* scattered electron was not observed but lost in the beamhole, then E_γ^{fit} is essentially equal to the energy of just this scattered electron E_ℓ. Figure 31 illustrates the experimental result of E_γ^{fit} for the photoproduction processes of table 6 after having applied the cuts mentioned before. The events at high $E_\ell = E_\gamma^{fit}$ origin mainly from events with a low transverse momentum $\hat{P}_T$ at the hard interaction vertex and vice versa.

- A cut at $E_\gamma^{fit} \leq 10$ GeV obviously suppresses a large fraction of the non– DIS background. The loss in efficiency for the leptoquark signal is negligible since the photon spectrum from initial state radiation is decreasing rapidly with increasing photon energy.

Equation 78 may also be written

$$E_\gamma^{fit} = E_e \left(y_\ell^{fit} - y_h^{fit} \right)$$

where y_ℓ^{fit}, y_h^{fit} are computed from the fitted electron candidate and hadron vectors. So figure 31 just shows the difference in the y measurements from the electron and the hadrons illustrating thereby the inconsistency of the interpretation as a deep inelastic scattering or leptoquark event.

However, it must be stated that the remaining background is not really under control since the huge number of simulated events still corresponds to a rather small integrated luminosity and does not allow firm statements concerning tails of the distributions. On the other hand, it is natural to assume that the high P_T leptoquark events can only be mixed up with 'relatively high' $\hat{P}_T$ photoproduction events. For these the simulated number of events is sufficiently large and the result shown in figure 31 indicates that the remaining background is well below the unavoidable deep inelastic scattering background. The photoproduction background has therefore been neglected for the calculations of limits.
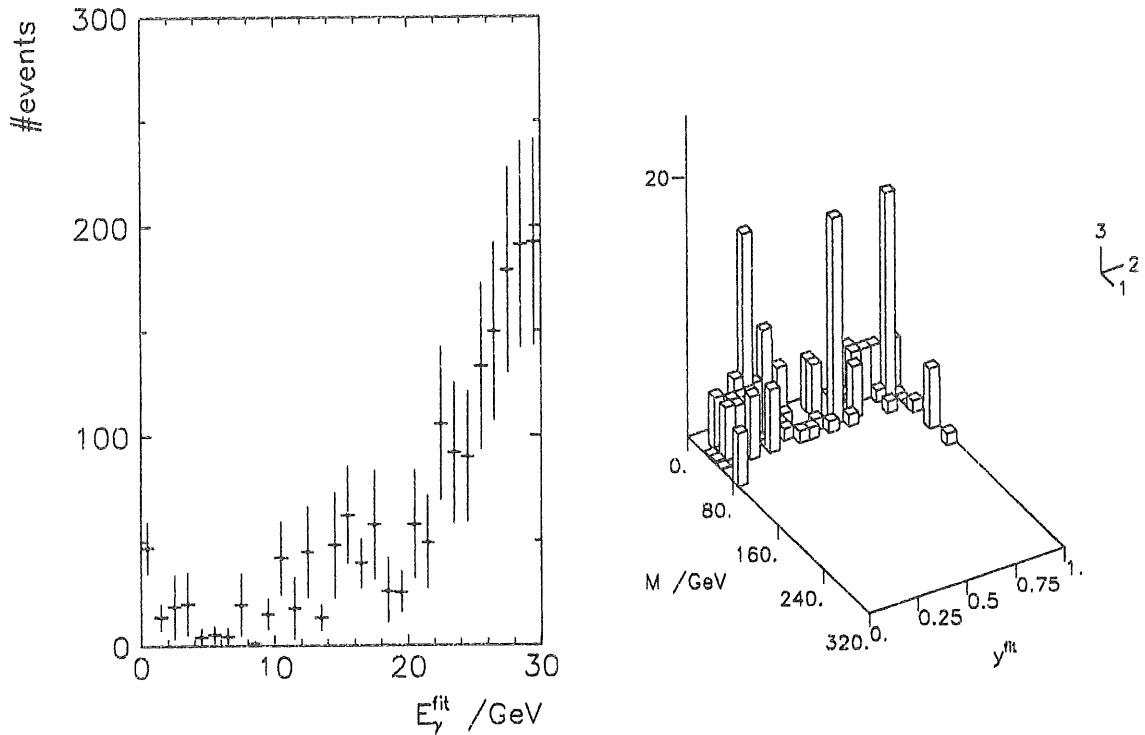
Figure 31: *Fitted γ spectrum for photoproduction events of light and heavy quarks together with the remaining background distribution in the mass–y plane after a cut of $E_\gamma^{fit} < 10$ GeV. Both figures are normalized to correspond to an integrated luminosity of $1pb^{-1}$.*

6.2 Background from Deep Inelastic Scattering

Neutral and charged current events are characterized by just two kinematic variables if the effect of initial state bremsstrahlung is corrected for. Since the mass resolution and y are fairly uncorrelated (figure 28) these variables are chosen to separate leptoquark events from the deep inelastic scattering events. This is a complete description of the events, and no additional variables should be used. They would just insert redundancy in the cuts or cause sensitivity to the hadronic final state. With respect to the uncertainties discussed in chapter 5.3.4, this has to be avoided.

The DIS events simulated correspond to an integrated luminosity of 150 and 250 pb^{-1} respectively for $Q^2 > 300$ GeV^2. Figure 32 shows the DIS background in the invariant mass– y plane obtained after the fit. Overlayed are random events from a scalar leptoquark illustrating the different y– dependence of signal and background.

The separation is performed with independent upper and lower cuts for M_{LQ} and y. In an optimization procedure these four cuts are varied until best limits are obtained. Because of the varying y–shapes of background and signal, this has been carried out separately for neutral and charged current events of scalar and vector leptoquarks (and
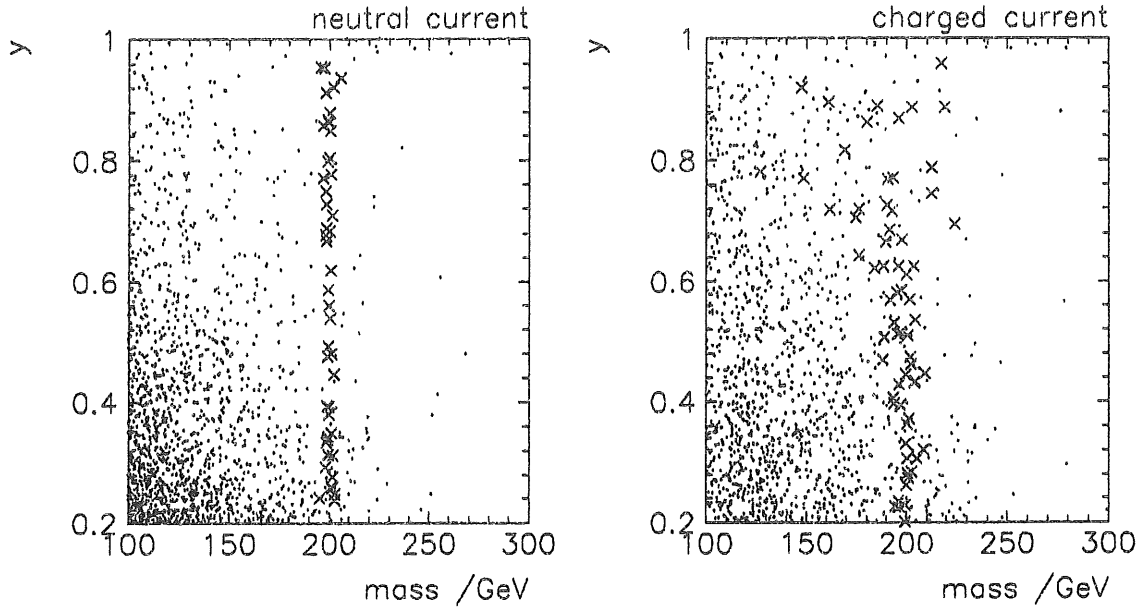
Figure 32: *Background from DIS events for $\int L\,dt = 100\,pb^{-1}$. Overlayed are events from a scalar leptoquark of $M_{LQ} = 200$ GeV.*
left: neutral current events, right: charged current events.

for leptogluons). Only events at very high and very low y are excluded ($0.05 < y < 0.95$) since in these regions radiative corrections are expected to become important for the DIS cross section. Figure 33 shows the optimized cuts in y. The much better mass resolution, obtained by the fit in comparison to other methods, allows to extend the measurement to much lower y. As result of the optimization procedure, leptoquarks with high masses can be separated from background in almost the whole y range. At lower masses the DIS background becomes more and more significant. For scalar leptoquarks decaying into an electron, the lower y cut has to be raised to ≈ 0.3 for $M_{LQ} = 200$ GeV and to ≈ 0.6 for $M_{LQ} = 100$ GeV. For vector particles the cross section drops at high y making the low y region even more important. This also holds for decays into neutrinos because of the decreasing mass resolution obtained at high y with the hadrons alone (right part of figure 32).

6.3 Limits for Leptoquarks

Model independent exclusion limits (based on Poisson statistics) for cross sections ×
branching ratio (BR) of any narrow resonance in the electron– parton system are pre-
sented in figure 34. Here, narrow means that the natural width of the resonance has to
be somewhat less than the experimental mass resolution ($\Gamma < 2$ GeV). Generally the
limits for neutral current topologies are better because the mass resolution is improved
at high y and the background distribution is falling steeper with increasing y. Due to
the different y shapes, a smaller cross section is detectable for scalar leptoquarks than
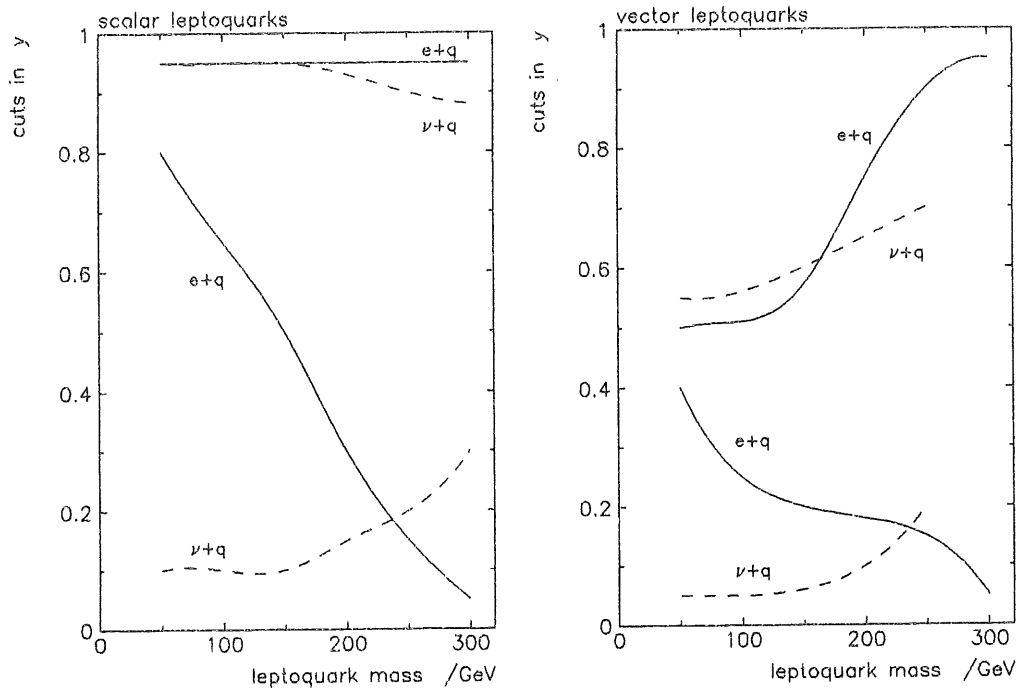
Figure 33: *Optimized lower and upper cuts in y for scalar and vector leptoquarks with decays in electron and neutrino for $\int L\,dt = 100\,pb^{-1}$.*

for vector particles. It is also noted that an increase of the integrated luminosity from 10 to 100 pb^{-1} is improving the final limits only by a factor 3. The statistical limit of three events (95% confidence level) is reached for neutral current topologies at very high masses, indicating that the background vanishes.

Now it is straightforward to obtain limits in terms of masses and coupling constants for any specific model if the branching ratios into electron or neutrino are known. Considered are *all possible* leptoquark couplings given in the framework of baryon and lepton number conserving, dimensionless, $SU(3)_c \times SU(2)_L \times U(1)_Y$ invariant couplings discussed in chapter 2.6 and in [27]. Only decays to leptons and quarks of the first generation are analyzed. Here the branching ratios are well defined and limits in the mass versus coupling constant plane are obtained (figure 35 and 36). The couplings correspond to the crossections given in table 8. Naturally the limits are much better for leptoquarks with couplings to quarks than to anti–quarks. However, it would be the opposite situation if a positron beam becomes available at *HERA*.

Limits for a possible discovery of leptoquarks at *HERA* are shown in figure 37 and 38. As before the limits have been obtained by an optimization of the cuts in the mass–y plane. The requirement for a discovery has been

- a 5 standard deviation effect above background
- at least 10 events.

The leptoquark discovery limits are at most a factor 2 worse compared to the exclusion limits.
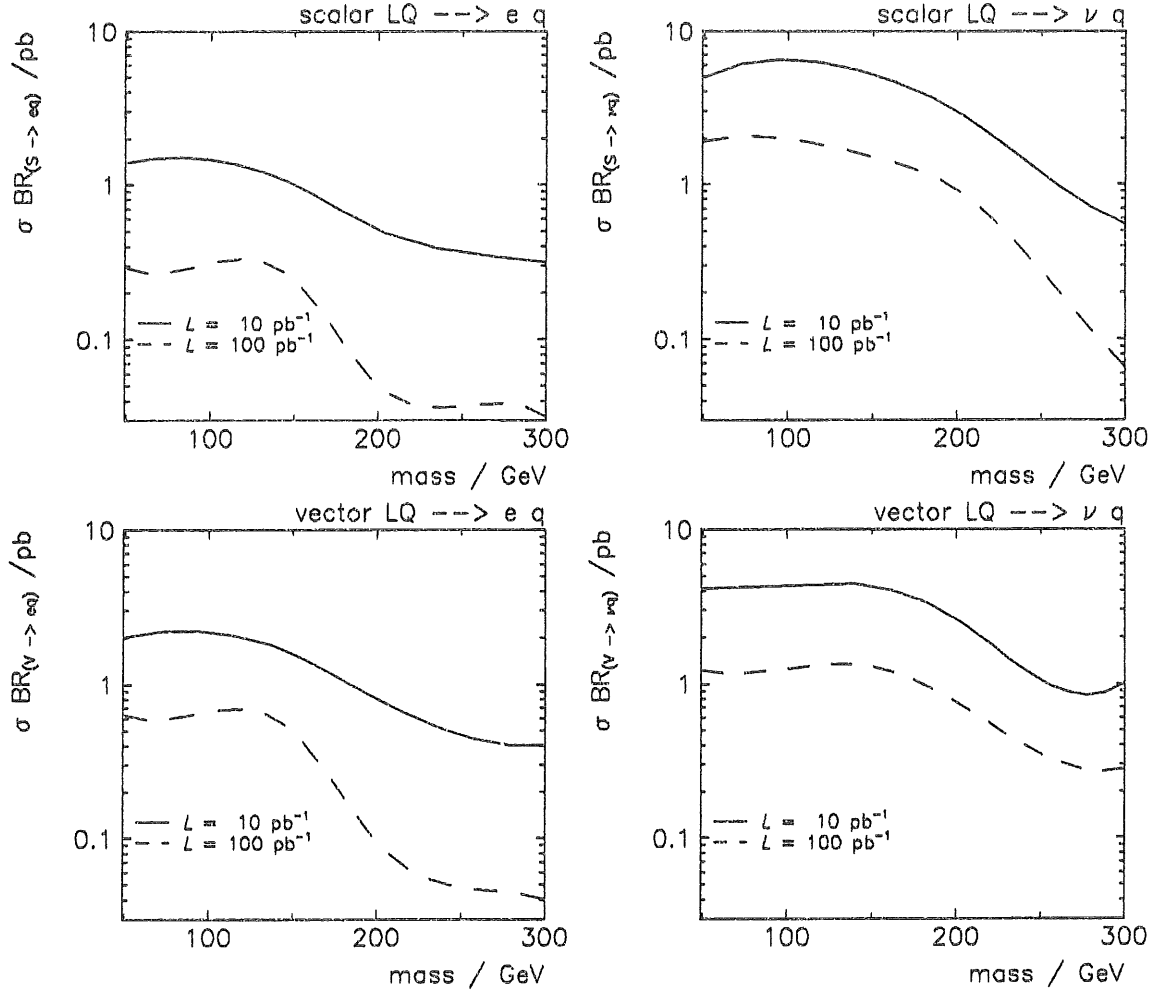
Figure 34: *95% confidence level exclusion limits for cross section × branching ratio of any narrow resonance in the lepton parton system.*

From this general description, also limits for more specific models can be obtained. As an example, the recent suggestion [5] to 'save' $SU(5)$ from disagreement with experimental data can be tested at *HERA*. In this model leptoquarks of the type $\tilde{S}_{1/2}$ are introduced. The corresponding limits in figures 35, 36, 37, 38 are directly valid for this model. For the connection to other models it is refered to chapter 2.6.

As discussed above, the most restrictive bounds from other experiments are $M_{LQ} > 72$ GeV and $M_{S_0,S_1,V_0,V_1} \geq 1.7$ TeV × λ_L as shown in figure 1.

Obviously *HERA* has a great potential to improve these bounds or even establish the existence of such exotic particles, for masses up to almost the kinematic limit and for Yukawa couplings at least one order of magnitude below the region observable up to now. The Yukawa couplings envisaged are already much weaker than for instance the electromagnetic gauge interaction. As an example for a scalar leptoquark decaying with equal probability into electron and neutrino, couplings of $\lambda^2/4\pi = 4 \cdot 10^{-4} \cdot \alpha_{em}$ at
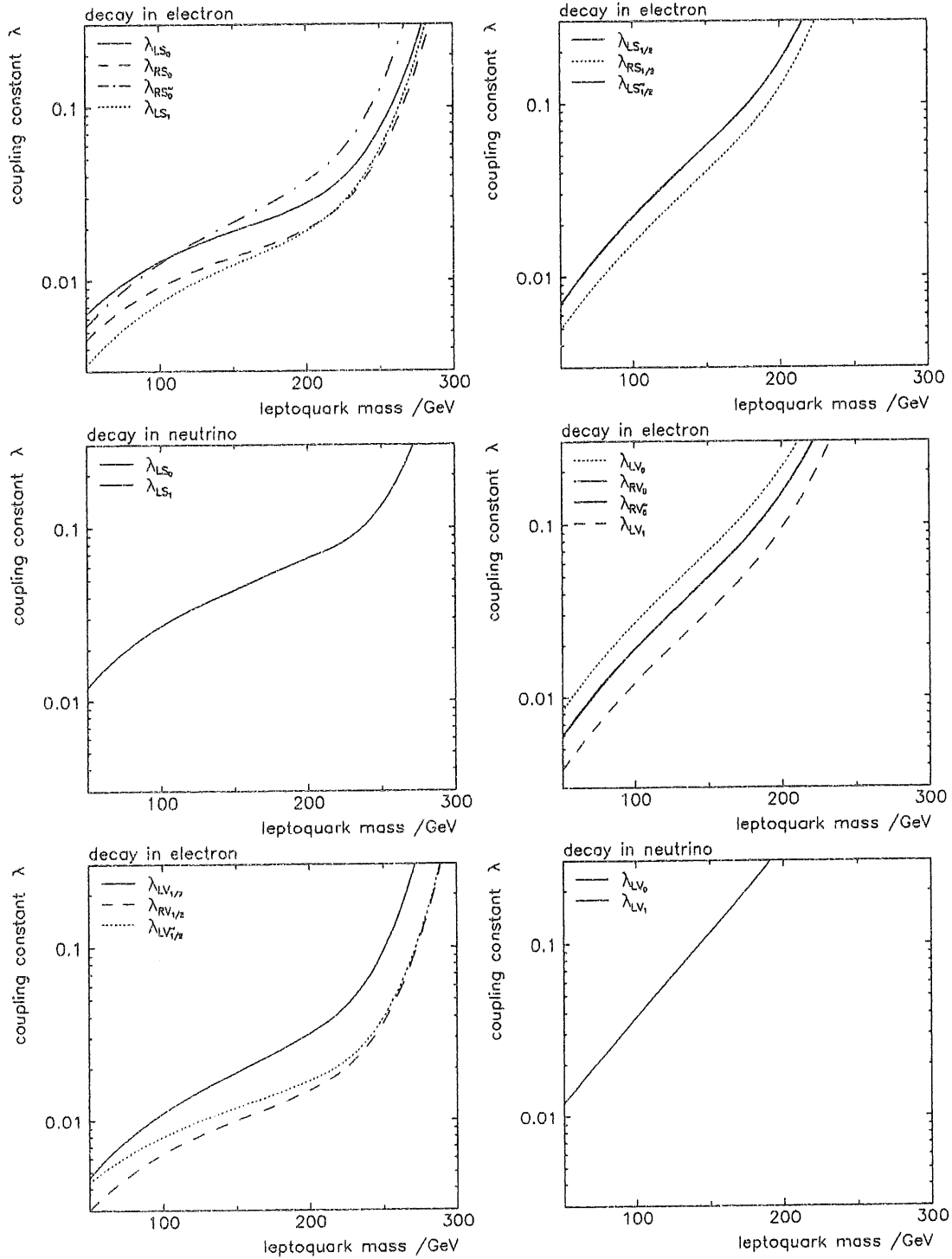
Figure 35: *Exclusion limits for all coupling constants and masses of leptoquarks at 95%
confidence level for ∫ L dt = 10 pb⁻¹. The left figures show couplings of electrons to
quarks, the right to anti- quarks. The structure functions used are from ref. [28].*
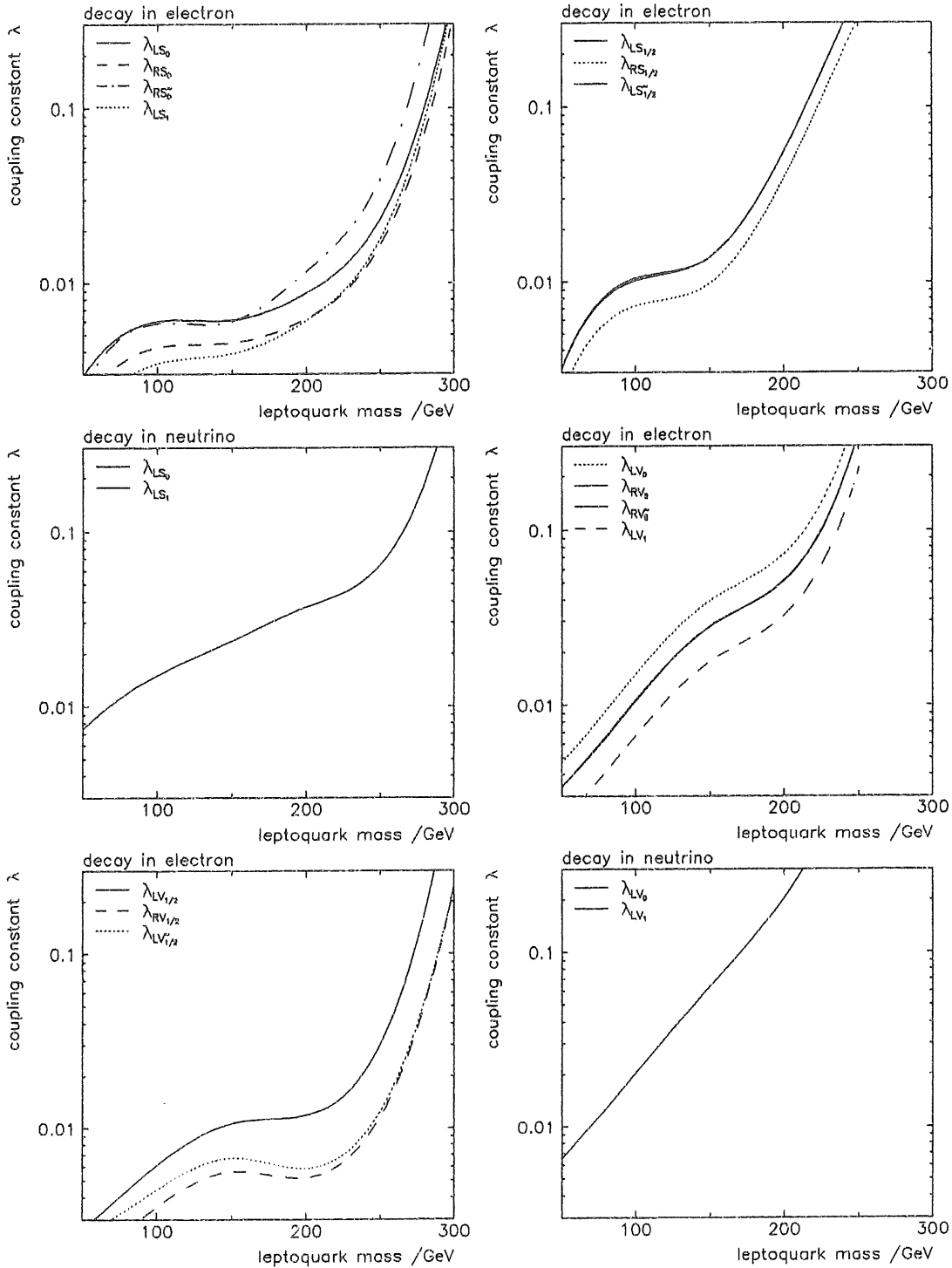
Figure 36: *Exclusion limits for all coupling constants and masses of leptoquarks at 95% confidence level for $\int L\,dt = 100\,pb^{-1}$. The left figures show couplings of electrons to quarks, the right to anti– quarks. The structure functions used are from ref. [28].*
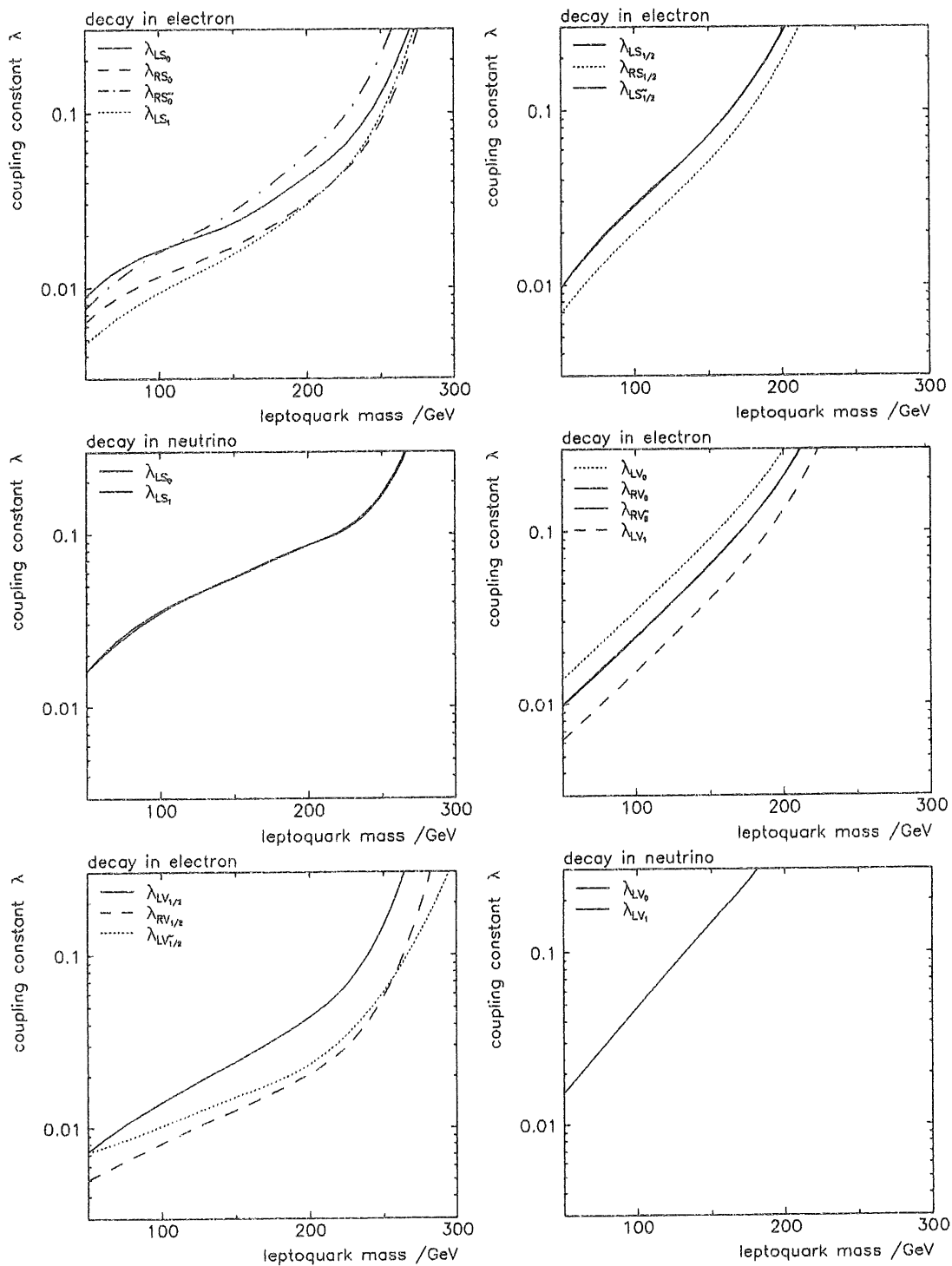
Figure 37: *Discovery potential for all coupling constants and masses of leptoquarks for* $\int L\, dt \,=\, 10\, pb^{-1}$. *The left figures show couplings of electrons to quarks, the right to anti- quarks. The structure functions used are from ref. [28].*
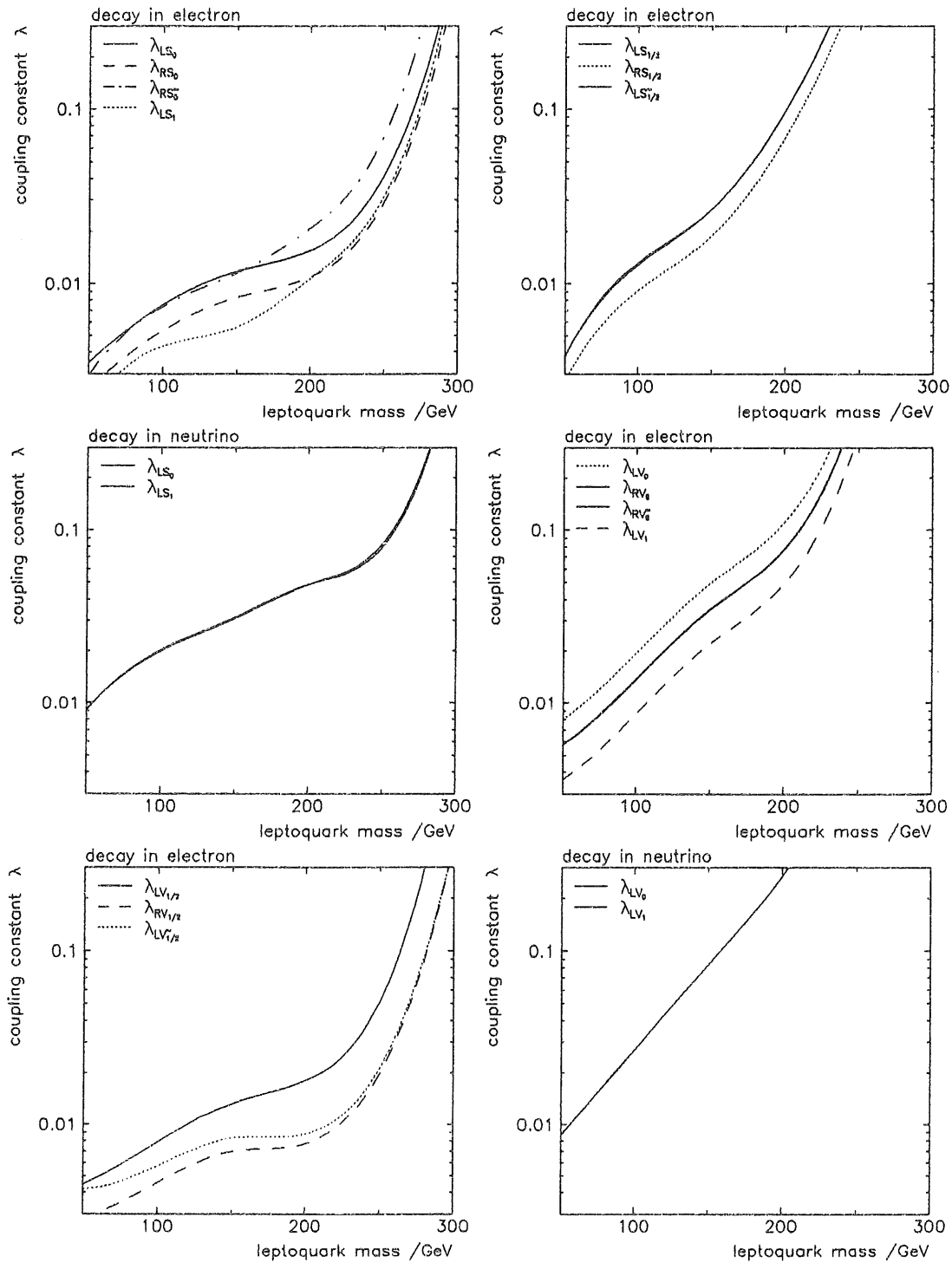
Figure 38: *Discovery potential for all coupling constants and masses of leptoquarks for* $\int L\,dt = 100\,pb^{-1}$. *The left figures show couplings of electrons to quarks, the right to anti- quarks. The structure functions used are from ref. [28].*

$M_{LQ} = 100$ GeV $(\lambda^2/4\pi = 4 \cdot 10^{-3} \cdot \alpha_{em}$ at $M_{LQ} = 250$ GeV) might be excluded.

6.4 Limits for Leptogluons

The topology of events with leptogluons is very similar to those with leptoquarks. The decay in a gluon instead of a quark only alters the hadronic final state. The constrained fit as well as the other reconstruction methods are independent of fragmentation effects. They only use the overall energy flow, which is not affected. Due to this, all results of chapter 5 are also valid for leptogluons. Also the relation to the background from photoproduction and DIS is equivalent. So all analysis steps are perfectly the same, and the results only differ due to the spin of the leptogluon and the absolute size of the cross section.

The remarkable sensitivity of *HERA* for the scale Λ is shown in figure 39. With an integrated luminosity of 100 pb^{-1}, the high production cross section will allow to explore values between $\Lambda = 80$ TeV for low masses and $\Lambda = 1$ TeV close to the kinematic limit.
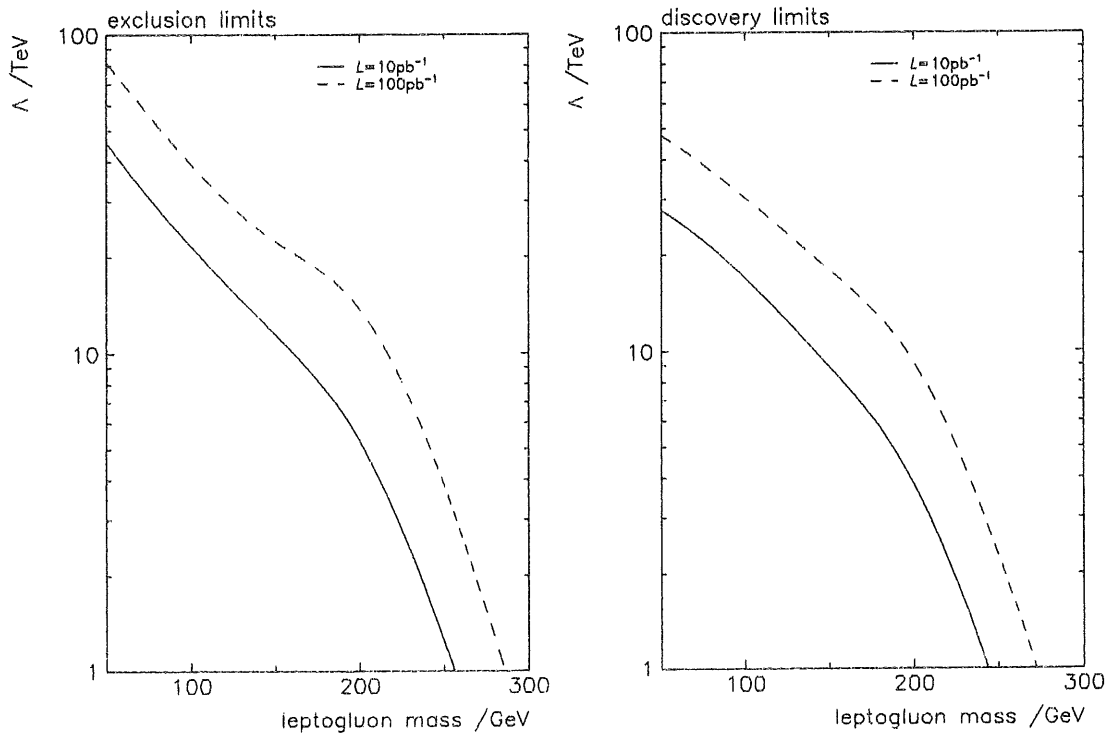
Figure 39: *Exclusion limits (left) and discovery potential (right) for the scale Λ from leptogluon production. The structure function used is from ref. [28].*

6.5 Measurement of Quantum Numbers

Assuming a signal in the invariant mass spectrum, several methods are available in order to measure the quantum numbers of the observed resonance and the properties of the couplings. In the framework described in table 7 these are:

- The spin and therefore the shape of the differential cross section $\frac{d\sigma}{dy}$ allows a separation of scalar leptoquarks from leptogluons and vector leptoquarks. Since scalar leptoquarks are easier to detect than vector particles (figure 34), this difference will become obvious as soon as a signal within the cuts for vector particles is detected. Leptogluons however show in fact a very similar behaviour compared to vector leptoquarks and a much larger statistic would be needed to differentiate them.

- For some of the leptoquarks and for the leptogluons the decay in a neutrino is impossible while for all others the branching ratio $BR = \frac{LQ \rightarrow \nu q}{LQ \rightarrow eq}$ is in the order of one. Table 2 gives an overview of the relative probability of finding an electron or a neutrino event for a given leptoquark. So, a signal in the decay mode with an electron allows to predict the number of decays with a neutrino. As soon as statistics allows to observe these events, a separation between different leptoquark species will be feasible.

- Almost all species may be distinguish on behalf of the helicity structure of the coupling if a polarization of the electron beam and a positron beam becomes available.

- Leptogluons might be separated from leptoquarks if the jet from the decay can be identified as a gluon or a quark jet. This however will be rather uncertain on an event by event basis and is especially doubtfull in view of the fragmentation effects discussed in chapter 5.3.4.

Table 7 gives an overview of how to disentangle the various left and right handed couplings. This can be used to decide, in case of a signal at $HERA$, which of the theoretical models predicting leptoquarks (chapter 2) is more favourable. As an example, the '$SU(5)$- saver' model including the $\tilde{S}_{1/2}$ leptoquark can be distinguished from the superstring inspired $E(6)$ theory containing the S_o leptoquark with help of the different ratios of neutral to charged current events.

6.6 Uncertainties

The structure functions used for event generation have never been measured but are extrapolated from experimental data at much lower Q^2. In the region of interest, the existing parameterizations differ by about 10%. Uncertain is, in addition, the choice of

coupling	$\lambda_{L\,s_0}$	$\lambda_{R\,s_0}$	$\lambda_{R\,\tilde{s}_0}$	$\lambda_{L\,s_1}$	$\lambda_{L\,s_{1/2}}$	$\lambda_{R\,s_{1/2}}$
$\lambda_{L\,s_{1/2}}$	BR	P	P	BR	?	P
$\lambda_{R\,s_{1/2}}$	BR	e^+	e^+	BR	P	
$\lambda_{L\,\tilde{s}_{1/2}}$	BR	P	P	BR		
$\lambda_{L\,s_1}$	BR	BR	BR			
$\lambda_{R\,s_0}$	BR	?				
$\lambda_{R\,\tilde{s}_0}$	BR					

coupling	$\lambda_{L\,v_{1/2}}$	$\lambda_{R\,v_{1/2}}$	$\lambda_{L\,\tilde{v}_{1/2}}$	$\lambda_{L\,v_0}$	$\lambda_{R\,v_0}$	$\lambda_{R\,\tilde{v}_0}$	$\lambda_{L\,v_1}$
(LG)	P	P	P	P	P	P	BR
$\lambda_{L\,v_1}$	BR	BR	BR	BR	BR	BR	
$\lambda_{L\,\tilde{v}_0}$	P	e^+	P	BR	?		
$\lambda_{R\,v_0}$	P	e^+	P	BR			
$\lambda_{L\,v_0}$	BR	BR	BR				
$\lambda_{L\,\tilde{v}_{1/2}}$	?	P					
$\lambda_{R\,v_{1/2}}$	P						

Table 7: *Separation methods for scalar and vector leptoquarks and leptogluons. Entries in the two tables can be separated via angular decay distributions. 'BR' means branching ratio, 'P' means polarization, 'e$^+$' a positron beam. A '?' requires either a target with a different quark content or a neutrino experiment. For the description of the various couplings see chapter 2.6.*

the scale Q^2 used in the evaluation of the structure function. However the cross section of both background and signal depend on the uncertainties of the structure functions in the same way. Due to Poisson statistics the cancellation is not perfect but can be neglected for the evaluation of limits in comparison to the statistical errors.

The fragmentation effects for leptoquarks and leptogluons discussed in chapter 5.3.4 are not included in the event generator. Generally they will have the effect of broadening the natural width of the particle. If this exceeds the experimental mass resolution, the limits presented would be weekend correspondingly. This needs further investigations with improved event generators.

Radiative corrections, which are not included in the background simulation, are expected to increase the event rates for DIS at high y. However, the Born cross section at high y is rather low and events with initial state bremsstrahlung are effectively tagged by this analysis. Furthermore, a cut at $y = 0.95$ was applied. Nevertheless, a more detailed study is needed here.

The statistical uncertainties due to the huge photoproduction background have already been discussed earlier.

The absolute calibration of the different calorimeter stacks will not be known much better than 1– 2%. This will result in shifts in the mass distribution, which depend

on the angle of the electron and the quark jet in the detector and therefore on y. In the worst case the limits for the coupling constant of a 200 GeV leptoquark might be decreased by $\approx 30\%$. A correction of the same order would be caused by an additional, energy independent term in the energy resolution. Preliminary test beam results of the *H1* calorimeter indicate [74] that for the weighted resolution this term is below 1% and thus presumably less critical than the absolute intercalibration of stacks.

7 Conclusion

Leptoquarks are colour triplet states which couple to leptons and quarks. They are predicted as a natural connection between the quark and the lepton sector of particles by Grand Unifying Theories, Supersymmetry, Superstring inspired E(6) models, Technicolour and Compositeness scenarios. Specifically in certain Compositeness models, also the existence of colour octet states called 'leptogluons' is possible with vertices to leptons and gluons.

HERA as an electron– parton collider will be the ideal source for these possible, exotic particles. Their dominant experimental signature would be the decay into an electron or neutrino and a jet balancing each other in transverse momentum. This topology is indistinguishable from deep inelastic scattering events. Leptoquarks and leptogluons would appear as very narrow resonances in the Standard Model Bjorken x distribution at $x = M^2/s$, where M is the mass of the new particle and $\sqrt{s}$ is the center of mass energy. Therefore, neutral and charged current events constitute the most important background for leptoquarks and leptogluons. Other possible sources of background are expected due to the huge cross sections for the photoproduction of light and heavy quarks. Both processes will lead to more than 10^7 triggers per year.

Technically, an analysis of so many events is difficult especially due to the very time consuming event simulation. Therefore, a new monte carlo for the *H1* detector was developed, which is at least 300 times faster than other programs and allows to simulate 10^6 events per day on a mainframe computer. The program describes in detail the geometric acceptance, the efficiency and the resolutions of all detector components. Also non gaussian effects like passive material and cracks in the calorimeter, leakage, double hit resolutions in the tracking devices, particle decays and secondary interactions are included. Reconstruction algorithms are simulated as well in order to avoid slow pattern recognition programs. Applications for this monte carlo are seen mainly in the development of analysis strategies, for unfolding procedures and for the determination of systematic errors. Furthermore, such a fast simulation is presumably the only choice for the simulation of large background event samples. In this case, it can be used also as a first filter step before a detailed simulation of potentially 'dangerous' events is done.

For the analysis of leptoquarks and leptogluons decays into neutrinos or electrons are considered separately. Events with neutrinos are tagged by asking for a large missing transverse momentum. The mass of the leptoquarks may be reconstructed from the hadronic energy flow alone.

For neutral current signatures the decay electron has to be identified. In the mass range of interest for leptoquarks and leptogluons, purely kinematic and topological arguments, namely the requirement for an isolated particle with high transverse momentum are applied. All further cuts are based on a *constrained kinematic fit* which enforces momentum balance in the transverse plane. This fit can be performed independent of fragmentation effects and of initial state radiation. The primary result of the fit are

improved measures for the electron and the hadrons. Also the energy of an undetected photon from initial state radiation is reconstructed this way. This is used to

- separate photoproduction events from leptoquark and deep inelastic scattering events

- distinguish neutral current from charged current events by a cut in the χ^2 of the fit

- correct for initial state bremsstrahlung

- reject badly measured events by a cut in the χ^2 of the fit

- reconstruct in an optimum way the event kinematic in deep inelastic neutral current events

- reconstruct the leptoquark mass with a precision of about $\pm$ 2 GeV.

Deep inelastic scattering events can be distinguished from leptoquarks and leptogluons only on a statistical level. Beside a cut on the reconstructed mass, the Bjorken variable y is used for this separation. For all different leptoquark species, these cuts are optimized in order to achieve best exclusion limits. The good mass resolution obtained by the constrained fit improves the final efficiency by about a factor 2.

Limits for leptoquark detection have been evaluated in a model independent analysis for all possible, dimensionless, $SU(3)_c \times SU(2)_L \times U(1)_Y$ invariant leptoquark couplings. They show that up to almost the kinematic limit of 314 GeV, couplings one order of magnitude below present bounds can be explored. To give an example, couplings as small as $4 \cdot 10^{-4} \cdot \alpha_{em}$ for $M_{LQ} = 100$ GeV ($4 \cdot 10^{-3} \cdot \alpha_{em}$ for $M_{LQ} = 250$ GeV) can be excluded for scalar leptoquarks. For leptogluons, the compositeness scale can be tested between 80 TeV at low masses and 1 TeV at a mass of 300 GeV. Furthermore, a measurement of the quantum numbers of leptoquarks and leptogluons is feasible and would allow a distinction of these species. In most cases, theoretical models can thus be distinguished by measuring just the branching ratios into electrons and neutrinos.

Remaining uncertainties are due to fragmentation effects and to the absolute calibration of the calorimeters.

References

[1] P. Schleper, Proceedings of the Workshop 'Physics at HERA', DESY 1991

[2] V. D. Barger, R. J. N. Phillips, Collider Physics, Addison– Wesley, 1987

[3] Ch. Berger et. al., Z. Phys. C50 (1991) 385
S. Seidel et al., Phys. Rev. Lett. 61 (1988) 2522
K. S. Hirata et. al., Phys. Lett. B220 (1989) 308

[4] U. Amaldi, W. de Boer, H. Fürstenau, Phys. Lett. B260 (1991) 447
W. de Boer, H. Fürstenau, IEKP–KA/91–07
J. Ellis, S. Kelley, D.V. Nanopoulos, CERN–TH. 6140/91

[5] H. Murayama, T. Yanagida, Tohoku University, TU–370, 1991

[6] P.H. Frampton, B.H. Lee, Phys. Rev. Lett. 64, 619 (1990)
P.H. Frampton, T.W. Kephart, Phys. Rev. D42, (1990) 3892
P. Pal, Phys. Rev. D43, 236 (1991)

[7] J. Wess, B. Zumino, nucl. Phys. B70, (1974) 39
X. Tata, Mt. Sorak symposium lectures, UH-511-713-90

[8] J.A. Hewett, University of Wisconsin, Preprint 1991, WI 53706

[9] V. Barger, G.F. Guidice, T. Han, Phys. Rev. D40, (1989) 2987

[10] T. Kon, T. Kobayashi, Tokyo Metropolitan University,
TMUP-HEL-9107, ITP-SU-91/03

[11] M.B. Green, J.H. Schwarz, Phys. Lett. B149, (1984) 117

[12] J.A. Hewett, T.G. Rizzo, Phys. Rep. 183, (1989) 193

[13] N.D. Tracas, S.D.P. Vlassopulos, Pys. Lett. B220 (1989) 285

[14] J.F. Gunion, E. Ma, Pys. Lett. B195 (1987) 257
J.A. Grifols, S. Peris, Pys. Lett. B201 (1988) 287

[15] A. Dobado, M.J. Herrero, C. Munoz, Pys. Lett. B191 (1987) 447

[16] L. Susskind, Phys. Rev. D20 (1979) 2619
S. Weinberg, Phys. Rev. D19 (1979) 1277
S. Dimopoulos, L. Susskind, Nucl. Phys. B155 (1979) 237
E.Eichten, K. Lane, Phys Lett. B90 (1980) 125
M. Einhorn, Proceedings of: Particle and Fields, Vancouver 1991
J. Rosner, D. Soper, CERN– TH.6014/91, EFI 90-75

[17] A. Djouadi, T. Köhler, M. Spira, J. Tutas,
Z. Phys. C– Particles and fields 46,679-685 (1990)

[18] H. Harari, Scottish Summer School, St. Andrews, 1984
H. Harari, Seiberg, Phys. Lett. B98 (1981) 269
Greenberg, Sucher, Phys. Lett. B99 (1981) 339

[19] L.F. Abbott, E. Fahri, Phys. Lett. B101 (1981) 69
L.F. Abbott, E. Fahri, Nucl. Phys. B189 (1981) 547

[20] J. Wudka, Phys. Lett. B167 (1986) 337

[21] H. Fritsch, G. Mandelbaum, Phys. Lett. B102, (1981) 319

[22] U. Baur, K.H. Streng, Z. Phys. C30 (1986) 325

[23] K.H. Streng, Z. Phys. C33 (1986) 247

[24] J. Bijnens, Proceedings of the HERA Workshop, 1987

[25] H. Harari, Phys. Lett. B156 (1985) 250

[26] U. Baur, K.H. Streng, Phys. Lett. B162 (1985) 387
Y. Nir, Phys. Lett. B164 (1985) 395

[27] W. Buchmüller, R. Rückl, D. Wyler, Phys. Lett. B191 (1987) 442

[28] E. Eichten, I. Hinchliff, K. Lane, Ch. Quigg,
Rev. Mod. Phys 56 (1984) 579; revised ibid. 58 (1986) 1047

[29] W. Buchmüller, D. Wyler, Phys. Lett. B177 (1986) 377

[30] Particle Data Book, Phys. Lett. B239 (1990) 1

[31] M. A. Doncheski et. al., Phys. Rev. D40 (1989) 2301
I. I. Bigi, G. Köpp, P. M. Zerwas, Phys. Lett. B166 (1986) 238

[32] J. Blümlein, R. Rückl, Proceedings of: $'e^+e^-$ at 500 GeV',
Hamburg and Saariselkä, 1991

[33] M. Kuhlen, PhD Thesis, Hamburg, 1986

[34] B. Schrempp, F. Schrempp, Phys. Lett. B153 (1985) 275

[35] L3 Collab., B. Adeva et al., L3 Preprint #26, 1991
Opal Collab., CERN–PPE/91–61, 1991, submitted to Phys. Lett. B

[36] J.L. Hewett, T,G, Rizzo, Phys. Rev. D36 (1987) 3367

[37] M. de Montigny, L. Marleau, Phys. Rev. D40 (1989) 3616

[38] UA2 Collab., J. Alitti, CERN-PPE91-158, 1991, submitted to Phys. Lett. B

[39] J. Freeman, talk presented at the
     25th International Conference on High Energy Physics,
     Singapour, August, 1990 (not mentioned in the proceedings)

[40] M. A. Doncheski, J. L. Hewett, MAD/PH/584, September, 1990

[41] B. Schrempp, Proceedings of the Workshop, 'Physics at HERA', DESY 1991, and
     references therein

[42] Th. Köhler, Thesis RWTH Aachen (1989)
     Th. Köhler, Proceedings of the Workshop 'Physics at HERA', DESY 1991,

[43] HERA proposal report, DESY HERA 81/10, Hamburg 1981

[44] F. Schrempp, 'Contact interaction',
     Proceedings of the Workshop 'Physics at HERA', DESY 1991,

[45] G. Ingelman, LEPTO 5.2 manual, DESY
     G. Ingelman, Proceedings of the Workshop 'Physics at HERA', DESY 1991,

[46] T. Sjostrand, Proceedings of the Workshop 'Physics at HERA', DESY 1991,

[47] Letter of Intent, H1 Collaboration, DESY Internal Report, June 1985
     Technical Proposal for the H1 Detector, H1 Collaboration,
     DESY Internal Report PRC-86/02 (1986)
     Technical Progress Report, H1 Collaboration,
     DESY Internal Report PRC-87/01 (1987)

[48] R. Nisius, P. Schleper et. al., 'A Guide to H1PSI', *H1* internal note

[49] Proceedings of the Workshop 'Physics at HERA', DESY 1991,

[50] H. Albrecht, M. Erdmann, P. Schleper, 'H1PHAN, a physics analysis program for *H1*

[51] 'H1REC', H1 internal note

[52] J. Meyer et al., Guide for H1 simulation program H1SIM, H1 software note 11/89

[53] R. Brun et. al., CERN Data Handling Division, DD/EE/84-1, September 1987

[54] R.L.Ford und W.R.Ford; EGS Manual; SLAC-0210, Stanford 1978

[55] H. Fesefeld, PITHA report, 1985

[56] J. Freeman, CDF Detector Simulation, Fermilab-Conf-87/230

[57] Conclusion of the Workshop for Physics Analysis, H1 Software Note H1-05/89-112

[58] A. Fedotov, H1 Software Note H1-09/91-195

[59] R. L. Gluckstern, Nucl. Instr. Meth. 24 (1963) 381

[60] I. Skillicorn, private communication

[61] G. Grindhammer, M. Rudowicz, S. Peters,
Nucl. Instr. Meth. A290 (1990) 469
M. Rudowicz, Thesis at University of Hamburg, 1989
S. Peters, Thesis at University of Hamburg, 1989

[62] M. Rudowicz, P. Goritchev, privat communication

[63] R. Martin, privat communication

[64] J. Turnau, privat communication

[65] U. Braun, privat communication

[66] M. Nyberg, privat communication

[67] S. Levonian, privat communication

[68] A. deRoeck, privat communication

[69] H. Jung, Proceedings of the Workshop 'Physics at HERA', DESY 1991,

[70] R. Nisius, privat communication

[71] Th. Merz, Diploma Thesis, University of Hamburg, 1990

[72] Ch. Berger, Proceedings of the Workshop 'Physics at HERA', DESY 1991,

[73] P. Schleper, *H1* workshop, January 1991

[74] P. Schacht, privat communication

[75] W.Bartel et. al., JADE Collaboration, Z.Phys. C33 (1986) 23

[76] Proceedings of the study of an ep facility for Europe,
Ed. U. Amaldi, DESY 79/48 (1979) 391

[77] P. Schacht, privat communication

List of Figures

List of Tables

Danksagung

Lebenslauf

Am 28.7.1961 wurde ich als drittes von fünf Kindern der Eheleute Bernard und Elisabeth Schleper, geb. Spenthof, in Oberhausen geboren. Nach dem Besuch der Grundschule von 1967 - 1971 erlangte ich 1980 am Freiherr - vom - Stein - Gymnasium in Oberhausen - Sterkrade die allgemeine Hochschulreife. Auf ein 2 monatiges Industriepraktikum und die Bundeswehrzeit folgte im Herbst 1981 der Beginn des Studiums im Fach Physik an der RWTH Aachen. Die Diplomprüfung absolvierte ich im Frühjahr 1988. Seit dieser Zeit arbeite ich als Wissenschaftlicher Angestellter des 1. Physikalischen Institutes der RWTH Aachen. Neben Lehraufgaben habe ich in Hamburg am Deutschen Elektronensynchrotron DESY bei der Erstellung der Software für das H1 - Experiment mitgewirkt. Seit 1988 bin ich verheiratet mit Frau Diplom Physikerin Sylvia Schleper, geb. Bielefeld.